UNIVERSITY OF OKLAHOMA

GRADUATE COLLEGE

A STUDY OF LEAN PREMIXED SWIRL-STABILIZED COMBUSTION OF GASEOUS ALTERNATIVE FUELS

A Dissertation

SUBMITTED TO THE GRADUATE FACULTY

in partial fulfillment of the requirements for the

degree of

Doctor of Philosophy

By

DONALD M. WICKSALL
Norman, Oklahoma
2004

A STUDY OF LEAN PREMIXED SWIRL-STABILIZED
COMBUSTION OF GASEOUS ALTERNATIVE FUELS

A Dissertation APPROVED FOR THE
SCHOOL OF AEROSPACE AND MECHANICAL ENGINEERING

BY

_____
Dr. Ajay K. Agrawal: Committee Chair

_____
Dr. Subramanyam R. Gollahalli: Committee Member

_____
Dr. Richard G. Mallinson: Committee Member

_____
Dr. Ramkumar N. Parthasarathy: Committee Member

_____
Dr. William H. Sutton: Committee Member

ACKNOWLEGEMENTS

I would like to thank God, through whom all things are possible. I also appreciate the love, support and encouragement of my family and friends, which has made my work possible. I am especially grateful to my parents, Mike and Doris Wicksall, for their love and prayers, and for being my first teachers and instilling and nurturing the desire to learn in me.

I would also like to express my thanks to my advisor Dr Ajay Agrawal for his advice and encouragement throughout the course of my studies. I would like to acknowledge the mentorship of Dr. Robert Schefer of Sandia National Laboratories in the area of laser diagnostics. I would also like to express my thanks to the other committee members Dr. Gollahalli, Dr. Mallinson, Dr. Parthasarathy, and Dr. Sutton for their guidance and advice in this work.

TABLE OF CONTENTS

LIST OF TABLES

LIST OF FIGURES

NOMENCLATURE

Symbol	Definition
a	Constant in the pressure forcing function (RUN-1DL)
$\left.A/F\right)_{Actual}$	Air to fuel ratio of the actual mixture
$\left.A/F\right)_{Stoic.}$	Air to fuel ratio of a stoichiometric mixture
c	Speed of sound
C1	First coefficient to calculate the stoichiometric air to fuel ratio
C2	Second coefficient to calculate the stoichiometric air to fuel ratio
C_p	Mixture specific heat
D1	First coefficient used in the adiabatic flame temperature curve fit
D2	Second coefficient used in the adiabatic flame temperature curve fit
D_H	Hydraulic diameter
D_{SW}	Diameter of the swirler
Da	Damkohler number
‹E›	Bias error in the PIV measurement
f	Frequency of oscillation
F(ω)	Fourier transform of a function in angular frequency
f(t)	Original function upon which Fourier transform operates
G	Normalized velocity (u/x) (RUN-1DL)
h_i	Enthalpy of the ith species (RUN-1DL)
$\hat{i}$	Horizontal unit vector
$\hat{j}$	Vertical unit vector
j	Square root of negative 1

k	Wave number
$\hat{k}$	Out of plane unit vector
Ka	Karlovitz number
Ked	Kinetic energy dissipation rate
Ked_{2D}	2-D kinetic energy dissipation rate
l	Length of the oscillating column
L	Convective-accumulative operator used in the governing equations for RUN-1DL computer model
L	Length and width of the interrogation region
N	Number of particle pairs in the interrogation region
N	Total number of samples used in the calculation of a discrete Fourier transform
P'(t)	Pressure forcing function (RUN-1DL)
Q	Volumetric flow rate
r	Density of the reactants
r_0	Outer radius of an annulus
Ri	Inner radius of an annulus
Re	Reynolds number
Ri	Auto-correlation coefficient at the ith point
S	Swirl Number of an axial swirler
S_e	Source term for conservation of energy equation (RUN1-DL)
S_m	Source term for conservation of momentum equation (RUN1-DL)
S_v	Source term for conservations of mass equation (RUN-1DL)
t	Time

T	Temperature (RUN-1DL)
Tad	Calculated equilibrium adiabatic flame temperature
TKE	Turbulent kinetic energy
u	Velocity component parallel to the stagnation plane (RUN-1DL)
u	Horizontal velocity component
u_0	Horizontal velocity component at the center of the interrogation region
U_{RMS}	Horizontal root mean squared velocity component
$\vec{V}$	Velocity vector
v	Flow velocity perpendicular to the stagnation plane (RUN-1DL)
v	Vertical velocity component
v_0	Vertical velocity at the point of interest
V_0	Velocity at the center of the interrogation region
v_0	Vertical velocity component at the center of the interrogation region
v_{0avg}	Average vertical velocity at the point of interest
V_i	Diffusion velocity of the ith species (RUN-1DL)
v_i	Vertical velocity i steps away from the point of interest
v_{iavg}	Average vertical velocity i steps away form the point of interest
V_{RMS}	Vertical root mean squared velocity component
w	Out of plane velocity component
W	Thickness of the PIV laser sheet
X	Mole fraction of fuel additive in the fuel
x	Coordinate direction parallel to the stagnation plane (RUN1-DL)
x	Horizontal coordinate direction

y	Coordinate direction perpendicular to the stagnation plane (RUN-1DL)
y	Vertical coordinate direction
Y_i	Mass fraction of the ith species (RUN-1DL)
Z	Out of plane coordinate direction
ΔP	Pressure drop across the laminar flow element
Δt	Time between laser pulses
Δt	Sampling interval in Fourier analysis
ΔX	Distance between adjacent velocity vectors
Φ	Equivalence ratio of a fuel and air mixture
ε	Normal strain rate, or volumetric dilatation rate
ϕ	Generic quantity acted on by the L operator (RUN-1DL)
λ	Mixture thermal conductivity (RUN-1DL)
μ	Dynamic viscosity
ν	Kinematic viscosity
ρ	Density of the air in the laminar flow element
ρ_∞	Density of the ambient air (RUN-1DL)
σ_E	Random error associated with PIV measurement
ω	Angular frequency of signal in a Fourier transform
ω	Vorticity vector
ω_{AFR}	Uncertainty in the air to fuel ratio
ω_i	Mass production rate of the ith species (RUN-1DL)
ω_{Tad}	Uncertainty in the adiabatic flame temperature

ω_v	Uncertainty in the velocity
ω_{XH2}	Uncertainty in the mole fraction of H_2 in the fuel
ω_z	Z-component of the vorticity vector
ω_Φ	Uncertainty in the equivalence ratio
ω_ω	Uncertainty in the vorticity
∇	Gradient operator

ABSTRACT

The effects of utilizing gaseous fuels with different compositions was studied for a lean premixed swirl stabilized burner typical of those used in land-based gas turbine engines. The experiments were performed at atmospheric temperature and pressure in a quartz glass combustor. The fuels utilized were binary mixtures containing either methane or propane as the primary component and hydrogen, oxygen, nitrogen or carbon dioxide as the secondary component. The combinations chosen represent constituents of various gaseous alternative fuels. In particular, focus was placed on hydrogen enriched hydrocarbon fuels proposed as a cross-over strategy to the hydrogen energy infrastructure. The operating parameters included fuel composition, total reactant flow rate, and the calculated adiabatic flame temperature. Global flame characteristics such as emissions of oxides of nitrogen (NOx) and carbon monoxide (CO), flame extinction, and combustion noise were studied. The internal characteristics of flames were also studied, including the velocity field and related flow properties, as well as the structures of the reaction zones.

The burner was constructed of 1.5" (3.8 cm) schedule 40 steel pipe. Fuel injectors were placed 40 cm upstream of the burner to ensure that the fuel and air were fully premixed prior to combustion. The fuel air mixture entered the combustion chamber in the annulus around a centerbody which contained 6 swirl vanes to impart an out of plane motion to the flow. The flow expanded into the combustion chamber which had an 8.1 cm inside diameter, and was exhausted into the ambient at the end of the combustion chamber. Pollutant emissions were

measured using an electro-chemical gas analyzer and water-cooled stainless steel and expansion-cooled quartz probes. Flame extinction was studied by visual observation of the flame. Combustion related noise was recorded using a condenser microphone and digitized by a high speed data acquisition card. Frequency and power spectra were obtained from the sound data by Fourier transform. The flow field was measured using particle image velocimetry (PIV), which provides velocity data in a planar area. Velocity data were analyzed to provide flow properties of interest including vorticity, normal strain, RMS velocity, turbulent kinetic energy, kinetic energy dissipation rate, and integral length scale. The flame structure was observed by planar laser induced fluorescence of the hydroxyl (OH) radical. The OH radical is produced in the reaction zone of the flame and was utilized as a marker of the location and intensity of these zones. Simultaneous measurements of the velocity field and the OH radical concentration were obtained to study the interaction of the flame and the flow field. One dimensional flame calculations were performed using the RUN1-DL code to understand the effects of strain rate on flames burning fuels of different compositions.

Pollutant measurements indicate that NOx forms closer to the inlet in hydrogen enriched flames, but the exit level is similar to that of a methane flame at the same adiabatic flame temperature. The CO levels are significantly reduced in the hydrogen enriched flames due to enhanced burn-off and a higher hydrogen to carbon ratio. For all the fuels tested single digit emissions of NOx and CO were attainable near the lean limit before the flame became unstable. The

extinction limit was shown to depend on the fuel composition, with hydrogen offering a significant reduction in the lean limit. PIV measurements showed that the velocity field was altered by the addition of hydrogen such that the inlet jet of reactants shifted toward the downstream direction. The instantaneous velocity fields had many small scale vortical structures in them which were not present in the time-averaged fields, indicating the importance of temporally resolved data for experimental and modeling purposes. Measurements of the OH radical indicated that the flame structure changed with the addition of hydrogen to the hydrocarbon fuel, producing shorter and more intense flames able to sustain combustion in the corner recirculation zone. Simultaneous velocity-OH measurements showed that the combustion was frequently occurring on the outer edge of vortical structures where the combination of mixing of reactants with products and reduced velocity was able to help stabilize the combustion. The hydrogen enriched flame seems less dependent on the flow field than the methane flame. This statement is supported by the fact that it is a more stable flame, and that it is able to withstand significantly more strain before extinction as calculated by the 1-D simulation. Combustion noise measurements showed two primary modes at 450 and 600 Hz.

CHAPTER 1: INTRODUCTION

1.1 Background

Advanced gas turbine engines utilize lean premixed (LPM) combustion to reduce pollutant emissions. Although LPM systems reduce thermal formation of oxides of nitrogen (NOx) by lowering the peak flame temperature, they are prone to combustion instabilities, flashback, autoignition, and extinction. Most current LPM combustion systems utilize natural gas (NG), primarily containing methane (CH_4), because it has been studied extensively and its properties are well known. However, the availability of alternative gaseous fuels such as gasified coal or biomaterial, chemical and refinery wastes, fuel cell off-gasses, etc. is driving the need for fuel-flexible gas turbine systems. Richards et al. (2001) state that the cost-effective utilization of alternative fuels with a wide range of heating values is a current priority.

Understanding the role of hydrogen (H_2) on LPM combustion is important for utilization of these fuels because many alternative fuels contain significant quantities of H_2. For example, low and medium heating-value fuels containing H_2 are often produced as by-products in Coal-Gasification Combined Cycle installations. These product gases could provide a significant source of cost-effective fuels for power generating gas turbines. Currently, these fuels are typically used in gas turbines with conventional diffusion flame burners (Maden, 1998) resulting in poor emissions performance, although new approaches have been considered (Hasegawa et al., 2000, 2001; Adouane et al., 2003). A second need is related to the recognition that ultra-lean premixed combustion is effective

in reducing the NOx emissions. Hydrogen blended with traditional hydrocarbon fuels could improve flame stability and allow stable lean combustion at the lower temperatures needed to minimize the NOx production (Ren et al., H_2 2001). Anderson (1975) studied the addition of H_2 to propane (C_3H_8) in a tube burner. The results showed that H_2 extended the lean blow out limit for both a H_2 pilot torch, and when the H_2 was premixed with C_3H_8. The NOx emissions showed improvement when the H_2 was premixed, but not when it was burnt in a non-premixed mode, indicating the need for fuel-air premixing. Philips and Roby (1999) examined the annualized costs of operating a gas turbine engine using a fuel mixture of H_2 and NG. Their calculations indicated that a system utilizing a NG/H_2 blended fuel could be significantly less expensive than other low emissions concepts, such as selective catalytic reduction (scrubbing) of the exhaust. A longer-term need is the desire to minimize and, eventually, eliminate unburned hydrocarbons (UHC) and carbon dioxide (CO_2) emissions. The use of H_2-blended fuels provides both a solution to the immediate need for NOx reduction, and a transition strategy to a carbon free energy system in the future. A review of literature on the subject of alternative fuels follows.

1.2 Literature review

The literature review will be divided into sections giving examples of past work in the field of alternative fuel utilization in LPM systems, and will explain how the present work has differed from the past studies and added to the knowledge base. The review will progress from work on simplified or idealized flame geometries to practical configurations. Optical diagnostics techniques

including particle image velocimetry (PIV), and planar laser induced fluorescence (PLIF) measurements used to obtain flow field and flame structure information will be discussed. The simultaneous application of these optical techniques for combustion studies will also be examined. Lastly, findings on the effect of fuel composition on thermo-acoustic instabilities will be presented.

1.2.1 Idealized flame configurations

Numerical and experimental studies have been conducted to study the effects of fuel composition on lean premixed combustion in opposed flow flames. This idealized configuration consists of two co-axial jets forming a stagnation plane, or a single jet impinging on a heated wall. This configuration has been utilized extensively because the flow field is 1-D along the centerline, and hence, simplified analytical solutions can be obtained without much computational effort. Gauducheau et al. (1998) performed a numerical study of stretched lean premixed H_2 enriched CH_4 flames at high pressures to study their use in spark ignition engines. Specifically, they were interested in high compression ratio supercharged engines (30 Atm and over 700K) that would use NG's high octane number (130) to achieve improved efficiency. It was determined that flame stretch (or strain) due to the turbulent nature of combustion in the chamber could lead to local extinction, reducing combustion efficiency and increasing pollutants. Therefore, extinction by strain is important, and it must be understood to achieve optimal combustion performance. Their results showed that H_2 increased the flame's resistance to strain, which would allow combustion at a lower equivalence ratio, producing lower emissions. Furthermore, they found that in the case of a

stretched H_2-enriched flame the calculated radical pool concentrations were significantly enhanced, which would improve the flame stability. Cong and Jackson (1999) studied strained H_2-enriched CH_4 flames using a 1-D model. They also observed improved flame stability under stretched conditions with the addition of H_2.

Ren et al. (Reforming, 2001) performed both experimental and numerical investigations of the effects of burning $CH_4/H_2/CO/CO_2$ mixtures. They studied the fundamental flame configuration of a single jet of premixed reactants impinging on a heated wall. The fuel compositions were chosen to emulate a fuel stream containing a mixture of NG and reformate gas from either a steam or a dry reformer. The motivation for their work was to utilize the waste heat from a gas turbine engine to provide energy for the endothermic CH_4 reforming process. Chemically recuperating the heat energy in the exhaust in this manner raises the engine's efficiency. The addition of H_2, and to a lesser degree CO, to the fuel was found to increase the flame stability by increasing flame speed and resistance to extinction by strain. They also found that the majority of the NOx was produced downstream of the flame in the hot post combustion zone. Similar results were obtained by Jackson et al. (2003) in the opposed-jet flow configuration, who found early H_2 breakdown increased radical production near the base of the flame and thereby, increased the burning rates. Their study also showed that enriching CH_4 with H_2 increased the maximum allowable strain rate before extinction temperatures were reached, for the above reasons.

Wu et. al. (1999) conducted numerical and experimental studies of the effect of O_2 enrichment on lean CH_4/air flames. The experimental apparatus and computer model consisted of a single premixed jet impinging on a temperature-controlled wall. Oxygen enrichment was found to extend the lean flammability limit to lower flame temperatures resulting in lower NOx production, similar to the effect of H_2 enrichment. While this study characterizes the behavior for a fundamental flame configuration, limited conclusions about the effect of O_2 enrichment on a practical combustor could be drawn.

Qin et. al. (2001) examined the use of landfill gas (LFG) in a lean premixed combustion system to generate power. A single premixed jet impinging on a heated wall was studied experimentally and numerically. Landfill gas is composed of CH_4 and CO_2 together with other trace species. The results of this fundamental flame analysis indicate that CO_2 does not significantly change the extinction flame temperature, as it is an inert species. The CO_2 acts as a diluent, thus more CH_4 must be burnt to maintain the same flame temperature. Carbon dioxide does affect the chemical kinetics in third body reactions, since it has a significantly higher third body efficiency than other prevalent species. CO_2 also increases the radiative heat loss of the flame.

These 1-D studies provide insight into how fuel composition affects the flame, but are limited in practical application by their simple nature. They show that the strain rate characteristics of a fuel mixture are important parameters to understanding the behavior of these fuels. The studies however do not provide insight into the combustion of these fuels in practical devices such as

reciprocating, or gas turbine engines which have turbulent 3-D flow fields not captured by these simple models. Understanding of the 3-D flow field is important because issues such as curvature, local stretch, and transient affects on flame structure must be taken into account. While average strain rates in flames are on the order of those predicted by 1-D models, the instantaneous strain rates can be an order of magnitude greater. For these reasons, the present work was conducted in a swirl-stabilized burner to determine the effects of fuel composition under more realistic flow conditions. Opposed flow modeling will however be used to show the effects of H_2 addition on the average extinction strain rate.

1.2.2 Effects of fuel composition on practical flames

Fuels containing H_2 have been used for some time in conventional non-premixed combustion systems (Meier et al., 1986). The effects of fuel composition on premixed 3-D flames have been studied in a limited manner for both reciprocating and gas turbine engines. Meyers and Kubesh (1997) studied a rich burn/lean burn reciprocating engine concept, in which some of the cylinders operated at fuel rich conditions, and then their exhaust was passed through the remaining cylinders, which burnt in a fuel lean mode. The exhaust gases circulating through the lean cylinders contained significant quantities of H_2 and CO that were formed during the incomplete combustion in the fuel rich cylinders. The H_2 present in the reburnt exhaust allowed combustion at leaner equivalence ratios, and produced lower NOx emissions from the engine. Bell and Gupta (1997) studied a spark ignition engine utilizing H_2-enriched CH_4 as fuel. Their results indicated that the engine was able to operate leaner due to the addition of

H_2. Larsen and Wallace (1997) performed experiments on a spark ignition engine that showed reduced NOx emissions when burning a mixture of H_2 and NG.

Relatively few studies have been conducted to investigate the effects of fuel composition on LPM combustion systems for gas turbine engines. The capability of commercial gas turbine engines to operate on multi-component gaseous fuels in LPM combustion mode was demonstrated by Morris et al. (1998) who utilized fuels containing up to 10% H_2 by volume. Their results showed that the addition of H_2 to NG reduced CO and NOx emissions under fuel lean conditions. Alavandi and Agrawal (2004) studied the effect of H_2 addition to CH_4 flames stabilized over a porous inert media. Their results show a reduction in CO at a given flame temperature with the addition of H_2, but not in NOx. The NOx benefits are observed because the H_2-enrichment lowers the flame temperature at LBO by about 150^0C. Schefer et al. (NASA, 2002) utilized H_2 and H_2/CH_4 fuels in a tube burner. They found that the H_2 flames burnt leaner than those containing CH_4. Flores et al. (2001) used NG blends reflecting variations in composition across the U.S. and found that both fuel chemistry and fuel-air mixing affected the combustion performance. Bhargava et al. (2000) investigated humid air premixed flames and found a reduction in NOx emissions with increasing moisture content for a fixed adiabatic flame temperature. The NOx reduction was attributed to the decrease in O-atom concentration with moisture addition. Nguyen and Samuelson (1999) studied the effect of injecting a non-premixed H_2 pilot flame into a premixed model gas turbine combustor. Their results showed that the injection of H_2 did improve lean stability characteristics, but the choice of

injection strategy limited the reductions in NOx emissions because the H_2 was not premixed. Choudhuri and Gollahalli (2003) found that the addition of H_2 to NG significantly increased the velocity that a lifted non-premixed flame could withstand before extinction. The H_2 in the fuel was found to "dominate the stability behavior", indicating the importance of studying mixed fuels in 3-D systems.

Although these past studies have begun the exploration on the use of alternative fuels in LPM systems, they have not provided sufficient information to enable the utilization of alternative fuels in engines. The present study will examine the effects of fuel composition using binary mixtures containing one fuel which is understood and one whose effect is uncertain. This systematic approach was chosen for controlled experiments because changes in fuel composition alter the flame stability and structure. Detailed measurements of flame and flow structure are needed to understand the effect of adding a certain species on the combustion performance of a fuel.

1.2.3 Measurements using optical techniques

In recent years, greater insight into the reacting flow field has been gained by utilizing PIV. Swirling flow field have been studied in particular for their application to gas turbine engines. In gas turbine engines a swirling flow is created to stabilize the flame. Ji and Gore (2002) measured the flow field in a swirl-stabilized, unconfined burner and found significant differences between mean and instantaneous flow structures. Many smaller scale vortices were observed in the instantaneous flow fields, in contrast to the averaged field with a

single large vortex. The vorticity magnitude in the flame was several times higher than that in the non-reacting flow. Based on the differences in the mean and instantaneous flow structures, they proposed that the latter should be used to evaluate transient LPM combustion phenomena. Another result was that heat release in the flame was found to affect mean and instantaneous flow structures, indicating strong coupling between fluid flow and chemical reactions.

Archer and Gupta (2004) investigated the effects of combustion and confinement in swirling flames using a stereoscopic PIV system to obtain 3-D flow-field data. They reported that combustion affected the size and extent of the recirculation zone as well as flow and vorticity fields. The confinement produced a shorter and thicker recirculation zone, although these observations were limited to the non-reacting flow. Gupta et al. (2004) developed a new method which allowed them to utilize PIV in highly luminous flames. It was found that by adding narrow band pass filters and mechanical shutters, the problem of over-exposure could be dealt with. They also claim that this technique can yield improvements in less luminous flames as well. Griebel et al. (2003) used PIV to measure the non-reacting flow field in a high-pressure combustor and obtained turbulence intensities and integral length scales. They found that the combustor can be divided into separate regions; the near region is dominated by turbulence from a grid placed upstream in their setup, and the far-field is dominated by turbulence produced in the shear layer. The integral length scale was found to vary from 2 mm near the inlet to 12 mm farther downstream. The OH PLIF measurements showed that increasing the pressure or reactant flow rate causes the

flame to become more corrugated, but does not affect the flame front position. Choudhuri and Gollahalli (2000) used LIF to measure the OH, CH, and CN radicals in a H_2-enriched NG non-premixed flame. The Peak OH concentrations were shown to correspond well with the stoichiometric contour, whereas the CH peak occurred on the fuel rich side of the stoichiometric contour.

Several research groups have obtained simultaneous measurements of the velocity and scalar fields using PIV and PLIF imaging of OH or methyl (CH) radicals in flames. Kalt et al. (1998) used PIV and OH PLIF to study premixed C_3H_8 flames. They found that as the ratio of RMS to average velocity increased, the flame propagated differently. Rehm and Clemens (1998) found that thin OH zones are associated with regions of high compressive strain in non-premixed H_2 jet flames. Rehm and Clemens (1999) also showed that the reaction zones contained high vorticity levels, in addition to the high principle compressive strain. They also found that the minimum principle strain was compressive over 80% of the time, which they attributed to a "sheet-like topography for both the OH and nonreacting scalar dissipation layers". Donbar et al. (1998) performed simultaneous CH PLIF and PIV measurements. They found highly-wrinkled but rarely-broken thin CH layers in turbulent non-premixed flames, indicating that these flames do not need to be modeled with distributed reaction zones. Data revealed instantaneous strain rates of up to 20,000 s^{-1} at the tip of the flame, though average values were lower. It was also found that the strain rates measured on the instantaneous contours of the flame were significantly different from those on the average contours. Donbar et al. (2001) used simultaneous CH

PLIF and PIV measurements to study non-premixed turbulent jet flames, in particular those with high Reynolds Numbers. Their PIV data had enough resolution to capture the Taylor scale, but not the smaller scales. They also observed that the CH layer was not affected by the high instantaneous strain levels because the structures were only briefly in contact with the flame in comparison to the chemical time scales.

Kothnur et al. (2002) obtained simultaneous measurements of OH and CH, and simultaneous CH and velocity measurements in turbulent non-premixed jet flames. Their results showed that CH structures exhibit a stronger correlation with changes in the flow field resulting from heat release, such as dilatation, than OH structures. They also found that the 2-D principle compressive strain tends to align with a 45^0 orientation to the flow in the lower part of the flame, indicating interaction between heat release and the flow field. They found that the CH structures were more likely to align orthogonal to the principle compressive strain in the lower flame. Kalt et al. (2002) used Raman-Rayleigh scattering and laser induced fluorescence to study non-premixed, unconfined swirl stabilized flames. They observed a second recirculation zone downstream of the first on the centerline. They also found a "highly rotating collar-like flow" between these recirculations region, where local flame extinctions occurred. Watson et al. (2002) used simultaneous PIV and two shot CH PLIF to study lifted CH_4/air flames. The two shot PLIF method was employed because the flame dynamics could be studied by varying the time between the images. Results indicated that regardless of the velocity of the jet, the flame stabilized at a location where the

velocity was the same for all the cases tested. Han and Mungal (2003) performed simultaneous measurements of CH and velocity in jet flames in cross flow. They found that intense combustion as denoted by the CH layers occurred in regions of high compressive strain. The mean compressive principal strain was observed to decrease along the length of the flame also. The 2-D expansion was observed to be poorly correlated with the flame position, unlike in premixed flames.

The above review indicates that instantaneous PIV measurements in swirling flows have only been obtained for (a) unconfined flows without/with LPM combustion, (Ji and Gore, 2002) and (Archer and Gupta, 2004) and (b) confined flows without combustion (Archer and Gupta, 2004) and (Griebel et al., 2003). Furthermore, none of the past studies have considered effects of fuel composition on instantaneous flow field in LPM swirling combustion. Thus, the present research will investigate how the instantaneous and time-averaged flow field of a flame is affected by the fuel composition. Experiments involve an enclosed swirl-stabilized burner operated on CH_4 and H_2-enriched CH_4. Several flow properties derived from PIV measurements such as average and RMS velocities, 2-D vorticity and normal strain, turbulent kinetic energy, and kinetic energy dissipation rate will be presented to reveal the changes in the flow field when CH_4 is enriched with H_2. Flow properties in reacting flows will be compared with those in a non-reacting flow. In addition, simultaneous measurements of the velocity field and OH field will provide information on the interaction of the flame and flow field in an enclosed burner with and without H_2 enrichment of CH_4.

1.2.4 Fuel composition effects on combustion noise

Because of the strong coupling between the flame structure and flow field, one would expect fuel composition to affect the combustor dynamics. Thus, transient flow structures affecting phenomena such as combustion stability and flame blow off and thermo-acoustic instabilities depend on the fuel composition.

The effect of fuel composition on combustion dynamics was investigated by Janus et al. (1997). They found a shift in the stability region as the fuel composition, humidity, or inlet air temperature was altered. These authors proposed that changes in the reaction rates are the primary cause of the shift in the instability regions. Nord and Andersen (2003) obtained emissions and noise data from a heavy-duty gas turbine operated on NG with composition variations. They found that the day-to-day variations in NG properties did not have a significant effect on the emissions and combustion instabilities. However, large, sudden composition changes could considerably alter the combustor's behavior. Jones and Leng (1994) studied non-premixed pulsed combustion in a commercially available NG room heater. They observed that increasing the flow rate of CH_4 increased the pressure oscillation amplitude. The addition of H_2 caused the amplitude to decrease and the heat release and pressure to become out of phase, so that the Rayleigh criteria for thermo-acoustic instabilities was not met. This effect was attributed to the higher burning velocity of H_2-enriched CH_4. The addition of C_3H_8 to the fuel caused the pressure and heat release to move slightly out of phase, and affected the oscillation frequency. Again, this was attributed to the difference in burning velocities of the fuel mixtures. Kushari et al. (1996)

studied pulse combustion and showed that changes in the fuel composition, which affect the reaction rate, play a role on affecting the pressure oscillations in the chamber. Lieuwen et al. (1998) studied combustor inlet variations of flow rate, temperature, and equivalence ratio as causes for combustion instabilities in LPM gas turbine combustors using an unsteady well stirred reactor model. Perturbations of the over all flow rate did not affect the reaction rate as the equivalence ratio was varied. Oscillations in the inlet temperature caused fluctuations at higher equivalence ratios because of the temperature dependence of the Arrhenius reaction rate model. Equivalence ratio fluctuations produced significant reaction rate oscillations at low equivalence ratios. Equivalence ratio perturbations appear to be the involved in the increase in combustion instability frequently observed near lean blow out. The present work will investigate the noise for different fuel compositions including those with H_2 in a swirl stabilized burner. This is of interest because H_2-addition changes the reaction rate and flame structure, and therefore would affect the combustion noise characteristics as well.

1.3 Objectives

The objectives of this research are to study the effects of fuel composition on a LPM swirl stabilized burner using several techniques. These experiments will provide trends that can be used for high pressure and inlet temperature applications, such as gas turbine engines, although a direct scaling of quantities is not possible. Specifically,

- First, the effects of fuel composition in a LPM combustor representative of advanced gas turbines will be obtained. The emissions of NOx and CO will be measured at several axial planes. The lean blowout limit will be measured to determine changes in operability with different fuels. The flame structure will be characterized using direct luminosity photographs and OH PLIF images. In particular, the flame behavior will be characterized under fuel lean conditions near blowout using measurements of instantaneous and time-averaged OH concentrations. Strained premixed flame analysis in an opposed flow configuration will be used to explain the observed trends.
- Second, this research will investigate how the instantaneous and time-averaged flow field of a flame is affected by fuel composition. Several flow properties derived from PIV measurements such as average and RMS velocities, 2-D vorticity and normal strain, turbulent kinetic energy, and kinetic energy dissipation rate will be presented to reveal the changes in the flow field when CH_4 is enriched with H_2. Flow properties in reacting flows will be compared with those in a non-reacting flow.
- Third, insight into the interaction between reaction zone and turbulent flow field will be obtained. Unlike past studies of non-premixed flames, we will consider LPM combustion typically employed in gas turbine engines. The operating variable is the fuel composition, i.e., pure CH_4 or H_2-enriched CH_4, to emphasize the role of the chemistry. Measurements

of the flow field and OH radical will be obtained for CH_4 and H_2-enriched CH_4 flames, using simultaneous PIV and OH-PLIF imaging.

- Fourth, the effects of fuel composition on combustion performance will be investigated. Fuels utilized will consist of H_2-enriched CH_4, and H_2-enriched C3H8. Measurements of NOx and CO emissions, flame length, and combustion noise will be obtained at different equivalence ratios representing a range of operating temperatures.

CHAPTER 2: EXPERIMENTAL APPARATUS

Explanation of the experimental apparatus will be divided into three main sections. The first section will discuss the initial setup of the burner and measurement systems used. The initial burner was a proof of concept, made out of steel pipes and fittings. The swirler was hand-made with inconsistencies from vane to vane. The second section will discuss the modified burner and setup that was developed after the successful trial period. The modified swirler was precisely machined by computer numerical control (CNC) machining, and the apparatus was made out of 304 stainless steel. In order to obtain new and more reliable data, the measuring system was also improved. In addition to the probe measurements made at the University of Oklahoma, optical measurements of the flame and flow field were performed at Sandia National Laboratories (SNL). The optical setups available at SNL made taking the measurements a turnkey operation, and avoided purchasing very expensive equipment. The last section will discuss the optical diagnostics systems utilized at SNL.

2.1 Initial burner and measurement setup

The initial experimental apparatus will be discussed in several subsystems for ease of understanding. This prototype design was used to make extinction, emissions and OH PLIF measurements. The experimental setup consists of (a) the combustion chamber and premixer, (b) air and fuel supply systems, (c) the gas sampling and analysis equipment and, (d) data acquisition and computer control system.

2.1.1 Combustion chamber and premixer

The combustor is designed to emulate swirl-stabilized lean premixed combustion systems, typical of advanced land-based gas turbine engines. The combustor was supplied with air at atmospheric pressure and temperature, and it produced 15-20 kW of heat. Figure 2.1 shows a schematic of the combustor and premixer sections of the apparatus. The fuel mixture was radially injected outward from a centerbody to mix with the air flowing through the annulus. Swirl vanes located upstream and downstream of the injector centerbody enhanced the mixing of the fuel and air. These swirl vanes were created by cutting a disk nearly to its center several times and twisting the pie shaped pieces. These swirl vanes enhanced the mixing by creating bulk fluid disturbances. The premixing chamber was 40 cm long and was made of 3.8 cm (1.5" nominal) schedule 40 steel pipe.

The mixture of fuel and air entered the combustor through a 45^{o} swirl vane in the annulus around the centerbody. The inlet swirl vane was created by tack welding strips of metal onto a piece of rod stock which became the center body. Due to the extreme heat generated during the process, some warping and nonuniformity were inevitable. The swirler was then turned on a lathe to be a snug fit inside the pipe, and finally, was tack welded into place. The inside and outside diameter (ID) and (OD) of the annulus was 3.8 cm, and 2.1 cm, respectively. The combustion chamber was a 30 cm long air-cooled quartz glass tube with 8.3 cm ID and 9.1 cm OD. The air cooling of the combustion chamber was via natural convection.

2.1.2 Air and fuel systems

The combustion air was supplied by a compressor and throttled by a regulator to about 350 KPa. A 1.9 cm gate valve was used to control the airflow. The airflow rate was measured using an ASME standard orifice meter with pressure taps located one diameter upstream and one-half diameter downstream of the orifice plate. The pressure was measured using a pressure transducer (Ashcroft Model RXLdp). The pressure drop across the flow meter was correlated with the flow rate using the Stolz Equation for a standard orifice meter.

The NG and fuel additives were supplied from compressed gas containers, each with a pressure regulator and needle valve to control the flow. The first pressure regulator for the NG was an automotive regulator (HPR-3600) and required heated water to be circulated through it to counteract the refrigerating effect of throttling high pressure NG. A second low pressure regulator in the NG system was added in series with the high pressure regulator to eliminate oscillations in the fuel flow. Figure 2.2 shows a photograph of the NG pressure regulators used. The flow rates of the NG and the additive fuel were measured using calibrated mass flow meters (Fathom Model GR-112-1-A-PV). The fuels were mixed in a tee and then homogenized by flowing through a 3 m long flexible hose upstream of the premixer.

2.1.3 Gas sampling and analysis

Gas samples from the combustor were obtained using a quartz glass probe. The probe quenched the gas sample by increasing the volume of the flow through an expansion. The ID at the tip of the probe was 1.3 mm, and it expanded to 3.8

mm. Thus, the flow area increased 9 times across the probe tip. The main body of the probe was 30cm long, with an OD of 0.635 cm. The probe was oriented parallel to the direction of flow to minimize probe interference at the measurement plane.

The pollutant concentrations were measured by gas analyzers utilizing electrochemical cells to measure each species (Nova Model 362 WP). A photograph of the gas analyzer used is shown in Figure 2.3. The gas sample was dried by passing it through water traps to prevent condensation on the sensing elements. The gas analyzer measured NOx and CO each in the range of 0-200 parts per million (PPM), and percent O_2 in the range of 0 to 25%. The NOx and CO sensors were spanned using 198 and 200 ppm calibration gasses, respectively. The O_2 sensor was spanned using air and zeroed during the calibration of the other analyzers since the calibration gases contained no O_2. All pollutant emissions data are reported on a dry uncorrected basis.

2.1.4 Data acquisition and computer control

The experiment was monitored and partially controlled using the Strawberry Tree Workbench for Windows (ver. 3.00.15 1996) data acquisition software. Figure 2.4 shows the program used to monitor and control the experiments. The program accepted analog electrical inputs and digitized and recorded these signals. The signals were acquired using a data acquisition board (Strawberry Tree Terminal Panel T71). The acquisition rate was 40 Hz, and the recorded data were a running average over 5 seconds. The measured values were used to calculate equivalence ratio, adiabatic flame temperature and flow rates of

fuel and air which were displayed on the screen. Figure 2.5 shows the displays utilized in the operation of this experiment. The program also generated digital signals to control a stepper motor and servo system to automatically advance the gas-sampling probe. Once activated, the program would move the probe to the correct position, wait for a preset amount of time (90 s) to allow the system to reach steady state, record the data, and repeat the sequence as needed.

2.2 Modified experimental setup

The initial setup was modified to improve repeatability and operability of the system, as well as to add new features. The burner and premixer sections were redesigned, the air flow system was modified to utilize a laminar flow element to improve the accuracy, a water cooled probe was designed to enhance the quenching of the sample gasses, and the equipment to measure the combustion noise was added.

2.2.1 Burner and premixer

The burner and premixer sections of the combustor were modified for some of the results presented herein. A schematic of the modified premixer and combustor is shown in Figure 2.6. Figure 2.7 shows a photograph of the modified experimental setup and its enclosure. The burner still replicated important geometric features of land-based gas turbine combustion systems, for example, premixed swirling flow expanding into an enclosure. The fuel was injected from a spoke located downstream of an air swirler to enhance mixing. This swirler was again created by bending a disk of metal. The premixer was a 40.1 cm long 304-stainless steel tube with an ID of 4.1 cm. The apparatus was made of stainless

steel to allow operation with heated air in the future. A hand held C_3H_8 torch was used to ignite the reactants at the combustor exit.

The fuel/air mixture issued into the combustion chamber through a set of six axial swirl vanes located in the annulus between the centerbody and the wall of the premixer section. The centerbody and swirler vanes were CNC machined out of a solid piece. This process created a symmetrical precisely machined swirler, which enhanced the repeatability of the experiment. Figure 2.6 also shows a detailed drawing of the inlet swirler. The vanes were angled at 28^o from the horizontal and the annulus had an ID of 2.0 cm and an OD of 4.1 cm. Figure 2.8 shows a photograph of the swirler looking down along the axis of the combustor. A typical bulk vertical velocity through the inlet annulus of 10 m/s resulted in an inlet Reynolds Number of approximately 10,000. Vertical velocities ranged from 8.5 to 22 m/s for various experiments. Equation 2.1 was used to calculate the swirl number as defined in Gupta et al. (1984)

$$S = \frac{2}{D_{sw}} \cdot \frac{G_{Tangential}}{G_{Axial}} \qquad \text{Eqn. 2.1}$$

where D_{sw} is the diameter of the swirler and $G_{Tangential}$ and G_{Axial} are the momentum fluxes in the tangential and axial directions, respectively. The swirl number is 2.3, assuming the flow exiting the swirler is parallel to the vanes. The swirl number for the initial burner setup was estimated to be 0.75.

A 30.6-cm long quartz glass tube with an 8.1 cm ID and a 9.1 cm OD was used as the combustion chamber. Quartz glass was used because of its ability to withstand high temperatures and transmit ultraviolet light. Reflections of the incoming laser beams from the backside of the quartz tube were problematic

because the detection wavelength is the same as the laser wavelength for PIV. To alleviate this problem, half of the inside of the quartz tube was sandblasted. The sandblasted quartz tube was used for further measurements for comparability.

2.2.2 Air flow system

The air flow system was modified to utilize a laminar flow element (LFE), to reduce uncertainty and increase repeatability as compared to other flow measurement techniques. The LFE creates a pressure drop (CME Model 10-5-1000A, 0-25.4 cm of H_2O for 0-1000 SLPM) as the laminar flow traverses a honeycomb or other obstruction, which is related to the volume flow rate. The volumetric flow rate is provided as a calibration curve fit from the manufacturer. The formula for the volumetric flow rate Q is given below in Eqn. 2.2:

$$Q = \frac{\Delta P}{\mu}\left(18401.8 + 278573\left(\frac{\rho \Delta P}{\mu}\right) - 692498000\left(\frac{\rho \Delta P}{\mu}\right)^2\right) \qquad \text{Eqn 2.2}$$

where ΔP is the pressure drop across the LFE and μ is the viscosity of the fluid, and ρ is the density of the fluid. The differential pressure was measured using a differential pressure transducer (Omega Model PX 2650, 0-25.4 cm of H_2O). The LFE was utilized to obtain the mass flow rate by measuring the absolute pressure (Sensotech Model FDW 060-E275-02, 0-50 PSIG) and temperature (Omega K-Type Thermocouple). The air flow rate was controlled by a needle valve to allow for finer control as compared to the gate valve previously used. A photograph of the air measuring system is shown in Figure 2.9. Two air pressure regulators (Coilhose Pneumatics, and Watts) were used in series to maintain a constant

pressure as the compressor cycled on and off. A water trap was used to ensure that the air was dry.

2.2.3 Emissions probe

A water cooled stainless steel probe was designed to replace the quartz expansion-cooled probe to ensure that the quenching was adequate. The probe was designed with a tapered head to minimize upstream flow disturbances. The probe contained three concentric pieces of tubing, as shown schematically in Figure 2.10. The inner most tube was the sample tube, the middle tube was a baffle which was not sealed at the probe tip to allow water to flow around it, and the outer tube completed the cooling water's flow path. A photograph of the water cooled probe mounted on a traversing system is shown in Figure 2.11. The probe provides sufficient cooling to allow measurements to be taken at any point in the flame; however the probe can affect the flame by quenching.

2.2.4 Combustion noise measurements

Another new feature of the revised setup was the ability to measure combustion noise and obtain quantitative information on the frequencies observed. The sounds were detected using a phantom powered (Rolls PB23) condenser microphone (Apex 190). A picture detailing the location and orientation of the microphone is shown in Figure 2.12. The condenser microphone was chosen for its signal fidelity over the range of frequencies of interest. The signal was transmitted to the data acquisition system by an 8 m long shielded microphone cable. A second Strawberry Tree Workbench for Windows (ver. 2.01) data acquisition system was utilized to record the data on a high speed

data acquisition card (Flash 12 Model 1) from a T51 terminal board. Data were acquired at 2000 Hz until 2048 samples were collected. These parameters allowed frequencies up to 1000 Hz to be measured with a resolution less than 1 Hz using a fast Fourier transform.

2.3 Optical diagnostic systems at Sandia National Laboratories

Experiments were conducted at SNL to take advantage of pre-existing turnkey optical measurement systems. The initial setup was utilized to perform OH PLIF measurements at SNL, presented in Chapter 5. The modified burner was used for OH PLIF, PIV, and simultaneous OH PLIF and PIV, measurements presented in Chapters 6 and 7. The measurement systems at SNL were monitored using National Instruments Labview software. The air and fuel flow rates were measured and controlled by MKS mass flow controllers. A portion of the air flow was split off to run through the seeding apparatus when performing PIV measurements. The combustor was mounted onto a 3-axis traversing system so that the area of interest in the combustor could be moved into the measurement window. The lasers and other optical equipment were mounted onto a breadboard and remained fixed throughout the experiment. The PIV and OH PLIF apparatuses will be described in detail below.

2.3.1 OH PLIF system

A schematic of the OH PLIF system utilized in these experiments can be seen in Figure 2.13. A Q-switched Nd:YAG laser (Continuum Surelite model SLIII-10) operating at 532 nm was used to pump the dye laser (Continuum Model ND6000) in the OH PLIF system. A beam at 283.556 nm was produced by

frequency doubling the output of the dye laser. This frequency excited the Q1(8) line of the (1,0) band of the $A^2\Sigma \leftarrow X^2\Pi$ electronic transition. The OH fluorescence signal was collected using a 105-mm focal length, f/4.5 UV Nikkor lens, passed through a Schott WG305 colored glass filter, and focused onto an intensified CCD camera. With a magnification of 0.15, the 512 x 512 pixel format provides a field-of-view of 81.9 mm x 81.9 mm with a spatial resolution of 0.16 mm/pixel.

Measurements in a non-premixed CH_4 flame were carried out to quantify the effects of quenching and population fraction on the measurement of OH concentration using laser induced fluorescence (Barlow and Collignon, 1991). Their results showed that the OH PLIF images represented OH mole fraction to within 10% when the Q1(8) line was excited. In order to extend their results to premixed flames, calculated species concentrations and temperature variations were used to simulate changes in the fluorescence signal across the flame due to variations in quenching cross section and temperature. Collisional quenching cross sections for OH based on the work of Paul et al. (1994) were used. The preliminary results showed that the OH PLIF images represent OH mole fraction to within less than 10% for premixed flames.

The sheet forming optics utilized for the PIV beams were also used for the PLIF system. The PLIF laser pulse was coplanar with the two PIV pulses and occurred between them. The variations in the strength of the laser sheet were measured using both a homogenous acetone jet, and by reflecting an image of the laser sheet directly into the camera. The PIV and OH signals were collected

collinearly through the non-sandblasted half of the combustor. The signals were separated using a dichroic mirror placed at a 45^0 angle to the laser sheet, which reflected the OH signal at 305 nm perpendicular to the PIV signal, while the PIV signal at 532 nm passed through the dichroic unaffected.

2.3.2 PIV system

Velocity measurements were obtained using the PIV system shown schematically in Figure 2.14. The light source was a double oscillator chamber ND:YAG laser (Spectra Physics PIV 400) providing 400 mJ/pulses at 532 nm with a repetition rate of 10 Hz. The laser pulses and camera were controlled by a TSI Model 610034 Synchronizer. A cylindrical and a spherical lens were used to form a vertical light sheet 50 mm high and 0.5 mm thick. The time delay between the two PIV pulses was 15 μs. The laser sheet thickness and pulse delay were chosen to minimize lost particle pairs due to the strong out of plane velocity component associated with swirling flows (Ji and Gore, 2002). Hollow alumina spheres with a nominal diameter of 1.6 μm were used for seeding. Alumina is non-catalytic for CH_4/H_2/air reactions, and is not likely to affect the kinetics of the reacting flows. The seed particles affected the flames by increasing the radiative heat transfer. The increased radiation was evident because the flame turned orange with the addition of seed particles. The combustion airflow was divided into two streams after flowing through the mass-controller. The particles were added to one of the streams in a fluidized bed seeder. A cyclonic separator was used downstream of the seeder to remove agglomerations of particles to achieve a

uniform particle size distribution. The seeded air rejoined with the unseeded air prior to entering the premixer.

Images of Mie scattered light from the seed particles were recorded utilizing a digital camera. The camera (TSI Model 630045 Cross-Correlation Camera) had a 1024 by 1024 pixel image, and was placed normal to the laser sheet. An f2.8 lens with a 105 mm focal length was used to collect the scattered light, and the field of view was 30 mm by 30 mm. Background light and flame luminescence were removed using a 10-nm band-pass filter centered at 532 nm. The two images were recorded on sequential frames to allow a cross correlation analysis of the data.

The data were analyzed using PIV LAB 2000 (version 1.50) Matlab routines (Han and Mungal, 2000). This program utilized an iterative algorithm to improve the spatial resolution and decrease the number of incorrect vectors. The first two iterations of the solver used a 64 by 64 pixel region to obtain initial values, and the next five iterations had a 32 by 32 pixel interrogation region, which corresponds to spatial resolution of 0.9 mm. The interrogation regions were 50% overlapped, resulting in a distance between vectors of 0.45 mm. The pixel displacements were converted to units of m/s using the measured field of view and the time between pulses.

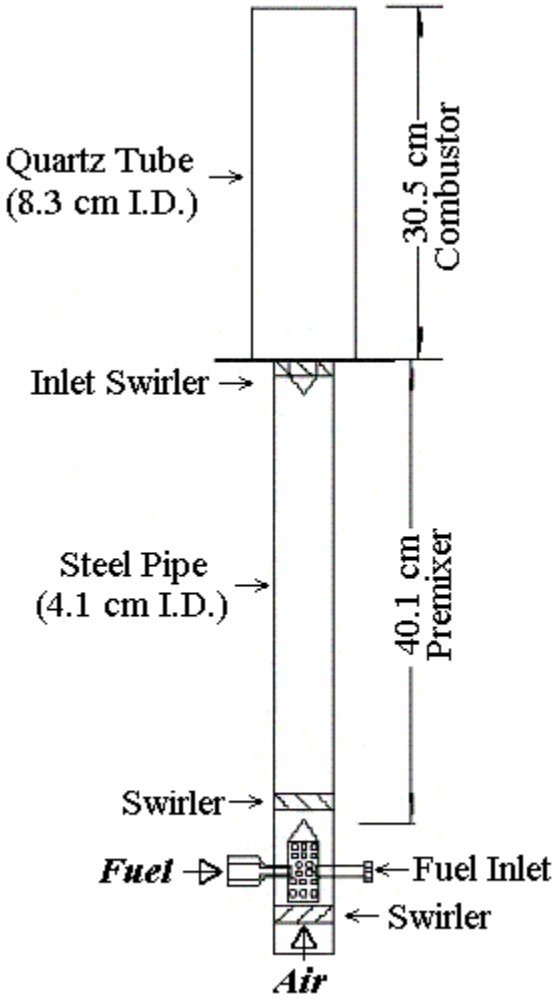

Figure 2.1. Schematic of the initial setup of the experimental swirl burner and premixer. All dimensions are in cm.

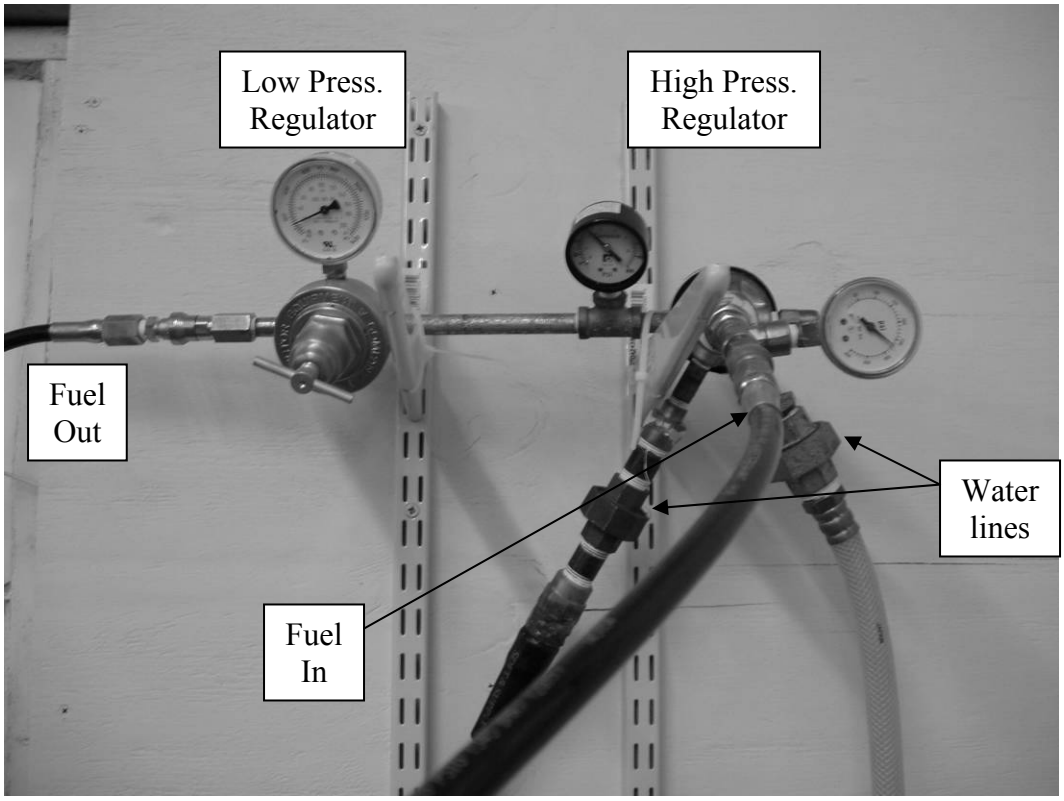

Figure 2.2. Staged pressure regulators used to reduce the pressure of the NG/CH_4 fuel.

Figure 2.3. Photograph of the gas analyzer used in this experiment. The product gas sample enters through the water traps on the right.

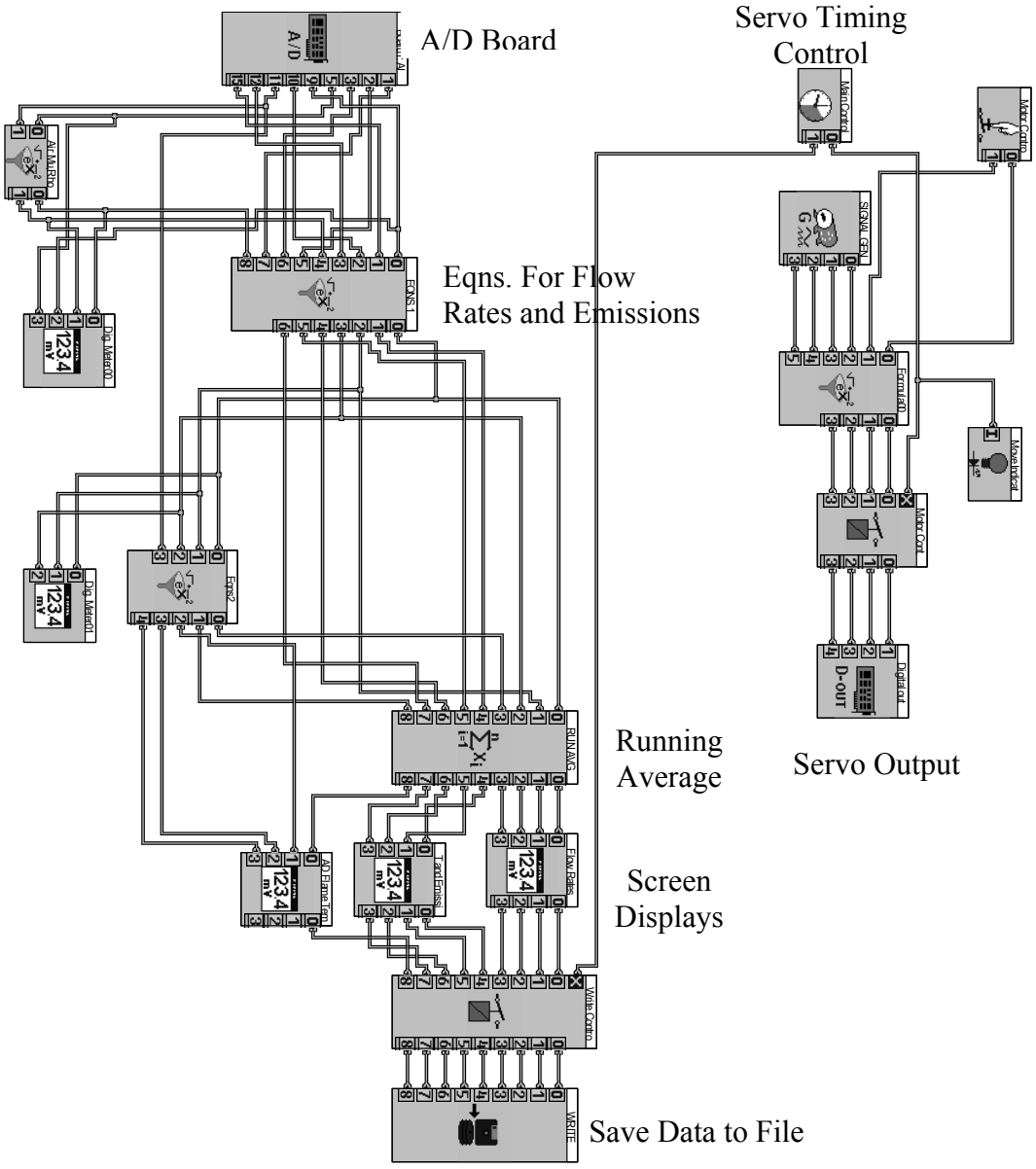

Figure 2.4. The Strawberry Tree worksheet used in these experiments.

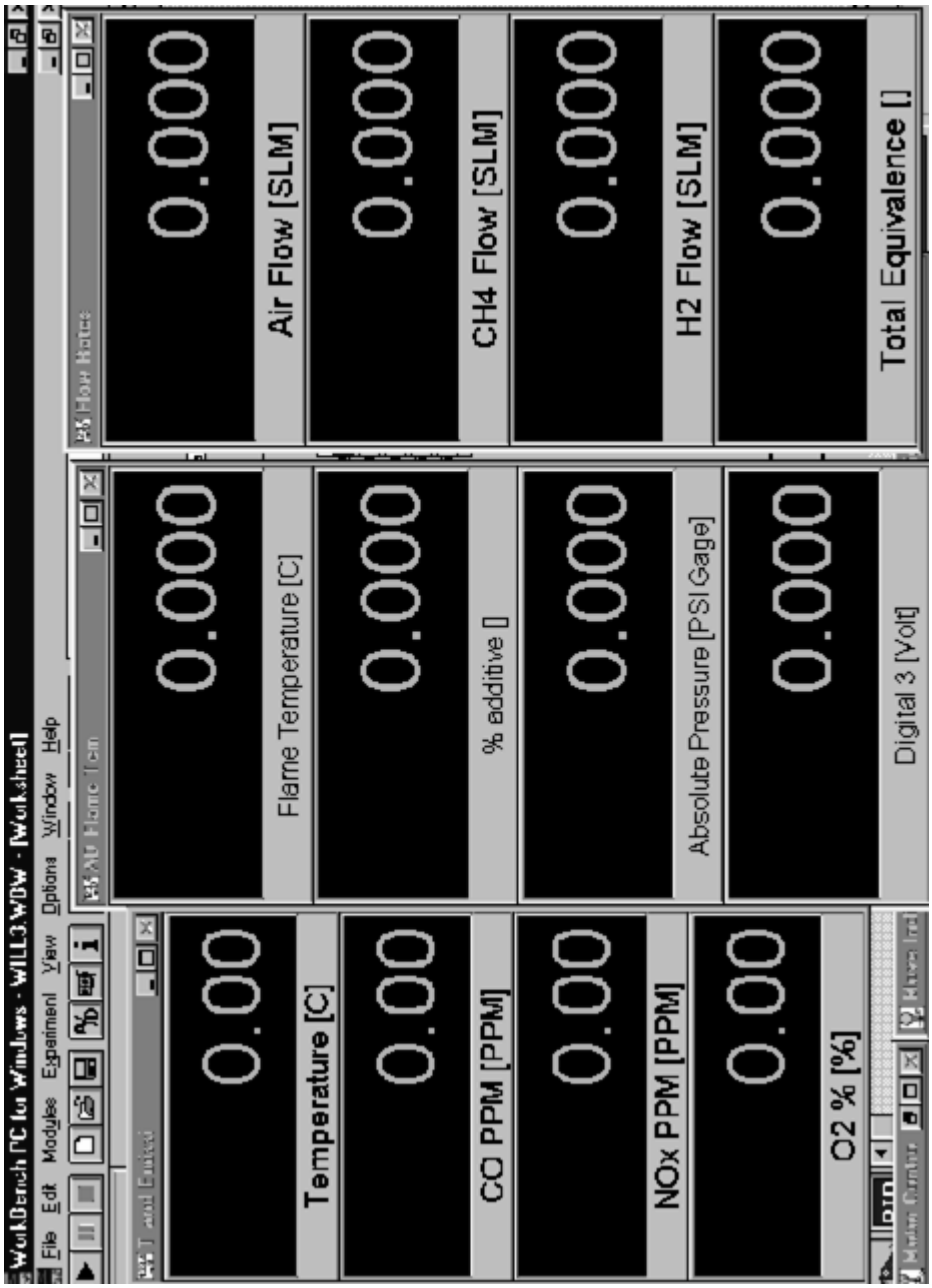

Figure 2.5. Display panel of the Strawberry Tree data acquisition program utilized in this experiment.

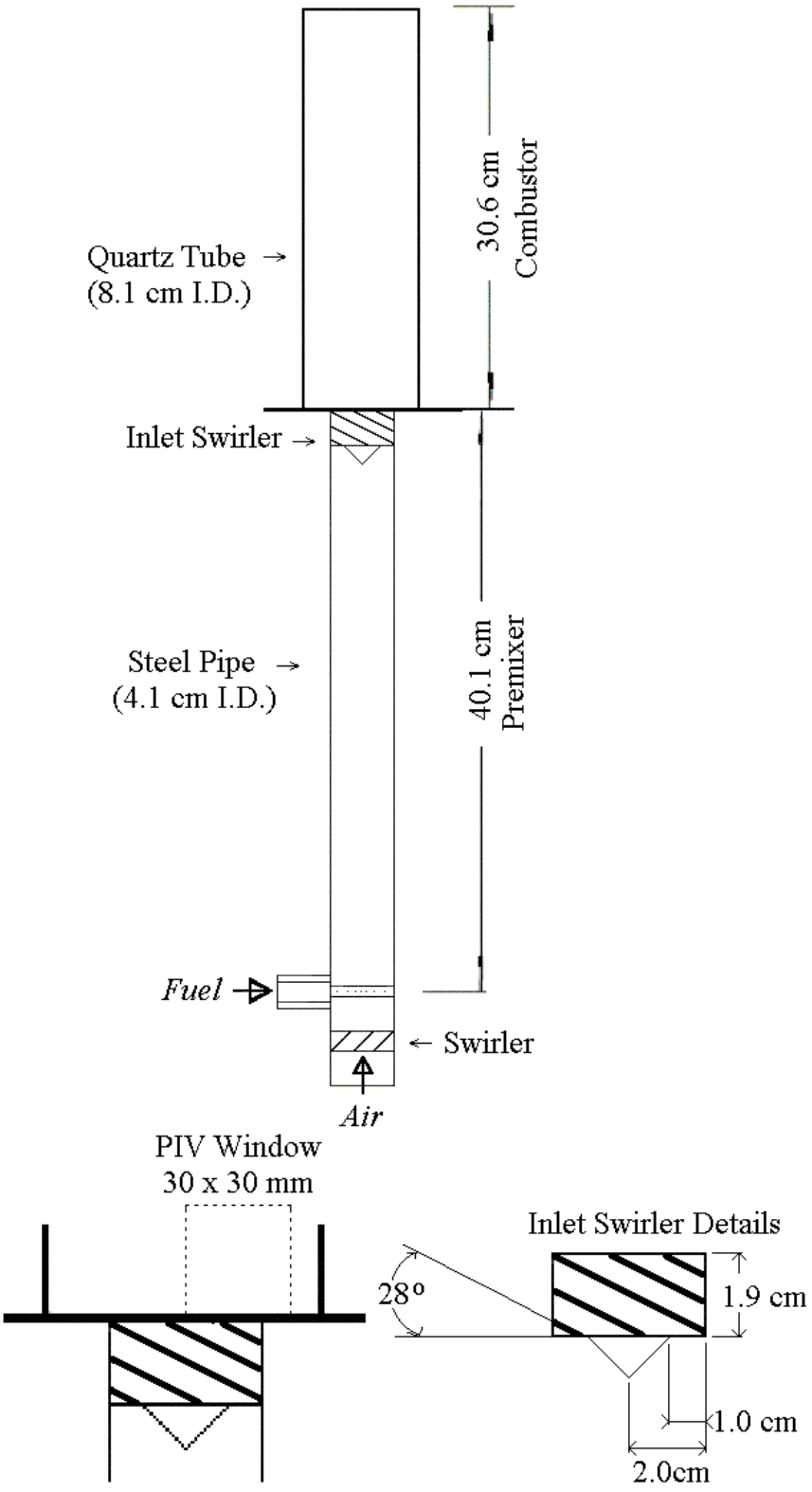

Figure 2.6. Schematic drawing of the modified setup of the combustor and premixer sections with detailed views of the inlet swirler and the PIV window.

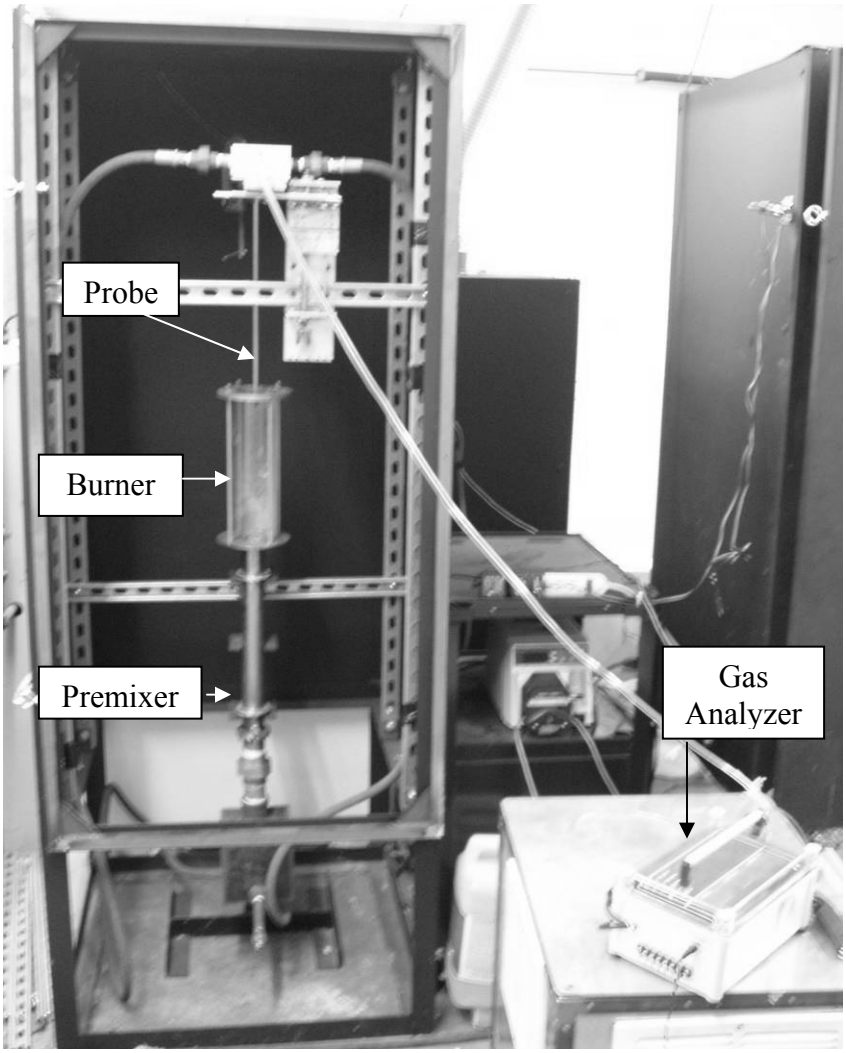

Figure 2.7. Photograph of the modified experimental setup.

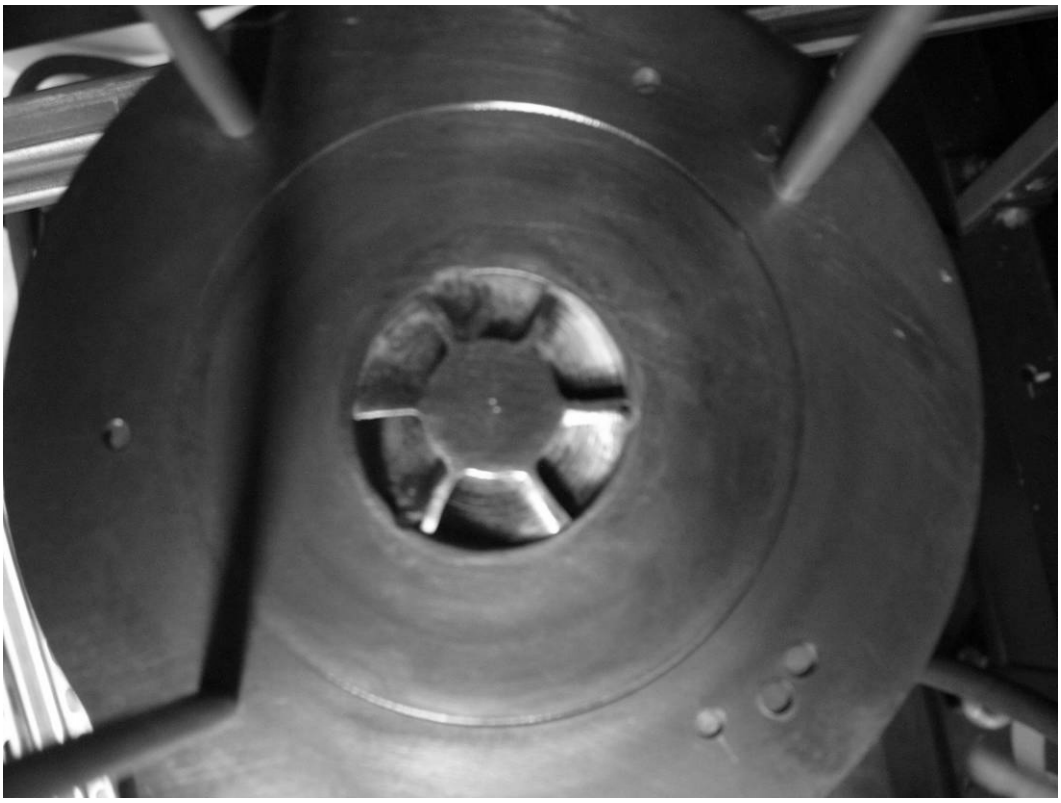

Figure 2.8. Photograph of the inlet swirler taken from above. The circle in the metal plate is a scribe line to center the quartz combustor, which has been removed for viewing.

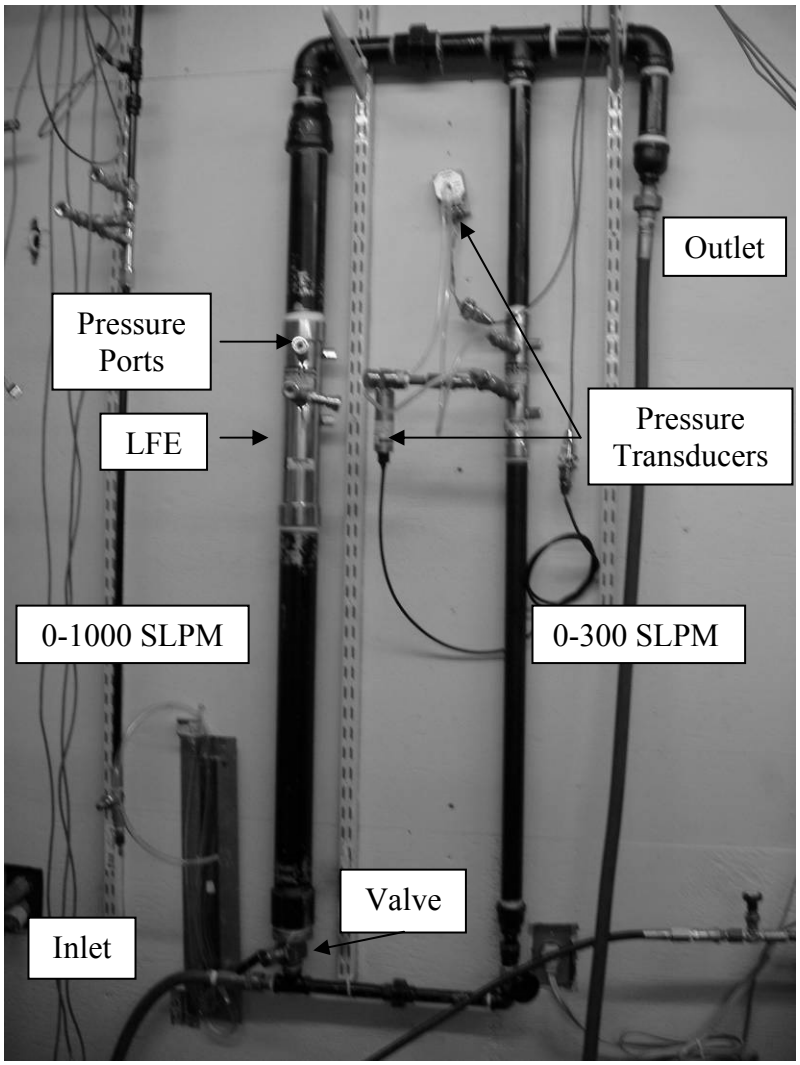

Figure 2.9. Photograph of the airflow measurement system. The pressure transducers are shown attached to the 0-300 SLPM LFE (not used).

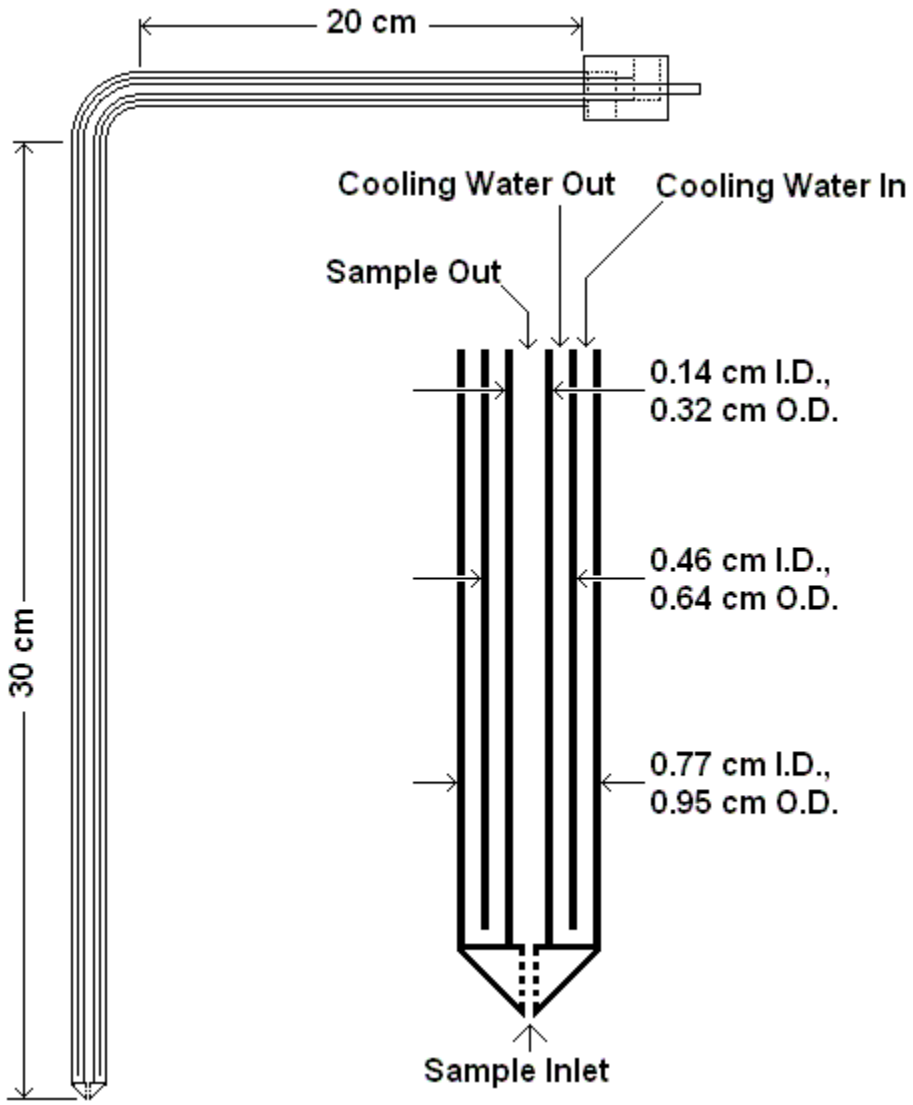

Figure 2.10. Schematic diagram showing water-cooled gas sample probe and expanded view of the probe tip.

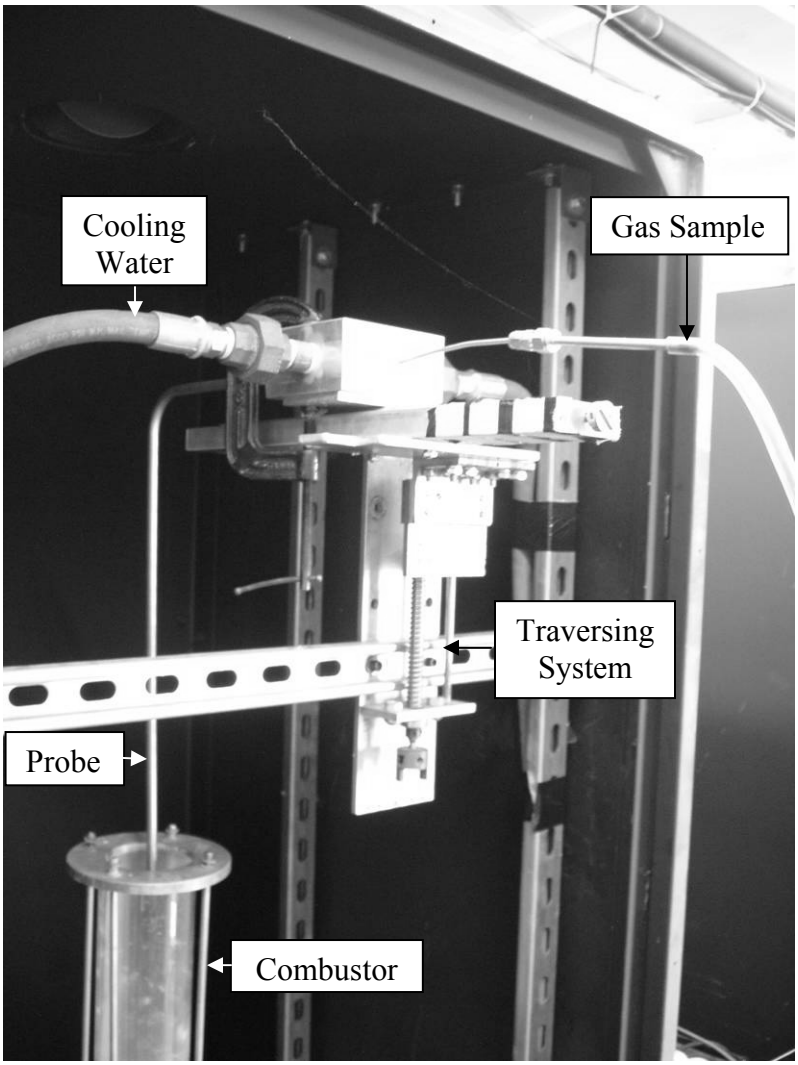

Figure 2.11. A close-up photograph of the water-cooled emissions probe used in the experiment.

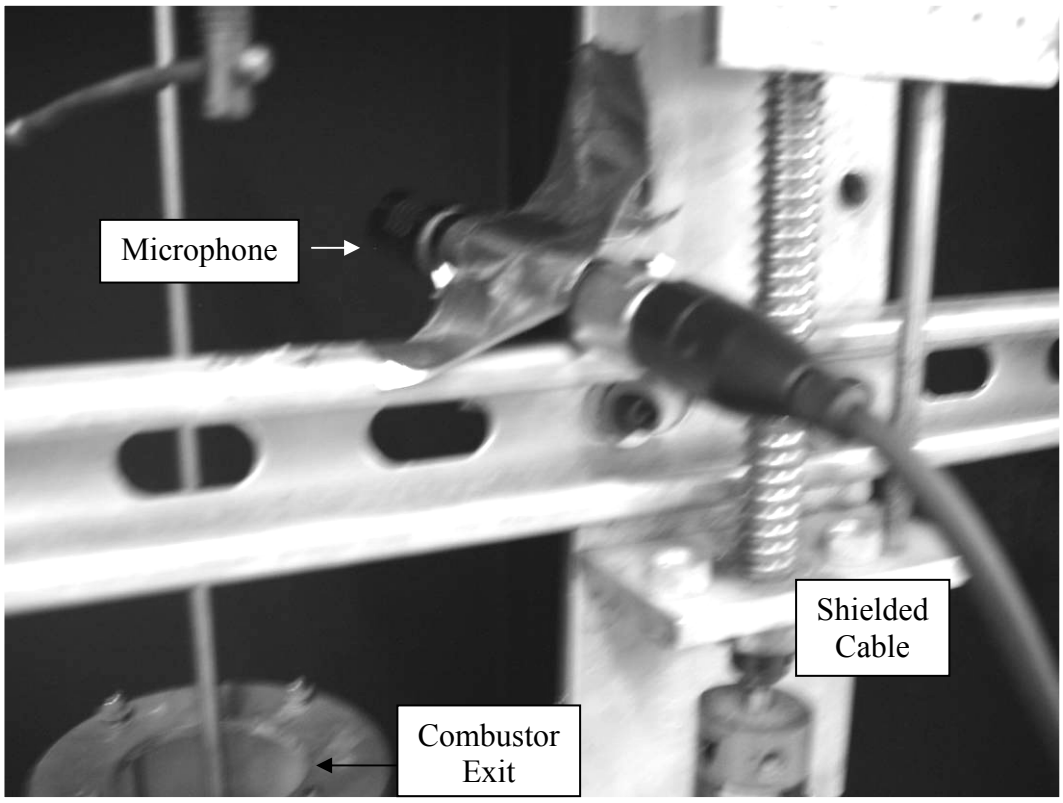

Figure 2.12. A close-up photograph showing the location and orientation of the microphone.

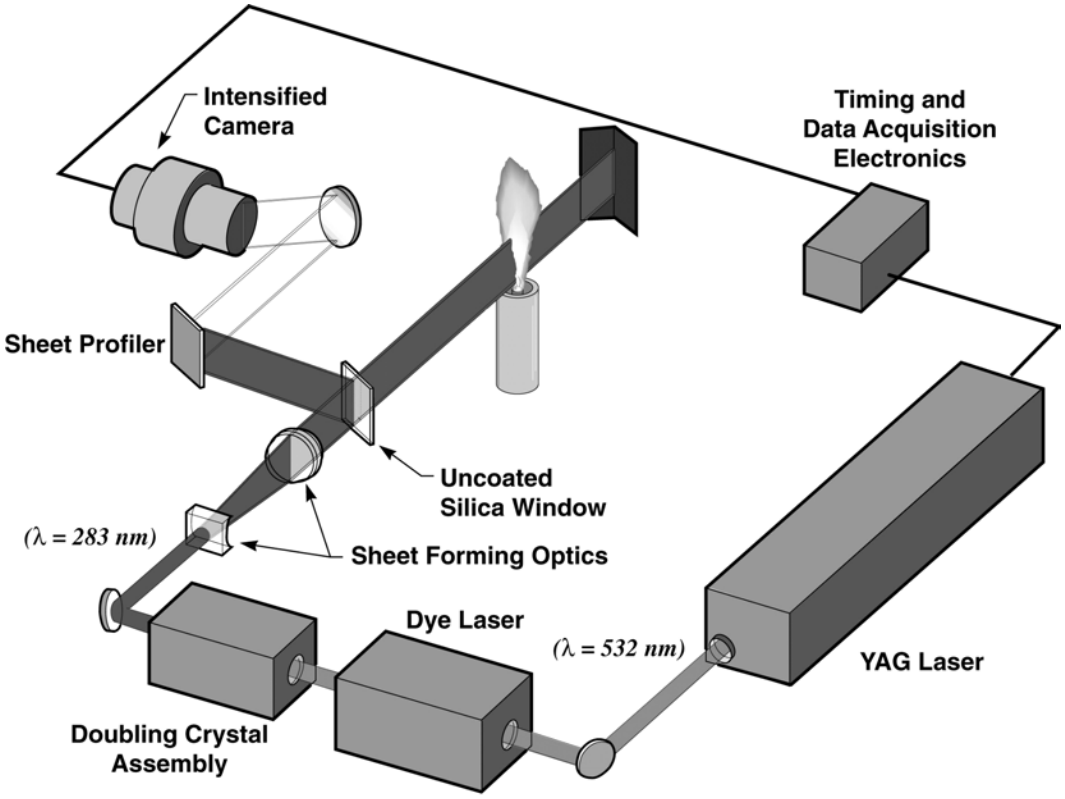

Figure 2.13. A Schematic of the OH PLIF imaging system. Laser sheet profiling using a reflected image of the sheet is shown.

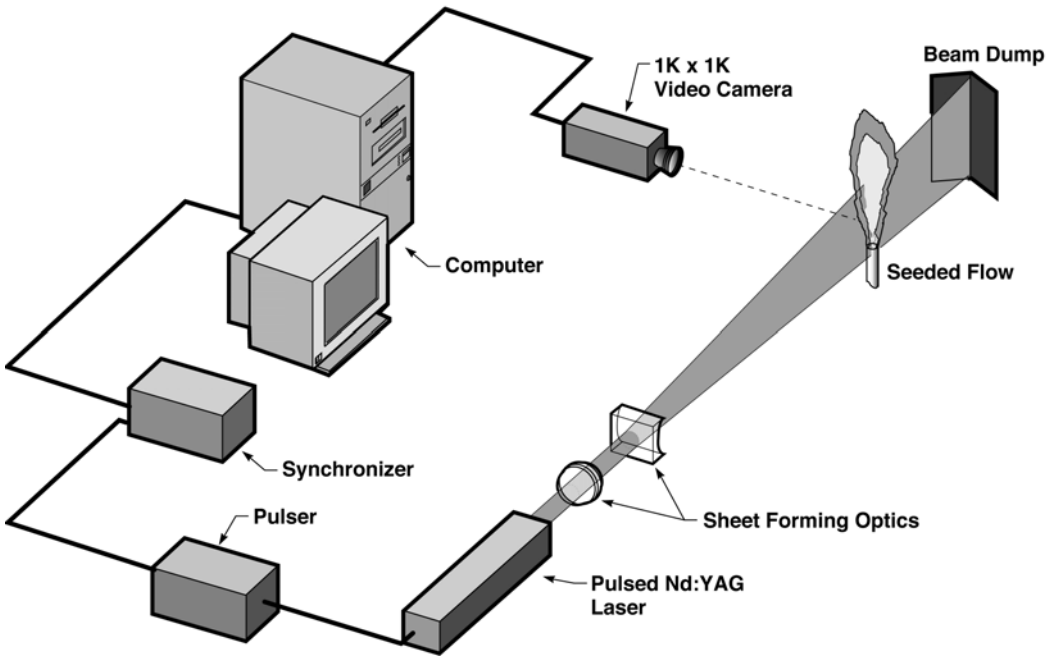

Figure 2.14. Schematic of the PIV imaging system used in these experiments.

CHAPTER 3: EXPERIMENTAL PROCEDURE

The steps utilized to obtain the experimental results will be outlined below. The discussion of the experimental procedure will be divided into sections relating to the different measurements, and the different laboratories in which measurements were taken.

3.1 Starting the system

Many of these tasks can be performed simultaneously with the steps for the gas analyzer calibration described below to minimize the time necessary to start the experiment.

1. Turn on the air compressor using the following steps.
    a. Make sure the valves for devices attached to the air lines are all closed.
    b. Check the oil in the compressor using the dipstick located on the side of the compressor and add any if needed. Replace the dipstick.
    c. Open the ball valve on the front of the air storage tank attached to the hose. There should be a hissing sound as the air fills the hose.
    d. Turn the electrical switch to the on position; the compressor will usually cycle on at this point and it is loud.
2. Start the data acquisition program, Strawberry Tree, by launching it from the desktop icon, and open up the file appropriate for the experiment.
3. Turn on the hot water heater using the following steps.
    a. Turn on the water flow at the spigot where the supply hose attaches to the building.

b. Open the valve that controls the flow of water to the NG/CH_4 pressure regulator and allow the water to flow until the sputtering noise stops and a steady stream of water is leaving the heater. Close the valve so the heater can raise the temperature of the water to the required temperature.

c. Carefully plug in the water heater's cord into the proper electrical outlet located next to it on the wall, which is a 240V outlet.

d. Allow at least 30 minutes for the water heater to warm up before using.

3.2 Lean blow out limit testing

In order to determine the lean blow out (LBO) limit, it is necessary to reduce the adiabatic flame temperature the system is operating at in a slow and controlled fashion so the exact point at which the flame becomes unstable or blows off can be recorded. It is necessary to maintain the experimental variables of total flow rate and fuel composition at the proper values while making these changes to the temperature. The change in temperature can be achieved by either raising the air flow rate, or reducing the fuel flow rate. The early LBO experiments were conducted by varying the air flow rate as described below; the later experiments were conducted by varying the fuel flow rates in a similar fashion.

1. Perform a preliminary LBO test to determine the temperature at which the flame blows off at the desired total reactant flow rate.

2. Set the fuel flow rate to a value which should cause LBO around the desired total reactant flow rate using the rough test as a guide. Make sure that the fuel composition is correct, and remains constant throughout the following steps. The air flow rate will need to be below the flow rate at which LBO is expected.
3. Increase the air flow rate by adjusting the control valve in the air line appropriately.
4. When the flame is the full length of the combustor slowly increase the airflow in small increments and wait several seconds for the system to stabilize before further increasing the air flow rate.
5. Record the flame temperature, flow rates and equivalence ratio when the flame is unable to continue combustion.

3.3 Emissions measurements

3.3.1 Calibrating the gas analyzer

1. Turn on the gas analyzer and let if run for at least 1 hour drawing in air to warm up.
2. After the gas analyzer has warmed up, the NOx and CO outputs must be zeroed using the zero adjustment knobs on the side of the analyzer, and the O_2 sensor should be spanned to read 20.9% using the knob on the side of the analyzer. If measurements are to be made using the electronic outputs, then the device should be zeroed with respect to the electronic outputs instead of the digital display on the device.

3. Turn the control knobs on the pressure regulators of the calibration gas cylinders to the left until all tension is relieved from the mechanism, so that the outlet pressure of the regulator is nearly zero. The cylinder should also be stored this way.
4. Open the valve on the cylinder of the calibration gas. The pressure gage on the regulator should read the cylinder pressure.
5. Locate the custom-made connector which has a piece of metal tubing on one end and a male quick connect fitting on the other. Attach the connector to the plastic sample hose of the gas analyzer by sliding the plastic hose over the metal tubing.
6. Plug the male quick connect fitting on of the adapter into the female fitting on the outlet of the pressure regulator of one of the cylinders.
7. Immediately begin turning the pressure adjustment control of the pressure regulator to the right to raise the outlet pressure until gas begins to flow.
8. The flow rate of the gas needs to be adjusted so that the rotameter on the side of the analyzer has its float at the top of the chamber. The suction pump on the gas analyzer must remain running; it will stop if the flow rate is too high. If this occurs, reduce the flow rate slightly until the pump restarts.
9. Allow the gas analyzer to run until the output reaches a steady value. This should take at least 15 minutes.
10. Remove the water proof cover on the top of the analyzer by loosening the four screws at the corners that hold it on and lifting the cover off vertically.

11. The gain settings are controlled by two screws, one for the CO and one for the NOx located on the face plate of the instrument.
12. Adjust the screw until the output value matches the value on the calibration certificate of the cylinder, either 198 PPM or 200 PPM depending on the calibration gas.
13. The O_2 reading should be zero as there is no O_2 in either of the calibration gasses. If it does not, follow the steps in the owner's manual to correct it.
14. Close the valve on the cylinder and allow the pressure to be bled off by the analyzer. When the pressure has been bled off the sound of the suction pump will change. Immediately disconnect the gas analyzer from the tank by pulling apart the quick connect fittings.
15. Adjust the pressure output knob of the regulator until the tension is removed from it. This is the correct way to store the device.
16. Repeat steps 4-15 with the other calibration gas cylinder to span the other reading.
17. After spanning both the NOx and CO sensors, allow the analyzer to draw in air until the readings stabilize. The NOx and CO should both read nearly zero at this time.
18. Turn the zero knobs for both the NOx and CO to zero them again. If one of the values is significantly off from zero it may be necessary to span it and zero it again using the steps outlined above. However, common use and calibration of the gas analyzer maintains the calibration of the instrument, so this should be rarely necessary.

3.3.2 Obtaining emissions measurements

1. Once the analyzer has been calibrated leave it running for the rest of the experiment.
2. Attach the plastic sample hose to the probe so there is a snug fit.
3. Make sure to allow enough time at a desired experimental point for the readings of the analyzer to reach a steady value.
4. The data can either be recorded by hand or by using the automated program which also advances the probe periodically to scan a line of data across the combustor,
5. If the quartz glass probe is being used, there are no further steps needed.
6. If the water cooled stainless steel probe is being used, place the outlet hose for the probe cooling water outside of the lab. The outlet hose is the blue hose coiled underneath the experiment which has and unattached threaded fitting.
7. Turn on the cooling water for the probe using the appropriate valve on the hot water heater until there is a steady stream exiting the blue probe cooling water outlet hose. **NOTE:** The cooling water must be turned on before the burner is lit or else the probe will melt.
8. The data can now be taken in a similar manner as above in steps 1-4.

3.4 OH PLIF measurements

1. Put on safety goggles to prevent exposure of the ultraviolet (UV) laser light to eyes and make sure that safety interlocks in the room are working properly. Caution is needed as high powered UV laser light is invisible and can cause severe eye damage in less time than it takes to blink.

2. Turn on the cooling water to the laser.
3. Place a beam block in the path of the laser light to prevent stray radiation during subsequent steps of the experiment. Turn on the YAG laser and let it "simmer" to warm up the lasing element properly for 30 minutes.
4. Turn on the CCD camera so that the temperature of the sensor element can be reduced to the proper temperature for measurement. This is important because the dark field correction which accounts for the thermal radiation detected by the sensor is obtained at a specific temperature.
5. Open the appropriate LABVIEW programs to control the experiment and the OH PLIF data acquisition system.
6. Line up the experiment as best as possible with the opening in the enclosure where the laser light emerges.
7. Remove the quartz tube and place a piece of UV sensitive detecting paper mounted on a metal block onto the flat metal plate at the combustor inlet.
8. Stop the laser and remove the beam block from the laser's path.
9. Restart the laser and let it run a few times, there should be popping sounds as the laser hits the sheet.
10. Use the location of the marks on the detecting paper to align the beam with the center line of the combustor by moving the experiment on the traversing system.
11. Place a target image in place of the UV sensing paper and use it to focus the camera and adjust the field of view side to side, up or down, and the size. The

target should have graduations on it so that the dimension of the images will later be known.

12. Start the combustor using the appropriate program and set it to the desired test conditions.
13. Remove beam block from the path and take data using the Labview control software. Limit the number of images taken at one time to 200 because all the data is saved to one file and this prevents excessive file size.

3.4.1 Obtaining OH PLIF corrections

1. The dark field image which is caused by thermal radiation can be obtained by acquiring images with the lens cap on when the detector is at the operational temperature.
2. The flat field correction accounts for the differences in pixel sensitivity of the detector. The flat field correction can be obtained by acquiring data of several pieces of paper placed in front of a bright light; the diffuse light shining through the paper provides a good uniform illumination to measure.
3. A correction for the beam intensity is also obtained since the OH signal can depend on the laser intensity. This correction was obtained two ways, first by reflecting a small portion of the beam from a piece of glass in the beam, and second using scattering off air.
    a. To correct for the beam strength using a partial reflection, place an uncoated piece of silica glass in the beam's path and use mirrors to reflect the light into the camera. This method lowers laser intensity

and field of view, but offer real time beam corrections for shot to shot variation.

b. To use the method for scattering off air, enclose the image area, preferably with black velvet, to prevent any ambient light from entering. Acquire images with the laser running and illuminating air. This data can be summed over a period of time to provide the correction based on relative beam strength.

3.5 Velocity measurements using PIV

1. Put on safety goggles to prevent exposure of green laser light (532 nm) to eyes and make sure that safety interlocks in the room are working properly. Caution is needed as high powered lasers can cause severe eye damage in less time than it takes to blink (even from specular reflections off objects).
2. Turn on the cooling water supply to the laser.
3. Place a beam block in the path of the laser light to prevent stray radiation during subsequent steps of the experiment. Turn on the PIV YAG laser and let it "simmer" to warm up the lasing elements properly for 30 minutes.
4. The first step is to align the experiment with the beam operating the lasers at low intensity. It is possible to see where the beam strikes the surface of the glass cylinder and align the experiment accordingly so the beams pass through the centerline of the combustor. The alignment can also be accomplished by viewing the reflection off the metal inlet plate of the combustor.
5. The two laser beams must overlap with each other to obtain data. To verify this, place a piece of light sensitive paper at an oblique angle to the beam in its

path. The angle helps to accentuate any difference in the positions of the two beams. By adjusting the optics inside of the laser, the two beams can be made to overlap. This method is quick and works when the laser sheet is wide as in this case.

6. A target image should be taken with the PIV camera to focus the image and to verify the field of view and the size of the image. The number of pixels per mm will later be determined from this image.
7. If further focusing is required, smoke can be illuminated using the laser.
8. The pulse delay can be set using the synchronizer, and should be checked using an oscilloscope, and compared to the frames of the camera to verify that the correct image is being recorded on the correct frame.
9. The laser pulses need to be adjusted to the same amplitude before taking measurements. This can be accomplished by using a partially shielded photo detector with its signal monitored by an oscilloscope. The signal will appear as two waves which are separated in time by the pulse delay. Adjusting the power levels until the two peaks are equal will guarantee the same amplitude laser power.
10. The quartz glass tube can be placed on the combustor. The system is ready to be utilized, and the operating condition can be set using the Labview software to get the system running.
11. Activate the focusing mode on the TSI control computer which operates the PIV system. The screen will show the image and the laser will fire.

12. Adjust the control knob on the particle seeder while watching the focusing image.
13. When there is a sufficient level of seeding, immediately begin recording and take 10 PIV image pairs. The seed will quickly obscure the glass causing low quality images if the system is operated for too long, thus limiting the number of images.
14. Shut the seed control valve off and turn off the fuel flow if a reacting flow case was being studied.
15. Allow the combustor to cool before proceeding.
16. Remove the combustor and clean with water or cloths to remove the seed fouling the wall.
17. Repeat steps 10 – 16 until a sufficient set of data is obtained.

3.6 Simultaneous PLIF and PIV measurements

1. Previous safety precautions need to be followed; glasses acceptable for the green laser light will also block the UV light.
2. A dichroic mirror is placed in between the PIV camera and the combustor at a 45^0 angle to the beam. This mirror bounces the PLIF image so that it can be recorded at 90^0 from the PIV image allowing both images to be recorded from one side of the combustor.
3. Focusing of the images and adjusting the fields of view is accomplished using a target shot, which also provides location and image size information. When using a mirror it is important to verify the orientation of the images as well.

4. After both the PLIF and PIV lasers are warmed up, the beams need to be aligned so they are coplanar.
5. The method using the photo sensitive paper described in the PIV section will again be used, however this time one of the green PIV beams and the UV beam will be aligned with each other. The second PIV beam will also be aligned with the first PIV beam using this method if it has not already been done.
6. The timing of the beams needs to be verified using an oscilloscope to observe the synchronizer pulses. The PLIF laser pulse should fall in between the two PIV pulses so that the measurements are in fact simultaneous.
7. It is necessary to verify that the images on both the PIV computer and the PLIF computer are being recorded simultaneously. This can be accomplished by taking a set of data where the field of view is repeatedly blocked by an object. The blocked and unblocked images should correspond with each other on both computers. It may be necessary to reduce the data rate in order to synchronize the two systems.
8. Again, the data must be acquired in small sets due to the seed build-up on the quartz wall.
9. It is not necessary to get as many simultaneous data points as with individual PIV or PLIF measurements, since average data will be obtained from the individual measurements only.

3.7 Combustion noise measurements

1. Attach the microphone near the combustor outlet, but not directly in the path

as the high temperature of the exhaust is an issue.

2. Connect a shielded phantom power cable to the microphone and a phantom power unit.
3. Attach wires to the appropriate signal outlet terminals on the power unit and to the leads of the data acquisition system.
4. Start the appropriate Strawberry Tree software, and when the experiment is running take a burst of data. This is accomplished using the start all logs and stop all logs commands sequentially.
5. In order to process the data with a fast Fourier transform algorithm it is necessary that the sampling frequency be known (2000 Hz), and the number of samples is a multiple of two (2048). These frequency and number of samples are the defaults in the Strawberry Tree software program written for this experiment.

CHAPTER 4: DATA PROCESSING AND ANALYSIS

This chapter is divided into several sections detailing the data processing and analysis techniques that were used to obtain the results presented in the next chapters.

4.1 Equivalence ratios of multi-component fuels

When working with alternative fuels care must be taken in how one defines and calculates the equivalence ratio. According to the standard definition, the equivalence ratio is the ratio of the stoichiometric to actual air to fuel ratios given in Eqn. 4.1 below.

$$\Phi = \frac{\left(A/F\right)_{Stoich.}}{\left(A/F\right)_{Actual}} \qquad \text{Eqn. 4.1}$$

From Eqn. 4.1, it is apparent that the definition is based on O_2 consumption in the air. Defining an equivalence ratio for alternative fuels in this same manner is important for consistency with established definitions. The stoichiometric air to fuel ratio is found by balancing the chemical equation for one mole of fuel, which is further divided into the fuel components. For example consider the 40% H_2-enriched CH_4 case. The coefficients for the fuel components are 0.6 CH_4 and 0.4 H_2. Defining the fuel in this manner preserves the standard definition of equivalence ratio, while the variation in fuel composition is accounted for.

The procedure for finding the equivalence ratio can be taken a step further. First, the stoichiometric equation is balanced with algebraic constant representing the concentration of the components in the fuel. In the example above, the coefficients for the fuel components will be (1-X)CH_4 and XH_2 where X is the

mole fraction of H_2 in the fuel. The chemical reaction for this case is shown below in Eqn. 4.2; all the N_2 in the air remains as N_2, and the coefficient for the air is unknown.

$$(1-X)CH_4 + (X)H_2 + (\ )(O_2 + 3.76N_2) \Rightarrow (1-X)CO_2 + [2(1-X)+X]H_2O + ... \quad \text{Eqn. 4.2}$$

The equation can be solved because the number of oxygen atoms in the reactants must be equal to the number in the products. This is a statement of the O_2 balance which is expressed mathematically in Eqn 4.3.

$$(\ ) = (1-X) + \tfrac{1}{2}[2(1-X)+X] = \left(2 - \tfrac{3}{2}X\right) \quad \text{Eqn. 4.3}$$

The coefficient for the O_2 is multiplied by 4.76 to account for the N_2 present in air, giving the air to fuel ratio. Therefore, the stoichiometric air to fuel ratio can be quickly calculated for a given primary and secondary fuel, CH_4, and H_2, respectively. The actual air to fuel ratio is calculated from flow rate measurements, which are used to calculate the equivalence ratio in the experiment. This method works only if the additive is neutral, or consumes O_2 as it reacts. This method will produce equations which are all of the same form after simplification and contain two coefficients. The formula for calculating the stoichiometric air to fuel ratio using these coefficients is given by Eqn. 4.4:

$$\left(A/F\right)_{Stoich.} = (C1 + C2 * X) * 4.76 \quad \text{Eqn. 4.4}$$

where C1 and C2 are the coefficients found by the O_2 balance described above for different fuel mixtures. In the example above, C1 is 2 and C2 is -1.5. Coefficients for some of the fuel mixtures used in these experiments are provided below as a reference in Table 4.1.

Table 4.1: Coefficients utilized to calculate the stoichiometric air to fuel ratio.

Primary Fuel	Additive Fuel	Coefficient C1	Coefficient C2
CH_4	H_2	2	-1.5
C_3H_8	H_2	5	-4.5
CH_4	N_2	2	-2
CH_4	C_3H_8	2	3
C_3H_8	CH_4	5	-3

4.2 Adiabatic flame temperature calculations

Combustion performance of different fuel mixtures was compared for a given calculated adiabatic flame temperature. The adiabatic flame temperature is the temperature attained if all reactions reached equilibrium, in a system that was completely insulated so that no heat was lost. This is a theoretical temperature because reactions do not usually proceed to equilibrium, but rather become quenched due to heat loss. Even though the actual flame temperatures are slightly lower, the adiabatic flame temperature will allow for comparisons to be made between different fuels in a consistent relevant manner. The flame temperature is an important parameter because it is directly related to the pollutants formed and the engine power developed.

The adiabatic flame temperature can be calculated if the product species are known or guessed. The preferred method for systems containing large numbers of species is to minimize the Gibb's free energy, which occurs at equilibrium. The program used to calculate the adiabatic flame temperature is the

CHEMKIN-II chemical kinetics package (Kee et al., 1989). The 53 species contained in GRI-MECH 3.0, shown in Table 4.2 below, were used to ensure that the flame temperature accounted for species dissociation, which tends to lower the temperature due to its endothermic nature.

Table 4.2: The species used in the adiabatic flame temperature calculations.

H2	H	O	O2	OH	H2O	HO2	H2O2
C	CH	CH2	CH2(S)	CH3	CH4	CO	CO2
HCO	CH2O	CH2OH	CH3O	CH3OH	C2H	C2H2	C2H3
C2H4	C2H5	C2H6	HCCO	CH2CO	HCCOH	N	NH
NH2	NH3	NNH	NO	NO2	N2O	HNO	CN
HCN	H2CN	HCNN	HCNO	HOCN	HNCO	NCO	N2
AR	C3H7	C3H8	CH2CHO	CH3CHO			

A special driver program was utilized which called the CHEMKIN subroutines repeatedly for a range of air to fuel ratios and saved the results to a file. The adiabatic flame temperatures were plotted against the air to fuel ratio starting with the highest flame temperature at stoichiometric conditions and continuing down to lean values below the lean blow out point. The data were found to fit well with a power law curve that resulted in r-squared coefficients of 0.9995 and greater indicating a nearly perfect curve fit. The form of the temperature curve fit equations is given below in Eqn. 4.5.

$$T_{AD} = D1 \bullet [AFR]^{D2} \qquad \text{Eqn. 4.5}$$

The coefficients D1 and D2 are listed in Table 4.3 for different fuels. The calculation assumed an initial mixture temperature of 300K and a constant pressure of 1 Atm.

Table 4.3: Curve fit coefficients utilized in flame temperature calculations of the form of Eqn 4.3. The fuels contain a balance of CH_4 unless otherwise specified.

Fuel Composition	**Coefficient D1**	**Coefficient D2**	**Least Squares R^2**
100% CH_4	12319	-0.7907	0.9997
100% C_3H_8	26624	-0.7962	0.9998
20% N2	10558	-0.8025	0.9997
30% N2	9607.7	-0.8093	0.9997
40% N2	8586.9	-0.8163	0.9998
20% CO_2	10343	-0.7973	0.9997
30% CO_2	9311.9	-0.8013	0.9997
40% CO_2	8234.2	-0.8055	0.9997
20% O_2	10512	-0.8013	0.9997
30% O_2	9554	-0.8078	0.9997
40% O_2	8529.6	-0.8145	0.9998
10% H_2	11753	-0.7946	0.9997
20% H_2	11302	-0.8030	0.9997
30% H_2	10759	-0.8099	0.9997
40% H_2	10181	-0.8171	0.9998
12.1% H_2	11624	-0.7956	0.9997
21.63% H_2	11005	-0.7980	0.9997

29.28% H_2	10491	-0.8000	0.9997
10% C_3H_8	14025	-0.7954	0.9997
20% C_3H_8	14845	-0.7800	0.9998
30% C_3H_8	17390	-0.8027	0.9997
40% C_3H_8	18623	-0.7986	0.9997
50% C_3H_8	19702	-0.7932	0.9998
10% H_2 in C_3H_8	24681	-0.7956	0.9998
10% H_2 in C_3H_8	22599	-0.7937	0.9998
10% H_2 in C_3H_8	20660	-0.7940	0.9998
10% H_2 in C_3H_8	18589	-0.7930	0.9998

4.3 Opposed flow flame calculations

When modeling combustion, one must not only calculate the chemical kinetics at each point throughout the domain of interest, but also the flow-field. This complication arises because the differential equations governing the flow and the chemical kinetics are coupled and must be solved simultaneously. For this reason, it is often preferred to study combustion in the case of a simple flow-field. The opposed flow configuration was selected because the flow-field is known apriori via exact solution to the Navier Stokes equations. The geometry used for the calculation in this report is that of planar stagnation flow, characterized by a planar jet impinging upon a stagnation plane and spreading outwards. A cross sectional view of a planar counter flow premixed flame is shown in Figure 4.1. Because the reactants are premixed, two symmetric flames form, one on each side

of the stagnation plane. Schlichting (1987) presents a discussion of a planar jet impinging upon a wall and diverging, also known as the Hiemenz flow. The Hiemenz flow is similar to opposed jets, however there is slip at the centerline boundary for an opposed jet configuration because of the absence of a wall. Since the flow-field is known, the analysis is greatly simplified, especially because the centerline for the flow is a 1-D domain.

Strained flame calculations were performed using B. Rogg's RUN-1DL laminar flame code (ver. 12.2, 1995). The flame strain rate is defined as the velocity gradient in the direction perpendicular to the stagnation plane which occurs directly upstream of the flame. The subroutines modeled strained combustion between two opposing planar premixed jets. Half of the domain (one side) was modeled taking advantage of the symmetry occurring at the stagnation plane thereby reducing the computational effort. The governing equations for this model are the conservation equations for total mass, momentum, energy, and species mass. The diffusion effects in strained flames are negligible, and have been omitted. The formulation of the governing equations listed below is taken from the RUN-1DL User Manual (Rogg and Wang, 1995). For each quantity (ϕ), a convective-accumulative operator (L) is defined in the form of Eqn. 4.4 below.

$$L(\phi) \equiv \frac{\partial(\rho\phi)}{\partial(t)} + \frac{\partial(\rho v\phi)}{\partial(y)} + \rho G\phi \qquad \text{Eqn. 4.4}$$

The L operator has terms that account for the accumulation of a quantity with time due to unsteady flow, and the convective inflow of a quantity. Here ρ is the density, v is the flow velocity perpendicular to the stagnation plane, t is the time,

y is the coordinate direction orthogonal to the stagnation plane, and G is a velocity term (u/x) where u and x are parallel to the stagnation plane. The governing equations for mass, momentum, energy, and species mass are, respectively, presented in terms of the L operator below. Equation 4.7 is the Continuity Equation. Equation 4.8 is the Conservation of Momentum equation, and Eqn. 4.9 is the temporal forcing term used in Eqn. 4.8. Equation 4.10 is the Conservation of Energy equation, and Eqn. 4.11 is representative of the governing equation of species mass.

$$L(1) = S_v \qquad \text{Eqn. 4.7}$$

$$L(G) = \frac{\partial}{\partial y}\left(\mu \frac{\partial G}{\partial y}\right) - \rho G^2 + P'(t) + S_m \qquad \text{Eqn. 4.8}$$

$$P'(t) \equiv \rho_\infty \left(\frac{da}{dt} + a(t)^2\right) \qquad \text{Eqn. 4.9}$$

$$c_p L(t) = \frac{\partial}{\partial y}\left(\lambda \frac{\partial T}{\partial y}\right) - \frac{\partial T}{\partial y}\sum_{i=1}^{N} c_{pi}\left(\rho Y_i V_i\right) - \sum_{i=1}^{N} h_i \omega_i + \frac{\partial p}{\partial t} - \frac{\partial q_r}{\partial y} + S_e \qquad \text{Eqn. 4.10}$$

$$L\left(Y_i\right) = -\frac{\partial \rho Y_i V_i}{\partial y} + \omega_i + \left(\delta_{id} - Y_i\right) S_v \qquad \text{Eqn. 4.11}$$

The source terms for mass, momentum and energy in two phase models are S_v, S_m, and S_e respectively. These terms are zero for the gas phase model used in this report. Here, μ is the dynamic viscosity; c_p is the mixture specific heat, and λ is the mixture thermal conductivity. The mass fraction of the ith species is represented by Y_i, its diffusion velocity is V_i, its enthalpy is h_i, and its mass rate of production is ω_i. The specific heat and enthalpy of each species are calculated using the temperature dependent curve-fit data from JANNAF tables (Rogg and Wang, 1995). The mixture's viscosity and thermal conductivity are calculated from mixture weighted values of the properties of the species. The symmetry

boundary conditions were modeled by forcing the equations to have zero gradients at the stagnation plane. At the intersection of the stagnation plane and the centerline, the velocity is set to zero in the direction parallel to the plane (**u**), and the velocity at the stagnation plane perpendicular to the plane is zero (**v**).

$V = 0$ At y = 0

$\frac{\partial(L)}{\partial(y)} = 0$ Stagnation plane boundary conditions

At the jet exit, the inlet of the domain, the boundary conditions are set to model the system desired, i.e. composition, temperature, and pressure, etc (Rogg and Wang, 1995). RUN-1DL uses a steady state Newton solver to resolve equations, but automatically implements time stepping when steady state convergence fails, until a steady state convergence is found. A detailed kinetic mechanism (shown in Appendix 3) was chosen to model the flame consisting of 50 reactions and 17 species.

4.4 PLIF measurements

The PLIF system allows one to take detailed measurements of flame structure in a relatively undisturbed state. The basic principle behind the operation of PLIF systems is that the energy of ro-vibrational excited states of molecules is quantized and therefore specific molecules will absorb and radiate photons at certain frequencies. Using a tunable dye laser, an appropriate excitation signal can be developed which will only excite the molecules being measured. This absorbed energy is then re-radiated in random directions in specific frequency bands and can be measured. The measured signal is related to the concentration of the molecule present. Thus, PLIF systems actually measure

concentration of a particular molecule, in this case the flame front marker, OH, or hydroxyl radical. The measured signal also depends on the pre-excitation states of the molecules, because only certain excitation levels will absorb the laser's frequency, so it is sometimes necessary to correct for the population fraction of the molecules in the various excited states using a standard thermodynamic distribution such as the Boltzman Distribution. The signal can also be absorbed by other molecules such as H_2O which require correction based on the amounts of those molecules present as well. However, by carefully choosing the frequency used to excite the OH molecules and the signal bands detected, these effects can be minimized and their corrections skipped. Barlow and Collignon (1991) have shown that when exciting a sample with the frequencies used for this work, the signal can be interpreted as the OH mole fraction to within 10% of the peak OH mole fraction.

When processing the data, there are still some corrections that must be made. First the dark field correction must be made which accounts for the magnification of thermal radiation in the CCD camera. This correction is obtained by taking images with the lens cap on when the detector is at a specific temperature. A second correction is the flatfield correction which accounts for the differing sensitivity of the pixels on the image chip in the camera. This correction is obtained by measuring a constant light source and comparing the values obtained for each pixel to the average value and obtaining a ratio which can be used to multiply the value measured to correct it. Another correction is to account for the variations in laser sheet intensity. This is necessary because the

signal strength will depend in part on how strongly the sample is excited. The sheet profile correction is a ratio of the measured laser sheet strength to the average strength. The sheet profile was measured in two ways in this experiment, first by reflecting a small amount of the incoming beam directly into the camera using a piece of glass angled to the beam, and second by viewing the fluorescence of a homogenous acetone jet. A correction for the laser's contribution to the background was also made by tuning the laser to a frequency without resonance and recording the image. Finally, the size of the image was corrected to account for magnification using the relationship for size developed from the target image pictures which contain a scale. All these steps were performed automatically by a MATLAB program (Mueller, 1997) to correct the PLIF images obtained from the system at SNL.

4.5 PIV measurements

The underlying principle behind PIV measurements is that the displacement of particles in the flow can be measured which provides a means to quantify the flow velocity. The light source, in this case a dual oscillator Nd:YAG laser (Quanta Ray PIV 400), strobes twice illuminating the particles at two different instants in time separated by a known interval. Operating simultaneously with the light source, a camera records the image of the light being scattered off the particles at both instants in time on separate frames. Figure 4.2 shows a PIV image which was obtained in a CH_4 flame. Light is scattered off the particles by Mie Scattering, which refers to a simple reflection of the light off an object at the same frequency as the incident light. Therefore, care

must be exercised when utilizing PIV to minimize unwanted reflections of the laser beams because the excitation frequency is the same as the signal frequency and cannot be filtered out. Comparing the two images from the camera, the displacement of the particles can be obtained and used to calculate the flow velocity. In order to convert the particle displacement to a physical distance, a photograph of a target with a grid is usually taken. In practice the velocity is found by taking the most probable displacement from several particle pairs in a small region of the image known as the interrogation region. The physical size of the interrogation region determines the spatial resolution of the system, and the time between camera images determines the temporal resolution of the system.

The large number of interrogation regions used for each image pair requires the use of computer programs to automatically process the data. These programs divide the images into interrogation regions and calculate the displacement of the particles for each region. There are several possible displacements whereby a particle could move from its starting location to any of the final locations. Therefore to determine which of these scenarios is the best, every possible displacement is compared. This is accomplished by moving all the particles by the same number of pixels and determining if there is correlation with the second image. Assuming that all the particles move with the same displacements, there will be a single displacement vector which accounts for the differences between the two images. However, if there are different displacements which might work, the algorithm will have to decide which displacement is the most probable. This is accomplished by calculating the 2-D

correlation value between the shifted first image and the second image. The largest correlation value is the most probable displacement. The MATLAB routine used to automate this procedure was developed by Han and Mungal (2000). In order to create smooth velocity fields, the interrogation regions are often overlapped which results in a greater number of velocity measurements, but not improved resolution.

4.6 Filtering of the average and RMS velocity values

The measured velocity data were filtered to remove outliers using a three standard deviation test for both the average and RMS velocity values reported. This test was successfully used by Griebel et al. (2003), and was emulated in the processing in this study. The three standard deviation test was performed iteratively three times such that outliers were removed from the mean and standard deviation calculated during each iteration as the acceptance criterion for the next iteration. Filtered and unfiltered average and RMS vertical velocity data is shown in Figure 4.3 for the CH_4 flame data. The outliers did not significantly affect the average, but there was a noticeable improvement in the RMS velocities. The RMS needed filtering because it was a higher order moment and depended on the square of the variance, so outliers significantly affected it. As expected, the noise in the RMS field was reduced while the average field remained relatively unchanged. The three sigma test used to filter the data preserved around 99% of the data and rejected the remainder, as predicted for a normal distribution of data. In this study, at least 200 image pairs were used for each experiment to ensure accurate RMS values. The computed RMS values were independent of the

number of images for image sets greater than 100, when the data were filtered as discussed above.

4.7 The calculation of the TKE

Turbulent kinetic energy is a measure of the kinetic energy contained in the fluctuations of the flow around the mean velocity value. Since these fluctuations are caused by the turbulent nature of the flow, the TKE is also a measure of the turbulence of the velocity field. In order to characterize the fluctuations around the mean, the RMS velocities are used to calculate the TKE. The formula used to calculate the TKE is given as Eqn. 4.12 below:

$$TKE = \frac{1}{2}\left(U_{RMS}^2 + V_{RMS}^2\right) \qquad \text{Eqn. 4.12}$$

where U_{RMS} and V_{RMS} are the horizontal and vertical RMS velocities respectively. The third RMS velocity component was not measured, and therefore has not been included in the calculation of the TKE. Neglecting the third RMS component will reduce the value of the TKE accordingly.

4.8 Vorticity calculation

Vorticity is an important flow property because it is a measure of the rotation of the flow. Therefore, vorticity is found where there is a turbulent eddy, or where the flow turns. The vorticity is defined as curl of the velocity vector, and is a vector quantity. The formula for the vorticity, ω, of a flow is given below in Eqn. 4.13:

$$\omega = \nabla \times \vec{V} = \left(\frac{\partial w}{\partial y} - \frac{\partial v}{\partial z}\right)\hat{i} + \left(\frac{\partial u}{\partial z} - \frac{\partial w}{\partial x}\right)\hat{j} + \left(\frac{\partial v}{\partial x} - \frac{\partial u}{\partial y}\right)\hat{k} \qquad \text{Eqn. 4.13}$$

where u, v, and w are, respectively, the horizontal, vertical, and out of plane velocity components, and x, y, and z are respectively the horizontal, vertical and out of plane coordinates of the flow field (Munson et al., 1994). The PIV measurements were used to obtain the 2-D planar vorticity, the z-component of vorticity, given as Eqn. 4.14:

$$\omega_z = \left(\frac{\partial v}{\partial x} - \frac{\partial u}{\partial y} \right) \hat{k} \qquad \text{Eqn. 4.14}$$

Note that the remaining two components of the vorticity could not be obtained from the monoscopic PIV data because the out of plane velocity was not measured. A positive value of vorticity corresponds to a counterclockwise turning of the flow, and a negative value corresponds to clockwise rotation. The magnitude of the vorticity value is a measure of how sharply the flow is turning.

A path integration method was utilized to differentiate the velocity field in Eqn. 4.14. This was necessary because the velocity vectors had a 50% overlap, which meant that neighboring data were 50% correlated. This correlation of adjacent data points leads to poor estimates of the velocity field derivatives when using more traditional differencing techniques. The path integral method utilized a square boundary defined by the eight surrounding data points. Figure 4.4 (a) shows a diagram of the eight points surrounding a point of interest. The dark line around the edge of the figure represents the path, the lighter lines denote the interrogation regions, and the quantities in parentheses are the MATLAB array designations. The circulation was calculated around the path, and was multiplied by two to obtain the vorticity. The path integration method and derivatives performed using several differencing techniques have been used to calculate the

vorticity of the same velocity field by Raffel et al. (1984). The path integration method showed a significant advantage in the ability to reproduce theoretical vorticity fields in velocity fields with overlapping data.

4.9 Normal strain calculation

The normal strain, ε, is a scalar value which is a measure of the expansion and contraction of fluid elements, also known as volumetric dilatation. In a compressible flow, normal strain can occur when there is a change in pressure, or when there is a change in temperature. In the present study, the pressure gradients are small; however there were significant temperature gradients due to the heat release of the flame. The normal strain is defined as the dot product of the gradient and the velocity vector, as given by Eqn. 4.15 below (Munson et al., 1994):

$$\varepsilon = \nabla \bullet \vec{V} = \frac{\partial u}{\partial x} + \frac{\partial v}{\partial y} + \frac{\partial w}{\partial z} \qquad \text{Eqn. 4.15}$$

The normal strain can also be calculated using a path integration method to improve accuracy in over-sampled data. The analogy used in this instance is to find the flow normal to the boundaries of the square path defined by the surrounding eight points (Raffel et al., 1984). Figure 4.4 (b) shows the path around the eight surrounding points, and the arrows show the flow normal to the boundary. The third term of Eqn. 4.15 was not calculated because the out of plane velocity and velocity gradients were not measured. Thus, the normal strain presented in this study is a 2-D normal strain. Flow normal to the plane can affect the value of the normal strain, which must be considered when analyzing 2-D results.

4.10 Calculation of the kinetic energy dissipation rate

Kinetic energy dissipation rate (Ked) is a measure of the conversion of the kinetic energy of the flow to internal energy of the fluid by viscous losses at small scales. The kinetic energy dissipation rate is given by Eqn. 4.16 below:

$$Ked = 2 * \upsilon \overline{\left[\left(\frac{\partial u'}{\partial x} \right)^2 + \left(\frac{\partial v'}{\partial y} \right)^2 + \left(\frac{\partial w'}{\partial z} \right)^2 + \frac{1}{2}\left(\frac{\partial u'}{\partial y} + \frac{\partial v'}{\partial x} \right)^2 + \frac{1}{2}\left(\frac{\partial u'}{\partial z} + \frac{\partial w'}{\partial x} \right)^2 + \frac{1}{2}\left(\frac{\partial v'}{\partial z} + \frac{\partial w'}{\partial y} \right)^2 \right]}$$

Eqn. 4.16

where ν is the kinematic viscosity of the fluid, assumed as air at atmospheric conditions (Tsurikov and Clemens, 2002), and the bar represents a time-average. The nine differential terms in Eqn. 4.16 arise from the strain rate tensor. However, all of these terms can not be calculated from the 2-D velocity data. Therefore, a 2-D kinetic energy dissipation rate was defined as follows in Eqn. 4.17:

$$Ked_{2D} = 2 * \nu \overline{\left[\left(\frac{\partial u'}{\partial x} \right)^2 + \left(\frac{\partial v'}{\partial y} \right)^2 + \frac{1}{2}\left(\frac{\partial u'}{\partial y} + \frac{\partial v'}{\partial x} \right)^2 \right]} \qquad \text{Eqn. 4.17}$$

where the terms that cannot be calculated have been removed following the work of Tsurikov and Clemens (2002). The differential terms were calculated by modifying the path integration formulas used for the normal and shearing strain rates defined in Raffel et al. (1984).

4.11 Integral length scale calculations

The integral length scale is a measure of the size of flow structures, or the length over which the data remains correlated. The size of the flow structures is important in determining both the properties of the flow field and the interaction of the flow field and the flame. The vertical integral length scale was calculated

at several locations near the reaction zone. First, the autocorrelation coefficients at several points downstream of a location were obtained using Eqn 4.18 below:

$$R_i = \frac{\overline{(v_0 - v_{0avg})(v_i - v_{iavg})}}{\overline{(v_0 - v_{0avg})(v_0 - v_{0avg})}} \qquad \text{Eqn. 4.18}$$

where the subscript "i" refers to points at downstream locations, the subscript "0" refers to the location, the subscript "avg" refers to the time-average value, and the bars over the denominator and the numerator refer to a time-average. The value of the autocorrelation coefficient is unity at i = 0 and it decreases to zero downstream. The calculations were truncated at i = 15, where the correlational coefficient was nearly zero. Accordingly, the integral length scale was defined as the integral of the correlation coefficient function for i = 0 to 15. The correlational coefficients were numerically integrated using the trapezoid rule.

4.12 Borghi turbulent combustion diagram

The operating conditions have been plotted onto a classical turbulent combustion diagram in Figure 4.5 to classify the flame types. The operating condition correspond to the two flame cases studied in chapters 6 and 7. According to the placement of the flames on the classical combustion diagram, they should be well stirred reactors. The data presented in later chapters do not support this hypothesis. The conditions have also been plotted onto a modified turbulent combustion diagram for classification as shown in Figure 4.6, following the work of Peters (1999). The CH_4 flame is near the border between the wrinkled and thickened-wrinkled regimes, and the H_2-enriched flame is in the thickened-wrinkled regime. These classifications seem more consistent with

flame structures observed in Chapters 5 and 7. The horizontal coordinate is the ratio of the integral length scale and the flame thickness. The modified turbulent combustion diagram is divided into several region based on values of the Turbulent Reynolds Number (RE_t), the Damkohler Number (Da), and the Karlovitz Number (Ka). The flame thickness was determined from the average of measurements of flame structures in single shot OH PLIF images. The flame thickness was 1.9 and 2.6 mm, respectively, for the H_2-enriched and CH_4 flames. The integral length scale was calculated to be about 1.5 mm for both flames, indicating that estimates based on geometry are not applicable near the combustor inlet. The vertical coordinate is the ratio of the RMS velocity to the laminar burning velocity. A typical RMS velocity of 8 m/s and laminar burning velocities of 0.4 and 0.96 m/s, respectively, were used for the CH_4 and the H_2-enriched flames. The laminar flame speed was assumed to be a volume weighted linear combination of the flame speeds of CH_4 and H_2 in air at atmospheric conditions.

4.13 Uncertainty analysis

Uncertainty values for the velocity field were calculated following the work of Haste (2000). The random portion of the uncertainty is caused by two factors. The first factor is lost particle pairs when a particle shows up on one image but not the other, possibly due to placement near an edge of the interrogation region. The second factor is velocity gradients within the interrogation region which cause different particle pairs to have different displacements making it difficult for the algorithm to decide which velocity is the correct one. The random error was calculated using Eqn. 4.19 below:

$$\sigma_E = \frac{1}{|V_0|\sqrt{12N}}\sqrt{L^2\left[\left(\frac{\partial u}{\partial x}\right)^2+\left(\frac{\partial u}{\partial y}\right)^2+\left(\frac{\partial v}{\partial x}\right)^2+\left(\frac{\partial v}{\partial y}\right)^2\right]+W^2\left[\left(\frac{\partial u}{\partial z}\right)^2+\left(\frac{\partial v}{\partial z}\right)^2\right]}$$

Eqn. 4.19

where V_0 is the velocity at the center of the interrogation region, N is the number of particle pairs per interrogation region, assumed to be 10, L is the width and height of the interrogation region, and W is the thickness of the laser sheet. All differentials are taken at the point in the center of the interrogation region. The random error is due to lost particle pairs and velocity gradients within the interrogation region. The differentials with respect to the out of plane velocity were estimated. The out of plane differentials accounted for a small amount of the overall random uncertainty, therefore estimating them seems reasonable. There is also a bias towards slower velocities in PIV, because faster moving particles are more likely to leave the interrogation region. The formula to correct for this bias is given by Eqn 4.20 below (Haste, 2000):

$$\langle E\rangle = -\frac{\Delta t}{|V_0|}\left[\left(u_0\frac{\partial u}{\partial x}+v_0\frac{\partial u}{\partial y}\right)\hat{i}+\left(u_0\frac{\partial v}{\partial x}+v_0\frac{\partial v}{\partial y}\right)\hat{j}\right]$$

Eqn. 4.20

where Δt is the time between laser pulses, u_0 and v_0 are the velocity components in the interrogation region, and $|V_0|$ is the magnitude of the velocity in the interrogation region. Haste's work included two additional terms in Eqn. 4.20 which were the product of the out of plane velocity and the corresponding differentials. These terms have been omitted here because they are the product of two unknowns, and are sign dependent. The uncertainty formulas were applied to every point in the velocity field for up to 30 images (100,000 points), and placed in order to determine the 95% confidence level. The uncertainty values calculated

from 30 images show convergence with those calculated for 15 images. The uncertainty in the velocity measurements is 0.31 m/s, corresponding to 3.1% of the average vertical velocity at the combustor inlet. The uncertainty for the vorticity and normal strain was calculated using the equation given by Raffel et al. (1984) in Eqn. 4.21 below:

$$\omega_\omega = 0.61 * \left(\frac{\omega_v}{0.5 * \Delta X} \right) \qquad \text{Eqn. 4.21}$$

where, ω_ω is the uncertainty in the vorticity or normal strain, ω_v is the uncertainty in velocity, and ΔX is the distance between vectors. The uncertainty in the vorticity and normal strain was found to be 400 s^{-1}.

4.14 Analysis of combustion noise measurements

When analyzing a time varying signal, such as sound, it is often desirable to modify the signal so that it is easier to observe trends in the data. Converting the signal from the time domain to the frequency domain using a Fourier transform is a common method for analyzing time varying signals. The Fourier transform is given in Eqn. 4.22 below (Wheeler and Ganji, 1996):

$$F(\omega) = \int_{-\infty}^{\infty} f(t) e^{-j\omega t} dt \qquad \text{Eqn. 4.22}$$

where $F(\omega)$ is the transform of the original signal f(t), j is the square root of negative 1, and ω is the angular frequency. When data is converted to the frequency domain, the dominant frequencies that make up the signal can be readily seen. However, converting a signal to the frequency domain means that all information contained in the time history is lost. For example, if a loud tone sounded at the beginning or the end of the sample window, the Fourier transforms

would be identical. Because the data is sampled in a discrete manner, the above formulation for the Fourier transform is inconvenient, and a Discrete Fourier transform (DFT) is used instead. The equation for a DFT is given in Eqn. 4.23 :

$$F(k\Delta f) = \sum_{n=0}^{N-1} f(n\Delta t) e^{-j(2\pi k\Delta f)(n\Delta t)} \qquad \text{Eqn. 4.23}$$
$$k = 0,1,2..., N-1$$

where Δt is the sampling interval, and N is the number of samples collected (Wheeler and Ganji, 1996). When using a DFT, the resolution is equal to the ratio of the sampling frequency and the number of samples analyzed. The sampling frequency also determines the maximum frequency which can be accurately measured. The Nyquist Criterion states that the maximum frequency that can be measured is half the sampling frequency. Any frequencies higher than the Nyquist limit will be aliased and show up as different frequencies. When dealing with frequency information, it is also desirable to know the sound power contained at a given frequency. The power spectral density (PSD) is a measure of the power contained in a finite frequency band. The PSD is mathematically defined as the square of the absolute value of the DFT, and is given in Eqn. 4.24:

$$PSD = |F(k\Delta f)|^2 \qquad \text{Eqn. 4.24}$$

where the symbols used are the same as those in Eqn. 4.23 (Wheeler and Ganji, 1996). The physical significance of this is that if the PSD data showed a peak at 500 Hz, it would mean that the sound being sampled had a strong signal at 500 Hz in addition to other weaker signal which may be contained in the original sound. The sampling frequency utilized for this experiment was 2000 Hz, which means that the signals up to than 1000 Hz can be accurately measured. The number of

samples collected was 2048, which means that the resolution of the sound measurements is less than 1 Hz. The PSD plot can be converted to units of Watt/Hz if a signal of known power is available. Integrating the PSD data with respect to frequency results in the total power contained in the region over which the data are integrated.

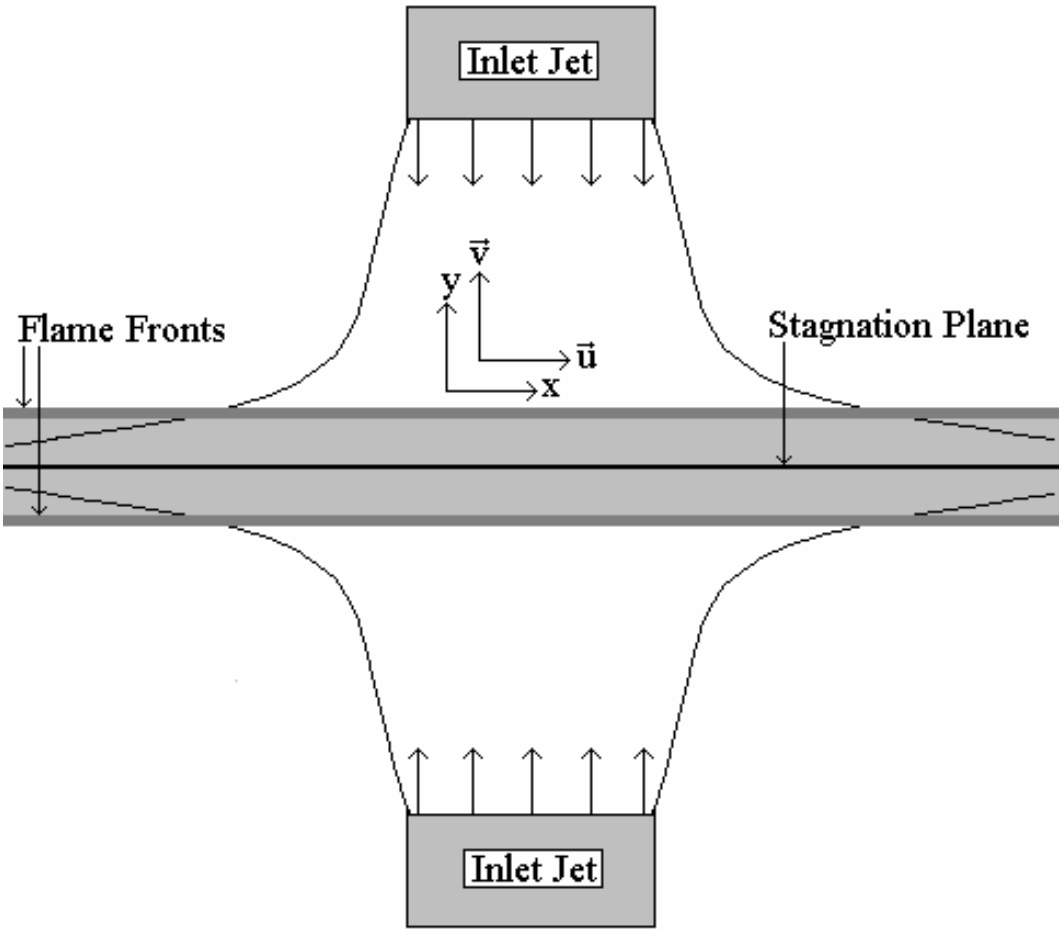

Figure 4.1. Cross section of a planar lean premixed counter flow flame. In the mathematical model, the jets pictured above would extend infinitely normal to the plane of the page.

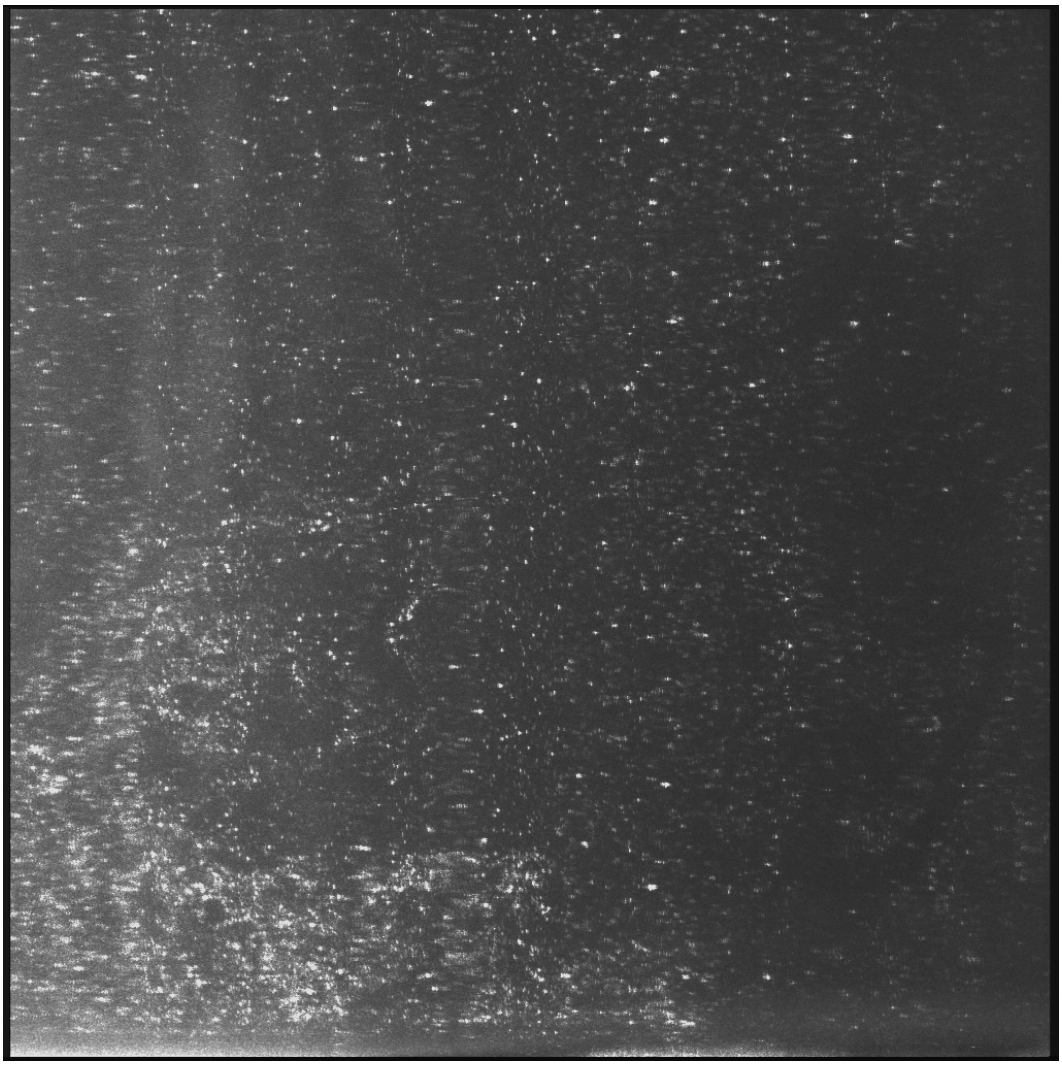

Figure 4.2. A PIV image of the CH_4 flame.

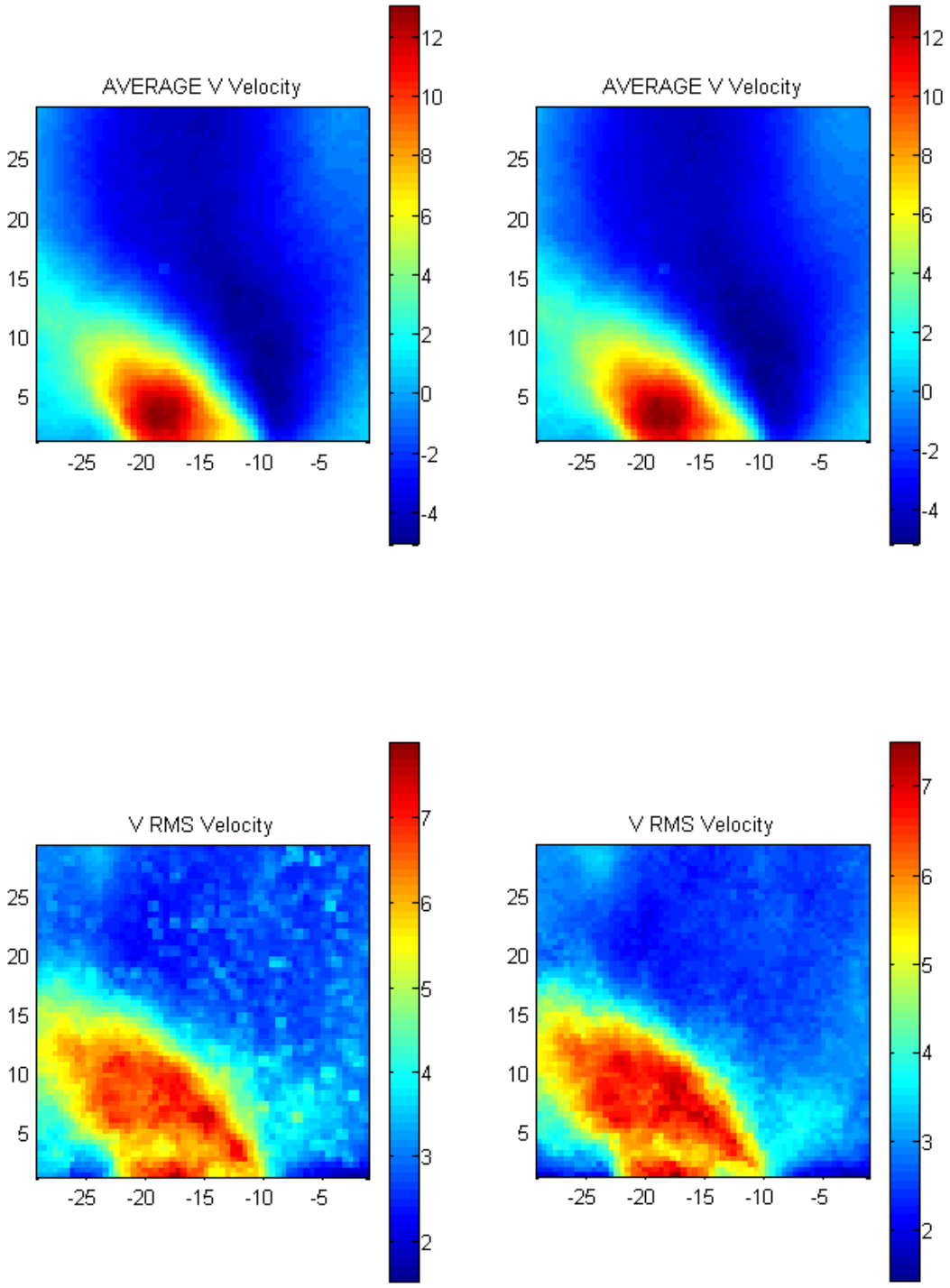

Figure 4.3. Average and RMS vertical velocities of a CH_4 flame, unfiltered, left column, filtered with iterative three standard deviation test, right column.

a.)

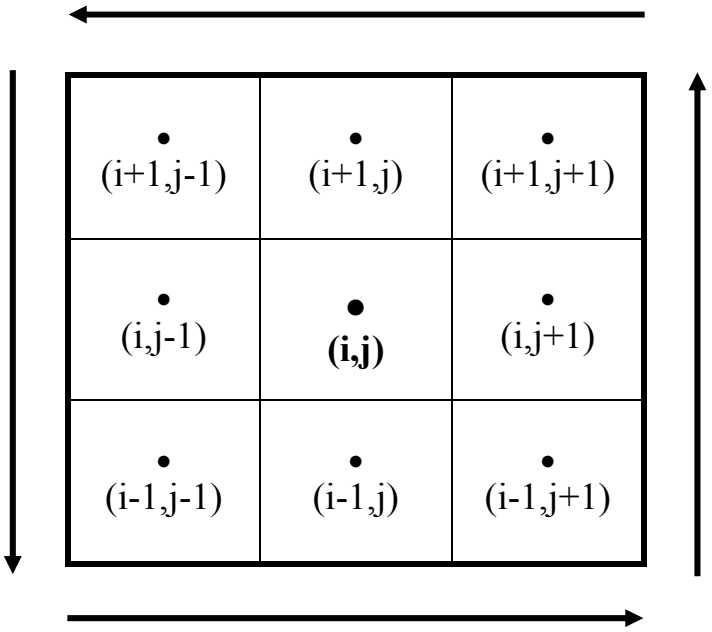

b.)

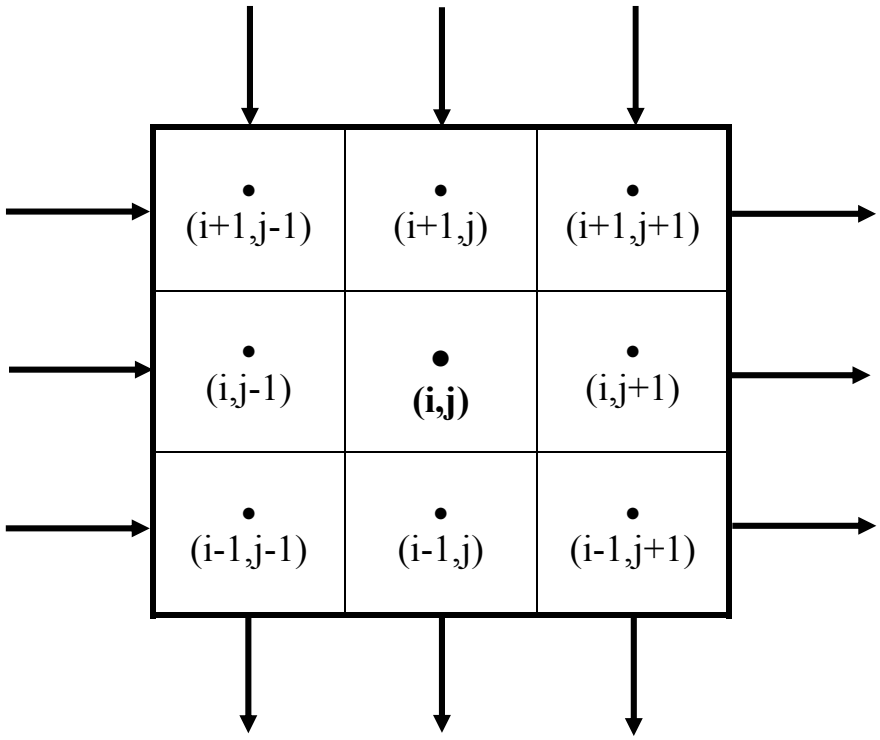

Figure 4.4. Schematic representation of the path integral method for vorticity a.), and normal strain b.). The interrogation regions, the boundary, and the MATLAB array designations for each point are shown.

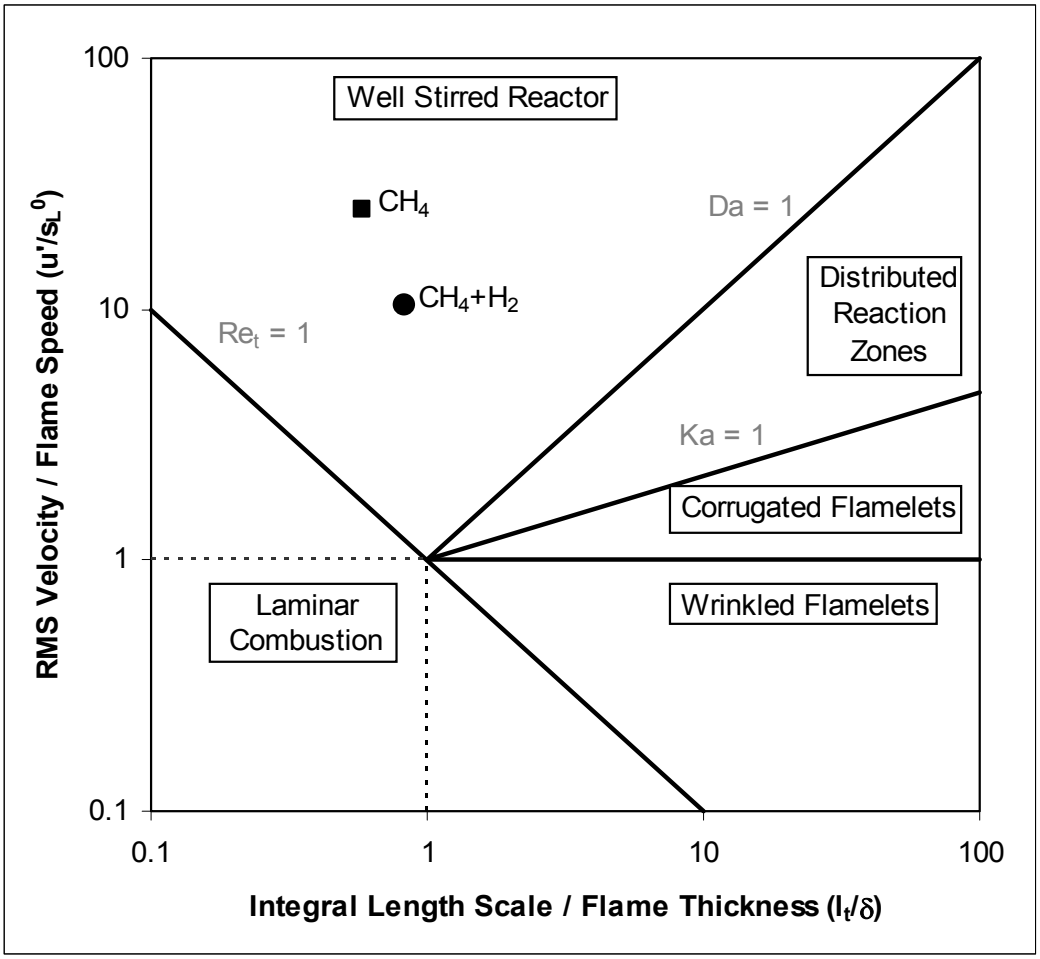

Figure 4.5. A classical turbulent combustion diagram (Borghi Diagram) showing the classification of a CH_4 and the 40% H_2-enriched CH_4 flame (Peters, 1999).

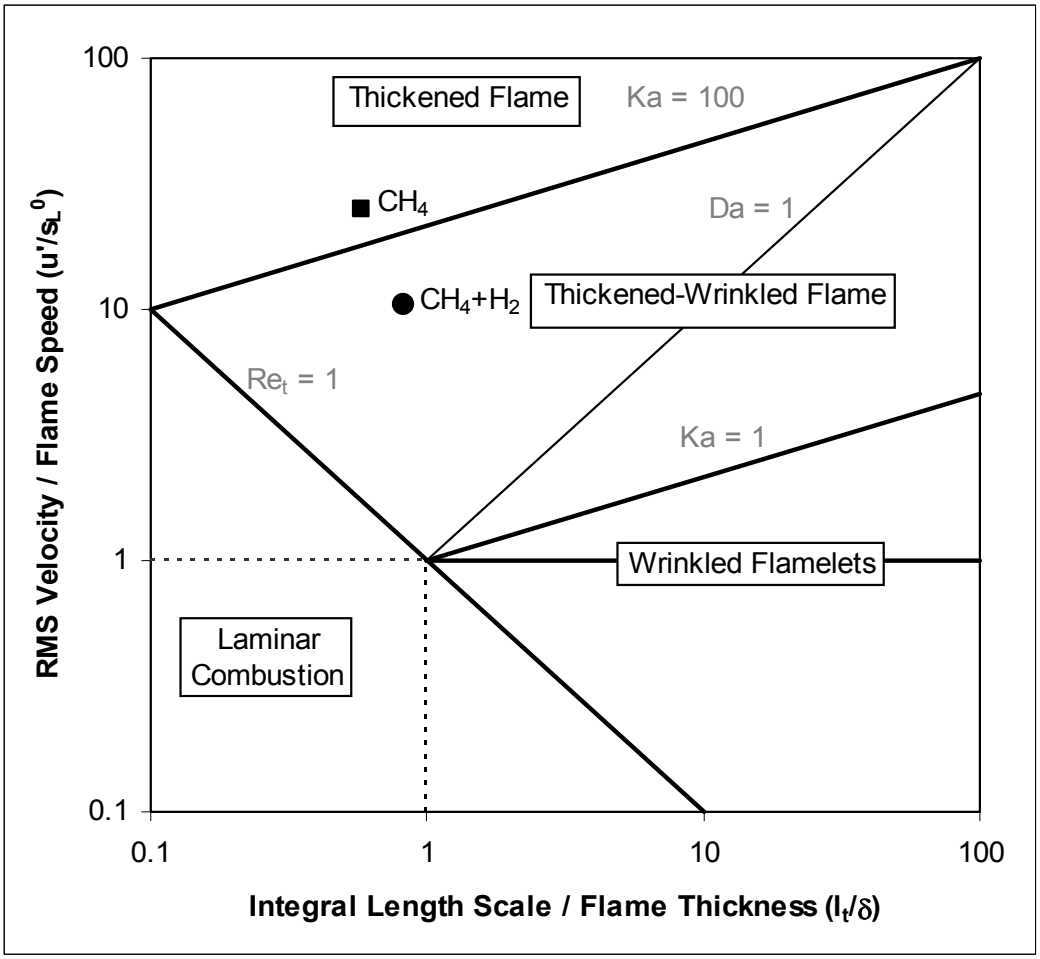

Figure 4.6. Modified turbulent combustion diagram (Borghi Diagram) showing the classification of the CH_4 flame and the 40% H_2-enriched CH_4 flame (Peters, 1999).

CHAPTER 5: GLOBAL FLAME CHARACTERISTICS

The results and discussion portion of this research will be divided into four chapters in a chronological manner. This chapter will present information on the global effects of adding H_2, O_2, N_2, CO_2, and liquefied petroleum gas (LPG) to CH_4 in the initial burner setup which has a swirl number of 0.78. The flame stability and extinction characteristics will be presented for all the fuels tested. Hydrogen is an important component of alternative fuels, so in addition to the extinction data, pollutant emissions data, flame photographs, and OH PLIF images will give information on the flame structure. Chapter 6 will detail the affect of H_2-enrichment on the flow field and its properties utilizing PIV measurements. Chapter 7 will present simultaneous PIV and OH PLIF data to show the interaction of the flame and the flow field, and how it is affected by fuel composition. Chapter 8 will present global flame properties including emissions, combustion noise, and flame length in the modified burner.

5.1 Flame stability

Flame stability characteristics were obtained by maintaining a constant volumetric flow rate of the fuel-air mixture (Q) through the combustor and incrementally decreasing the fuel flow rate, and hence the equilibrium adiabatic flame temperature (T_{ad}), until instability and blow off occurred, as per the steps outlined in section 3.2. Flow rate was used as a variable because it is directly related to the inlet velocity, and hence the strain rates in the combustor. The experiments were repeated several times at each flow rate for each fuel to ensure repeatability of the results. The flame instability refers to a weakening of the

flame anchoring, which produced a tornado shaped flame in the center of the combustor. In this study, the lean blow out limits of different binary gaseous fuels mixtures (NG and an additive) are compared for a given equilibrium adiabatic flame temperature. Note that the actual flame temperature will be lower than the equilibrium temperature because of the drop in the combustion efficiency as LBO is approached. Figure 5.1 shows the lean stability maps for H_2 mole fraction X_{H2} = 0.0, 0.12, 0.22, and 0.29. The upper data points refer to the flame instability and the lower data points represent the flame blow out. The results show that flames at higher fuel-air flow rates stabilized at higher adiabatic temperatures. This effect is attributed to the higher strain rate in the flame at larger fuel-air flow rates. At Q = 500 slm the CH_4 flame blows out at T_{ad} = 1175 ^{0}C. The corresponding value for X_{H2} = 0.12, 0.22, and 0.29 flames is, respectively, 1090 ^{0}C, 1080 ^{0}C, and 1070 ^{0}C. The results demonstrate that the addition of H_2 to CH_4/NG extends the lean stability and blow out limits in the present combustor configuration.

The LBO characteristic of NG blended with, respectively, 19%, 28%, and 38% LPG by mole basis are shown in Figure 5.2. The flame temperatures at LBO and instability show the typical increase with increasing fuel-air flow rate. However, the increases in temperatures with fuel-air flow rate are higher as compared to those for NG, suggesting that the addition of LPG to NG increased sensitivity of the flame to the local flow strain. Figure 5.2 reveals that the instability region narrowed at higher fuel-air flow-rates, prompting an unstable flame to readily blow out.

Figure 5.3 shows a small effect of O_2-enrichment on LBO characteristics of NG flames. The amount of O_2 may not make a significant difference in the combustion, since the fuel and air are thoroughly premixed, and the amount added to the fuel is small compared to that in the combustion air. The observed trends in Figure 5.4 for NG blended with N_2 are similar to those in Figure 5.1 (a) for NG. This result is expected because the N_2 added to the fuel constitutes only a small fraction of the total N_2 in the fuel-air mixture, a maximum of about 4 percent by mole basis. The flame stability data for NG blended with CO_2 are shown in Figure 5.5. In this case, an opposite trend is observed, i.e., the flame stability improved as the total air-fuel flow-rate was increased. This effect may be attributed to the flow mixing processes in the combustor affecting the flame stability. At high flow rates, the centrifugal action of the swirler might accumulate the heavier CO_2 molecules in the outer periphery of the combustor to produce a richer, and hence, more stable mixture in the central region. Detailed species measurements throughout the combustor are therefore needed to fully explain the observed trends.

An important design parameter for LPM combustion systems is the flame temperature at LBO. Therefore, the next two figures show how the adiabatic flame temperature at LBO varied with fuel composition for the five additive gases studied. Figure 5.6 presents results for the reactive species, i.e., LPG, H_2, and O_2. The data for non-reacting species, i.e., CO_2 and N_2 are shown in Figure 5.7. For each fuel composition, the measurements are shown for three different fuel-air

flow-rates, i.e., 0.5, 0.75, and 1.0 m^3/min. In Figures 8 and 9, the data points corresponding to zero percent additives relate to the base case of NG fuel.

Figure 5.6 shows that the addition of H_2 to NG drastically lowers the flame temperature at which LBO occurs. Adding 40% H_2 to NG lowered the LBO temperature by nearly 400 C. In this study, the decrease in LBO temperature was linearly proportional to the amount of H_2 in the fuel mixture. The increased stability range may be used to develop ultra-LPM combustion systems producing lower NOx emissions by sustaining combustion at lower flame temperatures without the typical increases in CO and UHC emissions. Similar benefits of H_2 were reported in previous studies using C_3H_8 (Anderson, 1975). Studies in stagnation and opposing jet flow configurations (Gauducheau et al., 1998), (Ren et al., 1999) have shown that the H_2 is resistant to flame extinction because of its high mass-diffusivity and reactivity. The effects of H_2's reactivity and its mass-diffusivity cannot be experimentally separated, so the benefits of H_2 are due in part to its diffusivity and in part to its reactivity. The burning rate was particularly sensitive to H-radicals attacking the O_2 molecule in the main branching reaction (Ren et al., 1999). Apparently, adding H_2 to NG affects the H-radical concentration and hence, is partly responsible for the resistance to the local flow-strain.

Figure 5.6 shows that adding LPG to NG increases the flame temperature at LBO. It was expected that LPG would improve the LBO limit because C_3H_8, the main constituent of LPG, has a slightly higher laminar flame speed than CH_4, the primary constituent of NG. A previous study (Kee et al., 1989) has also

shown that adding C_3H_8 to NG lowers the LBO limit at higher inlet temperatures, presumably because of the chemical kinetic effects. This study however found that these effects are not pronounced in LPG/NG flames at ambient inlet temperature and pressure. Therefore, these contrary results are probably a combination of slow kinetics at the inlet conditions, and reduced mass diffusion due to higher molecular weight.

The addition of O_2 to NG did affect a slight decrease in the flame temperature at LBO as shown in Figure 5.6. However, the effect was not significant over the range measured because maximum O_2 added to the fuel was less than 15 percent of total O_2 present in the fuel-air mixture. Conversely, this amounts to burning NG in an oxidizer containing 24% O_2 and 76% N_2. Improved flame stability in O_2-rich air was also observed in stagnation flow configuration investigated by Wu et al. (1999). Improved flame stability was attributed to an increase in the laminar flame speed because the added O_2 enhanced the main branching reaction involving O_2 and the H-radical. Figure 5.7 shows that the addition of non-reactive species to the NG did not affect the flame temperatures at instability and LBO in a definite manner. Evidently, the added CO_2 and N_2 are inert and thereby, they do not have a noticeable effect on chemical processes of the flame near the LBO limit.

The ability of H_2 to improve lean stability in a CH_4 flame was further explored using 1-D strained premixed flame calculations in RUN1-DL. The computed results in Figure 5.8 show that the strain rate at extinction increases as the flame temperature is raised, and as the amount of H_2 in the fuel is increased.

At an equilibrium adiabatic flame temperature of 1400C, the computed extinction strain rate is 645, 1100, and 2000 s^{-1}, respectively, for flames of CH_4, CH_4 with 20% H_2, and CH_4 with 40% H_2. The computational results support the experimental finding that the fuels containing H_2 withstand higher strain before extinction. Extinction due to strain is caused because the residence time of the reactants in the combustion zone decreases with increasing strain until there is not enough time for the combustion to occur before the reactants leave the combustion zone. The comparison between experiments and computations is, however, not direct. In experiments, the premixed flame stabilizes by orienting itself to the local flow velocity and strain fields that are subject to the turbulent fluctuations. Hence, the computations simulate the local phenomena rather than the global characteristics of the flame. These computations are included here as they provide explanation of the global characteristics observed. The measured average strain rates presented later are similar in magnitude to those calculated in the 1-D simulations, however the numerical simulations were performed to show trends rather than absolute values for the strain resistance.

5.2 Pollutant emissions

To gain an understanding of CO and NOx emissions produced in the flame, probe measurements were taken in the combustor using NG for $X_{H2} = 0.0$ and 0.45. The combustor was operated near the lean stability limit of NG at Q = 450 slm and T_{ad} = 1240 C for both fuels. Figure 5.9 shows horizontal profiles of CO and NOx concentrations at two vertical planes (y) measured from the swirler exit to depict the major trends. The results reveal significantly lower CO

concentrations at both vertical planes when H_2 was added to the NG. The H_2-enriched fuel produced CO values below 10 ppm at y = 20.3 cm, where the combustion process was nearly complete. The corresponding CO values for NG ranged from 15 to 100 ppm in the central region and several hundreds ppm in the wall boundary region. The NOx concentration shown in Figures 5.9 (c) - (d) was always below 10 ppm because of the modest adiabatic flame temperature of the experiment. The NOx formed close to the combustor inlet and reached nearly steady conditions within y = 5.1 cm, evidently because of the rapid combustion with H_2 present in the fuel. The NG flame required a longer residence time, and hence, a longer distance to reach steady NOx concentrations at y = 20.3 cm. Figure 5.9 (d) shows similar NOx concentration profiles for both fuels at y = 20.3 cm. This result suggests that the NOx production was not affected by H_2 addition and that it was determined mainly by the adiabatic flame temperature. These results demonstrate that a significant reduction in CO emissions is realized by H_2 addition without adversely affecting the NOx emissions.

5.3 Adiabatic flame temperature and flow rate effects

Before examining the effects of H_2-enrichment on a flame, the parameters of adiabatic flame temperature and inlet velocity will be investigated. These parameters will be studied for CH_4 flame, to serve as a baseline, and give context for the remaining results. The effect of adiabatic flame temperature will be explored by examining photographs, instantaneous and average OH PLIF images, and profiles of the average OH signal. Results of the opposed flow modeling will show the effect of temperature on the important OH and H radicals.

Figure 5.10 shows four photographs of the flame luminosity at different adiabatic flame temperatures for a CH_4 flame. The exposure time for these images was relatively long, so they represent an average image. Typically, at the highest equivalence ratio of $\phi = 0.60$, Tad = 1385 C (Figure 5.10 (a)) the flame is short and blue and fills the entire quartz confinement tube in the upstream region. The flow in a swirl-stabilized combustor consists of two flow recirculation zones; one is located downstream of the centerbody and another, torroidal region referred to as the corner recirculation zone**,** is located at the intersection of the vertical combustor wall and the horizontal inlet plate. Note the combustion occurring in the corner recirculation zone as clearly indicated by the flame luminosity. At this equivalence ratio the flame luminosity originating from the corner recirculation zone is continuous, indicating a steady combustion process. Decreasing the equivalence ratio, visible emission from the corner zone becomes increasingly intermittent until, at $\phi = 0.56$, Tad = 1311 C (Figure 5.10 (b)) there is no visible flame in the corner recirculation zone. The diameter of the flame decreases as the flame moves away from the confinement tube wall and the length of the flame increases as the equivalence ratio is decreased. For $\phi = 0.54$, Tad = 1274 C (Figure 5.10 (c)), the flame extends past the downstream end of the quartz tube. Finally, further reductions in ϕ (Tad) cause the flame to become unstable, oscillating between a larger-diameter flame that extends across much of the confinement tube (similar to flame c) to a much narrower flame that can best be described as a narrow cylinder extending along the center of the enclosure. Figure 5.10 (d) show a flame typical of this condition at $\phi = 0.52$, Tad = 1237 C.

The flame remains in this unstable mode until, becoming paler blue, and eventually extinguishing. This corresponds to the flame LBO condition. OH PLIF data will provide greater understanding of the effects of flame temperature on the flame structure.

Although the OH persists in the post flame region, the OH levels in the primary reaction front are typically a factor of two or more higher than those in the post flame gases (Cattolica, 1982). Thus, the signal intensity in PLIF images provides a direct measure of OH concentrations to identify the flame reaction zones. The single-shot OH PLIF images corresponding to the four flames pictured in Figure 5.10 are shown in Figure 5.11. For all equivalence ratios the outer edge of the high OH region is very irregular and probably reflects variations in the local velocity field, which contort the flame surface. The OH is uniform throughout much of the flame, with locally high concentration regions forming thin filaments that typically extend along the irregular interface located between unburned reactants and combustion products. Measurements in premixed flat flames (Cattolica, 1982) show that the highest OH concentrations occur in the primary flame zone and then decay downstream as the OH approaches equilibrium levels. These super-equilibrium values, which can exist at up to five times the equilibrium value, are due to the imbalance that exists between faster chain-branching reactions that produce OH and the slower radical recombination reactions that consume it. Using high OH as an indicator of high temperature, the high temperature region is seen as continuous over a large area downstream of the upstream flame front.

The above results emphasize the instantaneous OH distributions. Also of interest are the time-averaged OH distributions. To obtain these, 600 instantaneous OH PLIF images were averaged at selected flow conditions. Figure 5.12 (a) shows the time-averaged distribution for v = 14 m/s, $\phi = 0.60$, Tad = 1385 C for a CH_4 flame. Nearest the inlet, the maximum OH exists in the shear layer located between the centerbody recirculation zone and the corner recirculation zone. The peak OH occurs at about two centerbody diameters downstream of the inlet and away from the centerline near the quartz confinement tube. The region downstream of the centerbody contains a relatively low concentration of nearly uniform OH indicating a lack of reactions in that region. Significant OH can also be seen extending upstream into the corner recirculation zone along a layer adjacent to the quartz tube.

Figure 5.12 (b) shows the time-averaged OH distribution for the same velocity but at a lower equivalence ratio, $\phi = 0.54$, Tad = 1274 C. The peak OH concentrations exist in approximately the same region as with the higher equivalence ratio. Notable, however, is the lack of any OH in the corner recirculation zone. The maximum OH levels have also decreased significantly when compared to the higher equivalence ratio. Finally, in Figure 5.12 (c) for $\phi = 0.52$, Tad = 1237 C, the maximum OH occurs near the flow centerline in the region downstream of the centerbody. This corresponds with flame luminosity data showing a thin tornado shaped flame in the center of the combustor. Again the peak OH levels show a significant decrease at lower equivalence ratio.

Figure 5.13 shows time-averaged horizontal profiles of the OH concentration obtained from the images in Figure 5.12 for equivalence ratios of 0.60, 0.54 and 0.52, Tad = 1385 C, 1274 C, and 1237 C, respectively. These profiles correspond to an vertical location approximately two centerbody diameters downstream where the peak OH occurs in the $\phi = 0.6$ flame. The profiles verify that there is a significant variation in the peak OH with equivalence ratio or adiabatic flame temperature. Note that the flames corresponding to the three flow conditions seen in Figures 5.12 and 5.13 show considerably different global features that make direct comparisons of the OH levels difficult. For example, the flame at $\phi = 0.6$ exists very close to the quartz confinement tube where wall interactions with the flame could influence OH concentration. In addition, significant combustion is present in the corner recirculation zone. This observation contrasts with the $\phi = 0.54$ and 0.52 flames where no corner recirculation zone flame exists and the flame has moved away from the confinement wall.

Results of the opposed flow calculations lend insight into the observed trends in the data. In Figure 5.14, an increase in calculated OH radical concentration with increasing equilibrium temperature is shown. These profiles correspond to a CH_4 flame at a strain rate of $645 s^{-1}$. The increase of OH radical concentration with flame temperature is not proportional. At higher temperatures near stoichiometric conditions there does not appear to be any noticeable increase in OH radical concentrations. However, at lower flame temperatures pertaining to

the LBO limit the increase is OH is marked, in agreement with the experimental results.

Variations in the H radical mole fraction with equilibrium flame temperature are shown for a CH_4 flame at a strain rate of $645s^{-1}$ in Figure 5.15. As the equilibrium flame temperature increases, the concentration of H atoms increases noticeably. Furthermore, the peak location is shifted away from the stagnation plane at higher flame temperatures, as the flame is stabilized farther from the stagnation plane. The increasing concentrations of radicals and the stabilization of the flame closer to the nozzle at higher adiabatic flame temperatures agree with global characteristics of improved stability and a shorter flame.

Several OH PLIF images near the LBO limit are shown in Figure 5.16 to visualize the effects of flow velocity on the flame. Figures 5.16 (a) and (b) show two images taken on different laser shots of a CH_4 flame at an equivalence ratio of 0.52, Tad = 1237 C and an inlet velocity of 10 m/s. Comparison of the two images shows the time-varying nature of the flame. The images in Figures 5.16 (c) and (d) are for the same equivalence ratio but at an inlet velocity of 17 m/s, which is just below the blowout velocity of 18 m/s for this equivalence ratio. Comparison of the images at 10 m/s and 17 m/s shows a significant decrease in the size of the high OH region at the higher velocity, and a more shredded, or intermittent, appearance to the flame.

5.4 Hydrogen-enrichment effects on global flame characteristics

Global characteristics of H_2-enriched flames will be presented next for comparison with the previous results. Direct luminous photographs of the flame were obtained to gain an understanding of the flame location and size. The results are shown in Figure 5.17 for CH_4 with X_{H2} = 0.0, 0.12, 0.22, and 0.29. The total air-fuel mixture flow rate of 700 slm and equilibrium adiabatic flame temperature of 1290 +/ -20 C correspond to conditions near the lean stability limit of CH_4. Figure 5.4 (a) shows no visible flame in the corner recirculation zone for X_{H2} = 0.0. The flame extended past the downstream end of the combustor tube. Hydrogen addition (X_{H2} = 0.12) produced a continuous stable flame in the corner recirculation zone and a significantly shorter flame, indicating a more rapid combustion. The flame size and shape were qualitatively similar to those obtained with a CH_4 flame (X_{H2} = 0.0) operating at a higher equilibrium adiabatic flame temperature of 1385 C (not shown). A further increase in H_2 mole fraction decreased the flame length although the change was modest. The results show that flames with reactions in the corner recirculation region tend to be shorter and more stable, although perhaps only stable flames can support combustion in the corner recirculation. Because luminous photographs provide only a qualitative description, the OH measurements using PLIF are discussed next to develop a quantitative understanding of the flame structure.

The instantaneous flame structure is represented first by the single-shot OH PLIF images shown in Figure 5.18, corresponding to the photographs in Figure 5.17. The effect of H_2 on the flame is observed for v = 14 m/s and

$\phi = 0.54$ Tad $\approx$ 1290C. As the percentage of H_2 is increased the visible flame becomes significantly shorter indicating more rapid combustion. At these conditions without H_2 there is no visible flame in the corner recirculation zone. A 13.8% H_2 addition results in a continuous stable flame in the corner recirculation zone. The OH images with H_2-enrichement are similar to the CH_4 flames at higher temperatures.

The operating conditions of Q = 850slm and T_{ad} = 1240 +/- 15 C are near the lean stability limit of CH_4. These conditions were chosen to illustrate the effect of H_2 addition near the LBO limit, where it has the most potential to be beneficial. Figure 5.19 shows four flame images, two with and two without H_2-enrichment. The results show that the OH distributions are irregular, probably due to the turbulent fluctuations in the local flow field. The flame without H_2 (X_{H2}=0.0) is highly shredded and intermittent, and it appears to be nearly extinguished in Figure 5.19 (b). Large CO emissions can be expected to form in this highly strained flame resulting in poor combustion efficiency, as evidenced by the measurements shown in Figure 5.9. The flame with H_2 addition however reveals a wider region of high OH concentrations. Furthermore, the OH distributions are more continuous, the peak OH levels along the outer edges of the flame are higher, and the flame does not experience local extinction. These results show that the OH levels increase in a H_2-enriched flame, and suggest that the elevated radical pool is responsible for the improved flame stability observed.

Although single-shot OH measurements are important, a global understanding of the flame structure is gained from statistical data comprised of

time-averaged mean and RMS images of OH concentrations. A set of 600 single-shot images was used to obtain the statistical data. Figure 5.20 shows time-averaged OH PLIF images for X_{H2} = 0.0, 0.12 and 0.29. The operating conditions were same as those in Figure 5.17, i.e., Q = 700slm and T_{ad} = 1240C. Figure 5.20 shows only a modest change in the peak OH levels with increased H_2 addition. The location of peak OH levels was unaffected by H_2 addition. However, the flame structure is significantly altered with the addition of H_2. At X_{H2} = 0.0, the OH level is negligible in the corner recirculation region suggesting a lack of combustion in the corner recirculation region. This result is consistent with the luminous photograph of the flame in Figure 5.17 (a). At X_{H2} = 0.12, the OH extends into the corner recirculation zone along a layer adjacent to the inner wall of the combustor. Further increase in H_2 from X_{H2} = 0.12 to 0.29 results in high OH concentrations extending across a wider portion of the corner recirculation zone.

The corresponding RMS OH PLIF images are shown in Figure 5.21. Evidently, the highest fluctuation levels occur in the layer located between the incoming reactant stream and the centerbody recirculation zone. Large fluctuations in OH levels reflect the movement of the flame as it responds to the local flow turbulence. Note that the peak RMS OH levels are comparable to the peak mean OH levels. At X_{H2} = 0.0, the RMS OH values are near zero in the corner recirculation zone because there is no combustion occurring there. At X_{H2} = 0.12, the flame is present intermittently in the corner recirculation zone, resulting in large OH fluctuations between zero OH and high flame values.

Finally, at X_{H2} = 0.29, the combustion is continuous and stable in this zone, resulting in reduced RMS OH levels.

To facilitate a direct comparison of the OH levels, flow conditions were determined such that the H_2 addition could be varied without altering the global flame structure. It was found that for Q = 850 slm and T_{ad} = 1275 C, the flame structure was similar to that shown in Figure 5.17 (a), i.e., no flame in the corner recirculation zone and a flame that has moved somewhat away from the combustor wall, as X_{H2} was varied from 0.0 to 0.12. Time-averaged horizontal profiles of OH signal strength corresponding to these conditions are presented in Figure 5.22 (a) at y = 3.0 cm. Evidently, there is a noticeable increase in the OH levels when a moderate amount of H_2 is added to CH_4. However, the addition of larger amounts of H_2 does not proportionally increase the peak OH concentration. For example, an increase in X_{H2} from 0.06 to 0.12 caused only about 3% increase in the maximum OH level.

The OH mole fraction profiles from strained premixed flame calculations are shown in Figure 5.22 (b) for different fuels at adiabatic flame temperature of 1400C and strain rate of $645s^{-1}$, which is near the strain extinction limit of the CH_4 flame. The vertical coordinate in Figure 5.22 (b) is the distance from the stagnation plane. The computed OH mole fraction profiles support the experimental finding that the peak OH values increase non-linearly with increasing H_2 content in the CH_4 fuel. The similarity in shape of the experimental and computed profiles in Figures 5.22 (a) and (b) is however coincidental because the calculations simulate the flame characteristics at the local flow conditions.

As noted earlier, the H radical is an important species to affect flame extinction. Calculated concentrations of the H radical are shown in Figure 5.23 for several flames at an adiabatic equilibrium temperature of 1400 C and strain rate of $645s^{-1}$ for different concentrations of H_2 in the fuel. Although the maximum H levels are similar for all the flames, the location of the peak value differs. As the amount of H_2 in the fuel is increased, the location at which the H radical peaks moves farther from the stagnation plane. Evidently, the flame becomes more stable with H_2 addition, and is able to stabilize farther from the stagnation plane. In addition to increasing the chemical reaction rates, this allows more time for combustion reactions to approach completion, thereby raising stagnation point flame temperatures.

5.5 Summary of global flame characteristics

The adiabatic flame temperatures at flame instability and LBO were used to compare the stability characteristics of NG blended with different reactive or non-reactive species. Results show that the LBO limit was extended by adding H_2 or O_2 to the NG fuel. Adding LPG to NG slightly increased the flame temperature at LBO. The LBO temperature was not affected by CO_2 or N_2 in the NG fuel. The H_2-enriched NG flame was least sensitive and the LPG-enriched NG flame was most sensitive to the total fuel-air flow-rate or the flow strain.

PLIF measurements of the OH radical were made to understand the effects of H_2-enrichment on CH_4 flames near LBO. Both instantaneous and time-averaged data were measured. The lean stability limit was lowered by the addition of H_2 to the fuel, as expected. This improved stability with H_2-

enrichment is postulated to be a direct result of increasing the H, O, OH radical concentrations, which increases several key reaction rates. Results showed that moderate amounts of H_2-enrichment led to significant increases in the OH radical concentrations. Increasing amounts of H_2-enrichment to the higher levels tested in this report only marginally increased the radical concentration for the conditions tested. Perhaps if the strain rates in the combustor were higher, the differences would become more marked. Results also showed that as the equivalence ratio, and hence the adiabatic flame temperature, was increased, the OH concentrations increased significantly. This was expected since reaction rates increase with temperature.

Numerical modeling of strained, opposed, premixed, planar jet combustion was performed using RUN-1DL. The numerical results agreed with the OH PLIF measurement results. The ability of H_2-enriched fuel to withstand higher strain rates before extinction was demonstrated. Furthermore, it was calculated that the H_2-enriched fuel was also able to burn at lower adiabatic flame temperatures, which may reduce pollutant emissions. The effect of H_2 addition was shown to be non-proportional, with the more moderate amounts of H_2-enrichment producing the largest changes in the OH concentrations. The effects of equilibrium flame temperature were demonstrated for several cases over a range of temperatures, and the trend of insignificantly increasing OH concentrations was verified. Results were also shown for the H radical, as it is important in several reactions including the above mentioned chain branching reaction. There was no significant change in peak H levels with H_2 addition, but

the peaks did progressively move away from the stagnation plane as the flame was able to stabilize further from the plane. The H radical concentrations increased with equilibrium flame temperature, and the peak values moved farther from the stagnation plane.

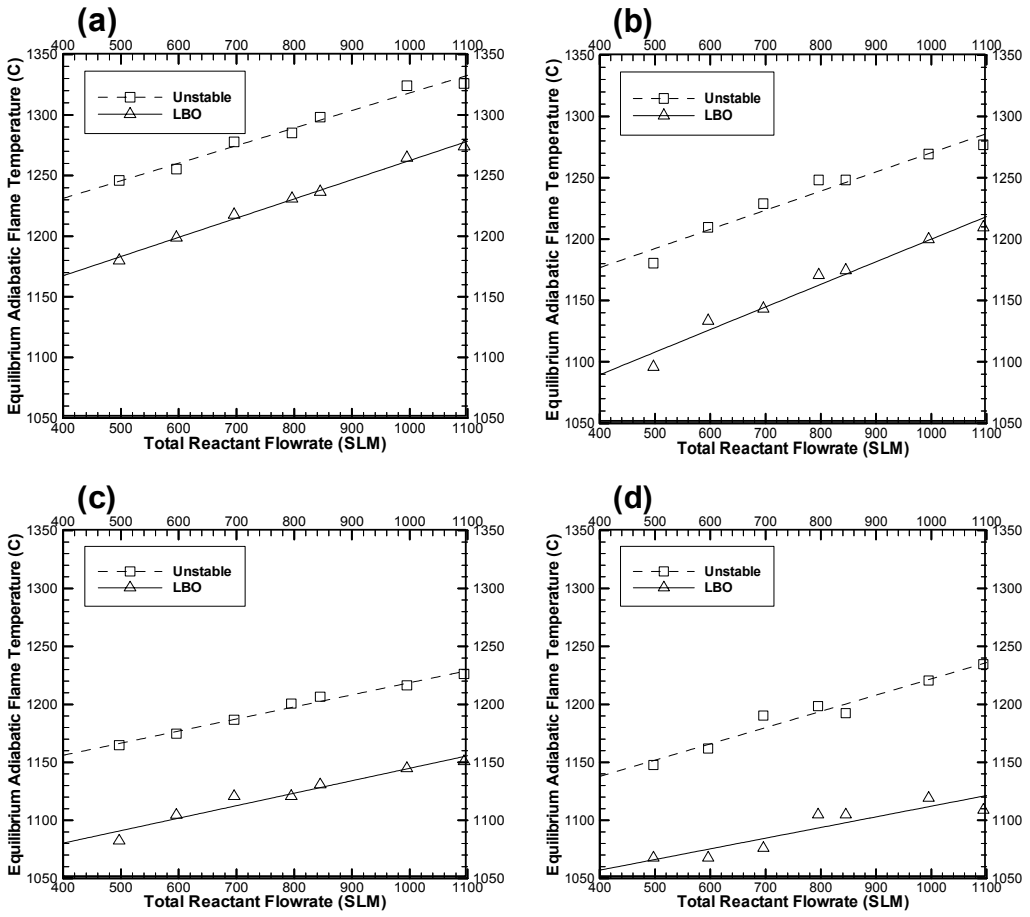

Figure 5.1. Flame stability and lean blow out limits of H_2-enriched NG (a) X_{H2} = 0.0, (b) X_{H2} = 0.12, (c) X_{H2} = 0.22, and (d) X_{H2} = 0.29.

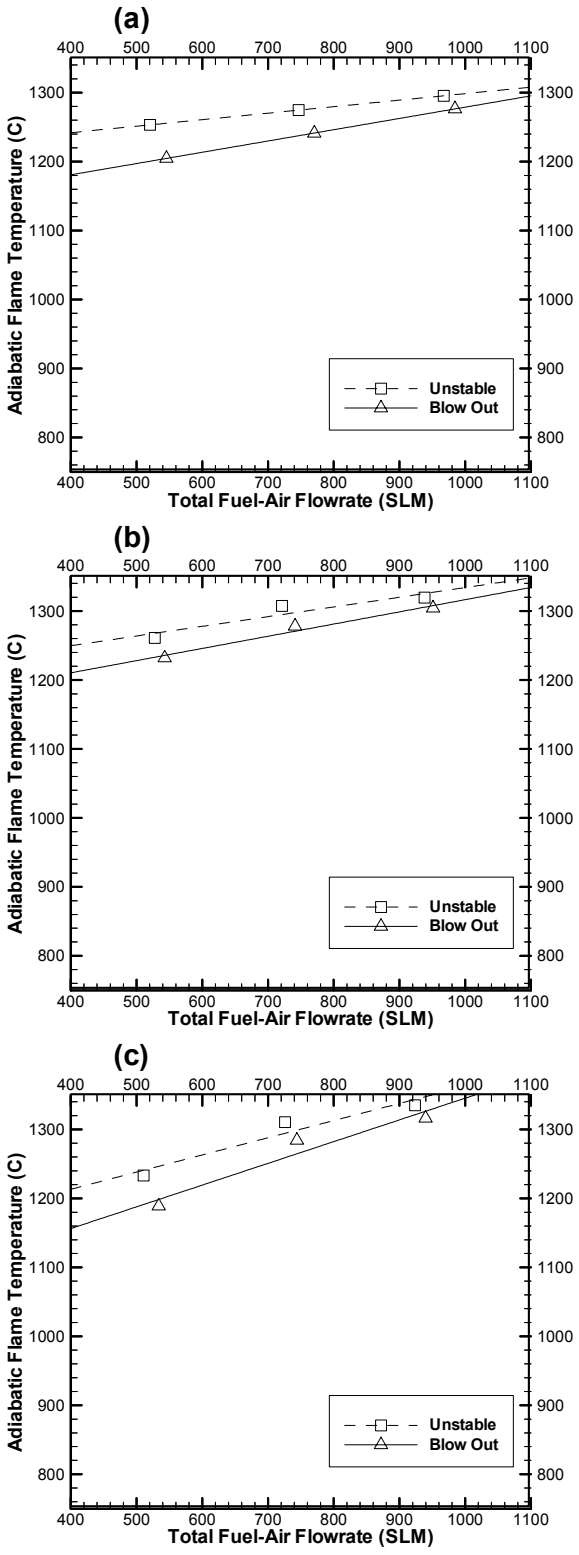

Figure 5.2. Lean blow out limits of NG with: (a) 19% LPG, (b) 28% LPG, (c) 38% LPG.

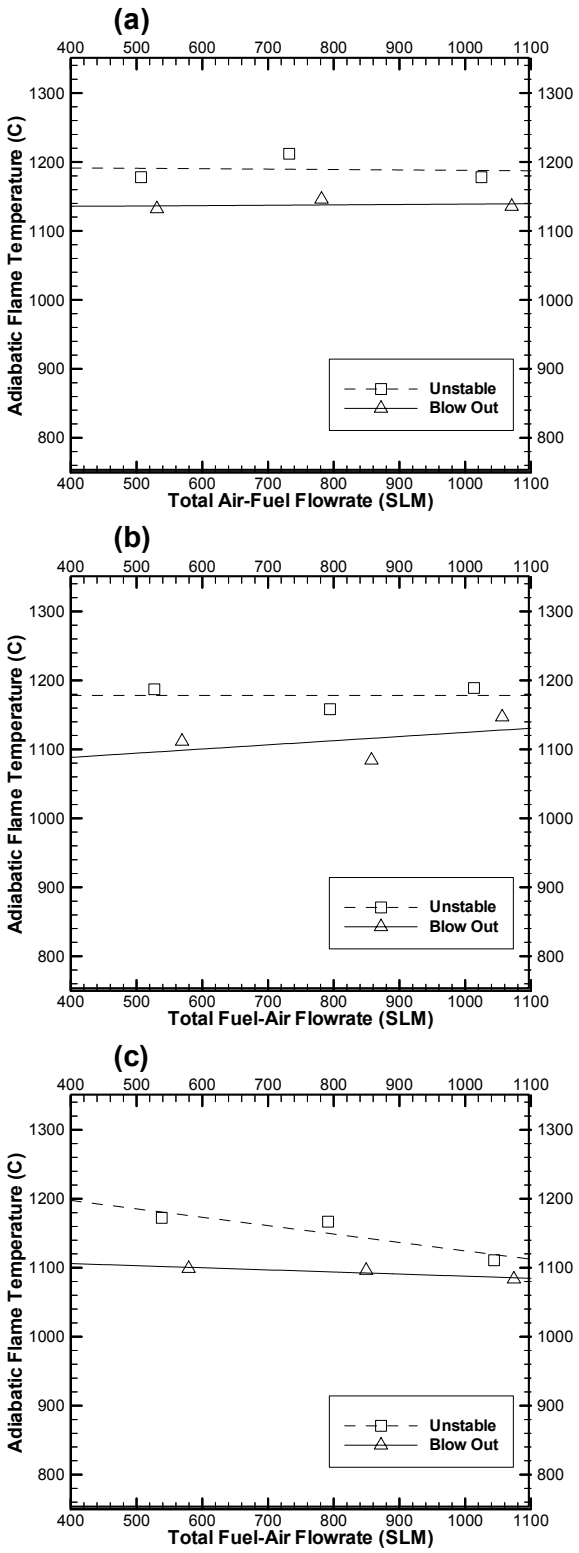

Figure 5.3. Lean blow out limits of NG with: (a) 20% O_2, (b) 30% O_2, (c) 40% O_2.

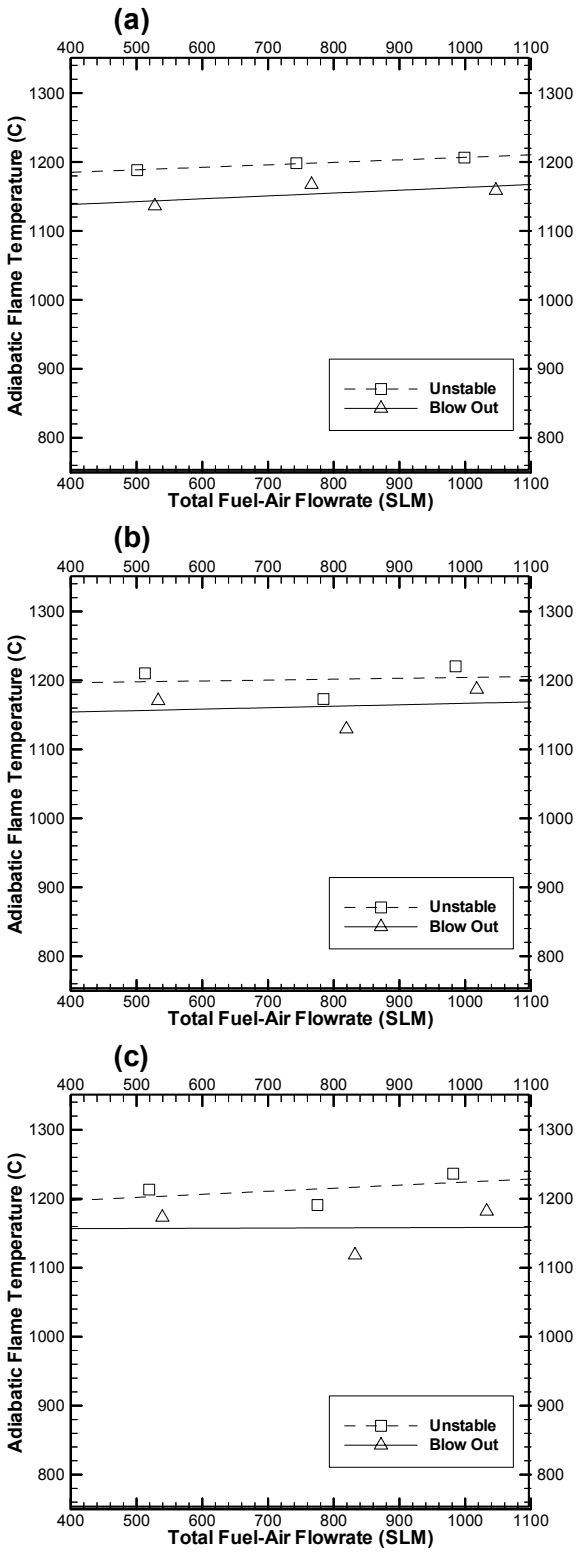

Figure 5.4. Lean blow out limits of NG with: (a) 20% N_2, (b) 30% N_2, (c) 40% N_2.

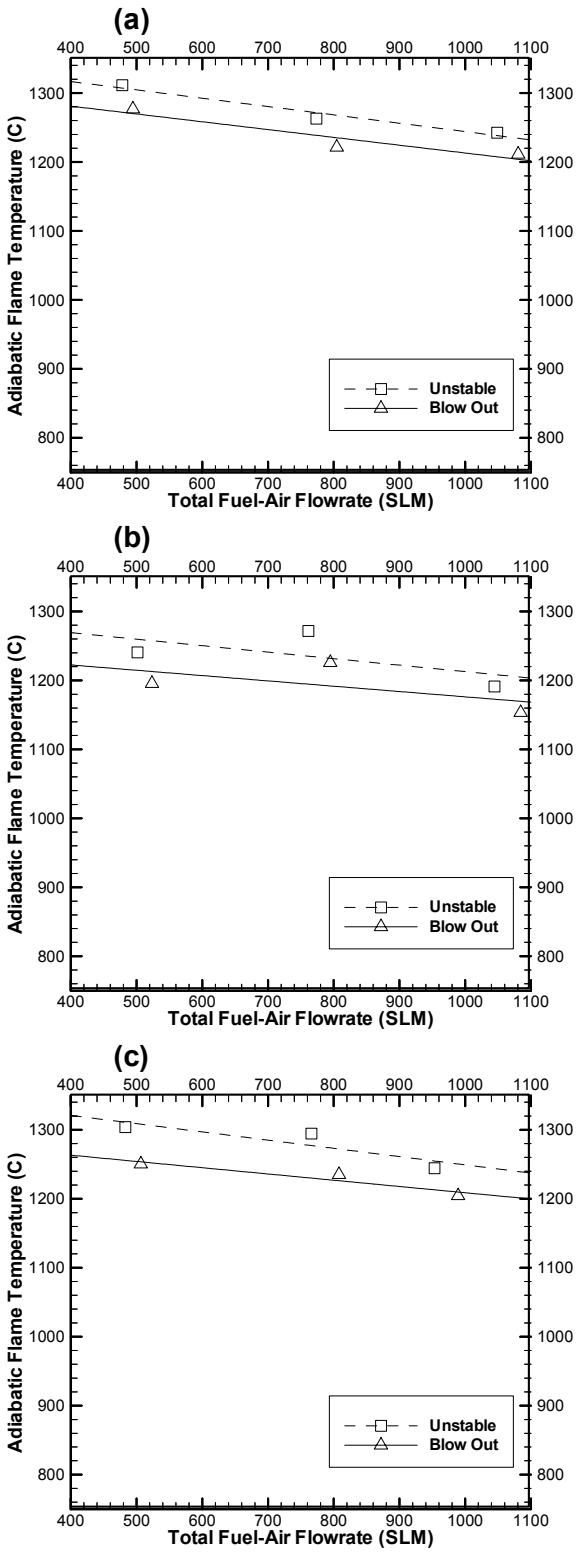

Figure 5.5. Lean blow out limits of NG with: (a) 20% CO_2, (b) 30% CO_2, (c) 40% CO_2.

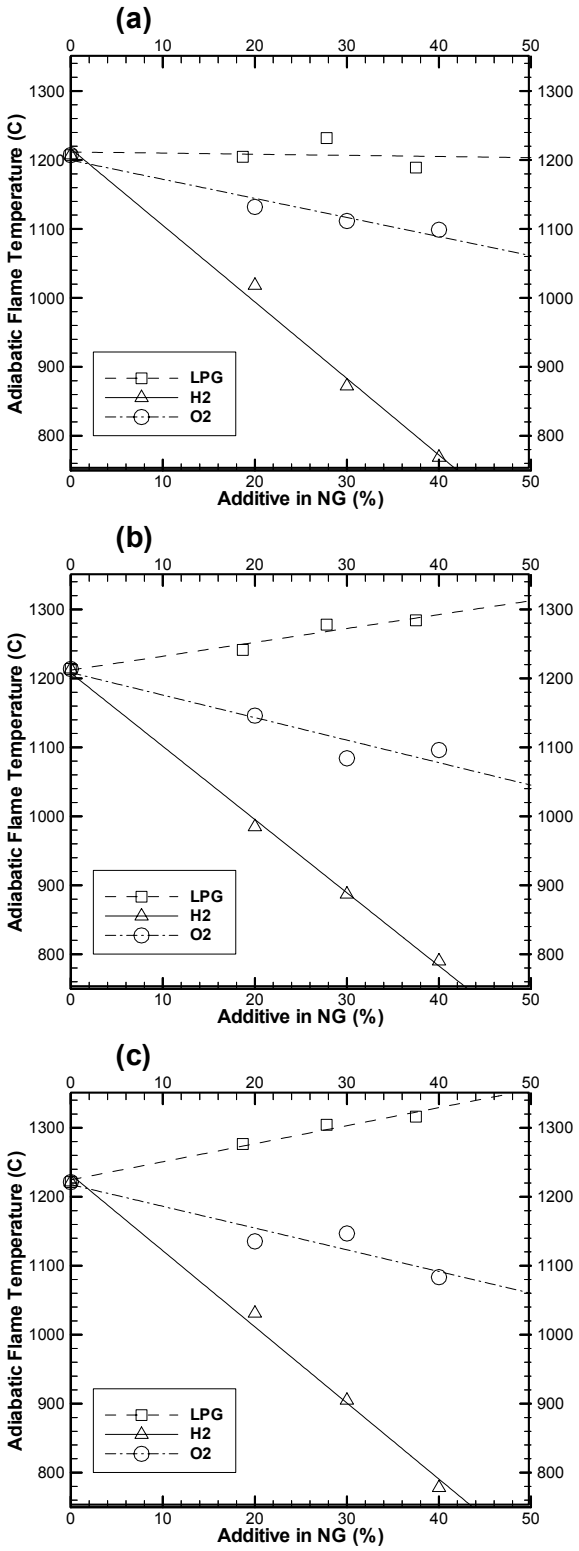

Figure 5.6. Effects of reactive species on lean blow out temperature in NG flames for total fuel-air flows rates of: (a) 0.50, (b) 0.75, and (c) 1.0 m^3/s.

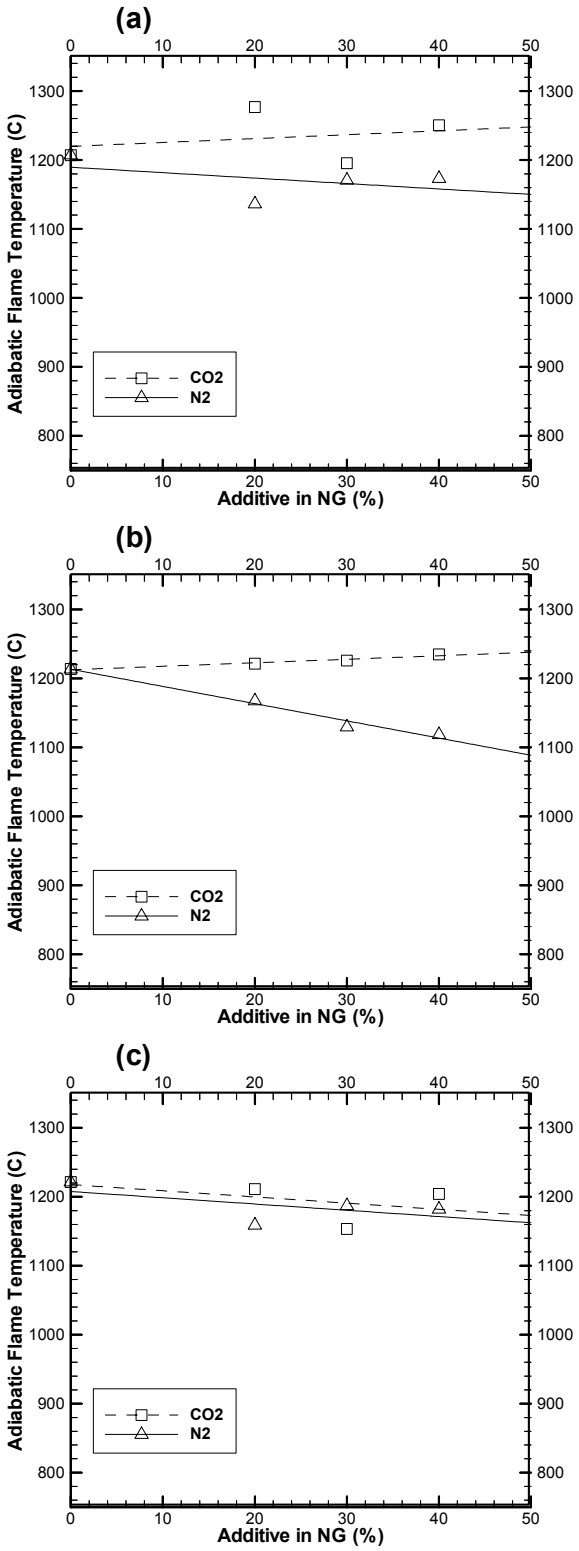

Figure 5.7. Effects of non-reactive species on lean blow out temperature in NG flames for total fuel-air flows rates of: (a) 0.50, (b) 0.75, and (c) 1.0 m^3/s.

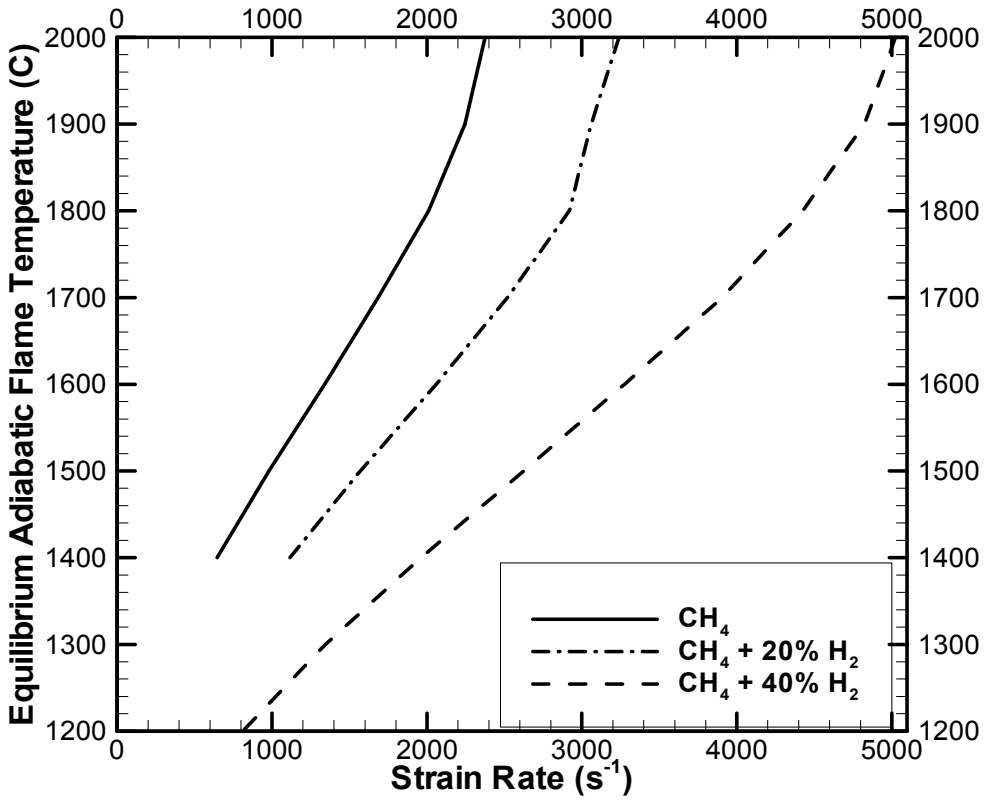

Figure 5.8. Extinction curves obtained from strained premixed planar opposed flow calculations.

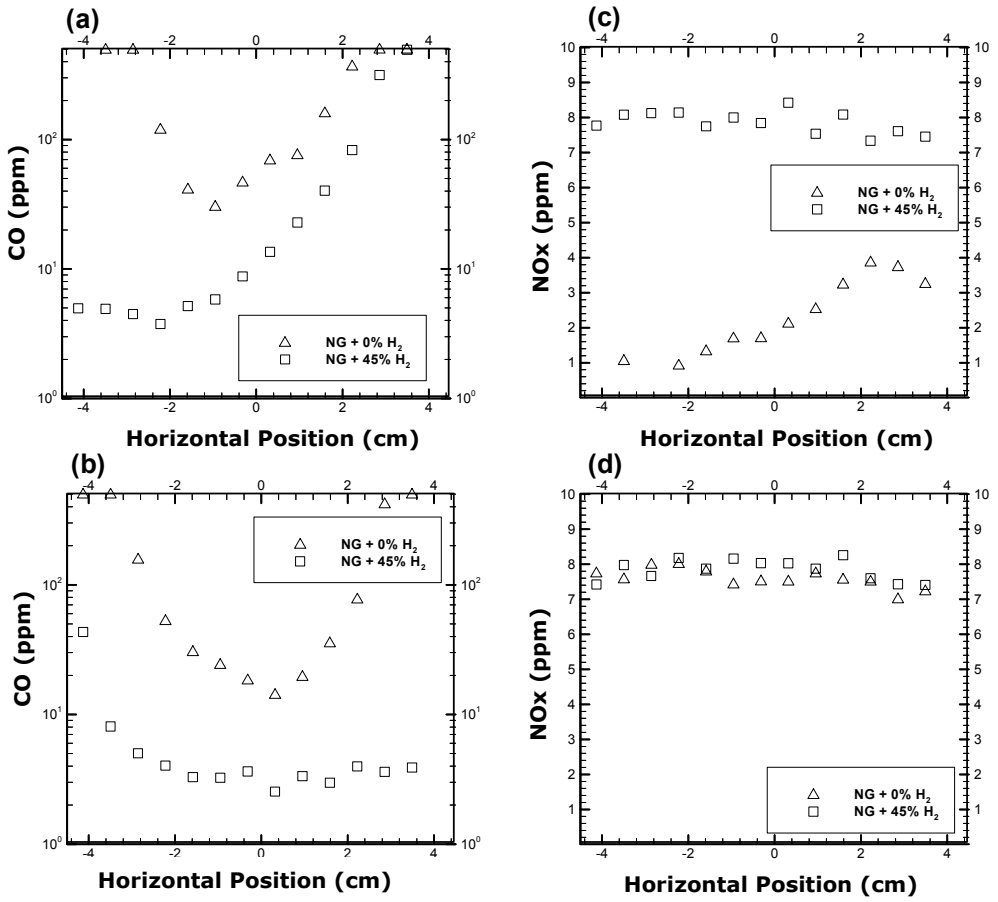

Figure 5.9. Horizontal profiles of CO and NOx concentrations at different vertical planes, (a) CO at y = 5.1cm, (b) CO at y = 20.3cm, (c) NOx at y = 5.1cm, (d) NOx at y = 20.3cm.

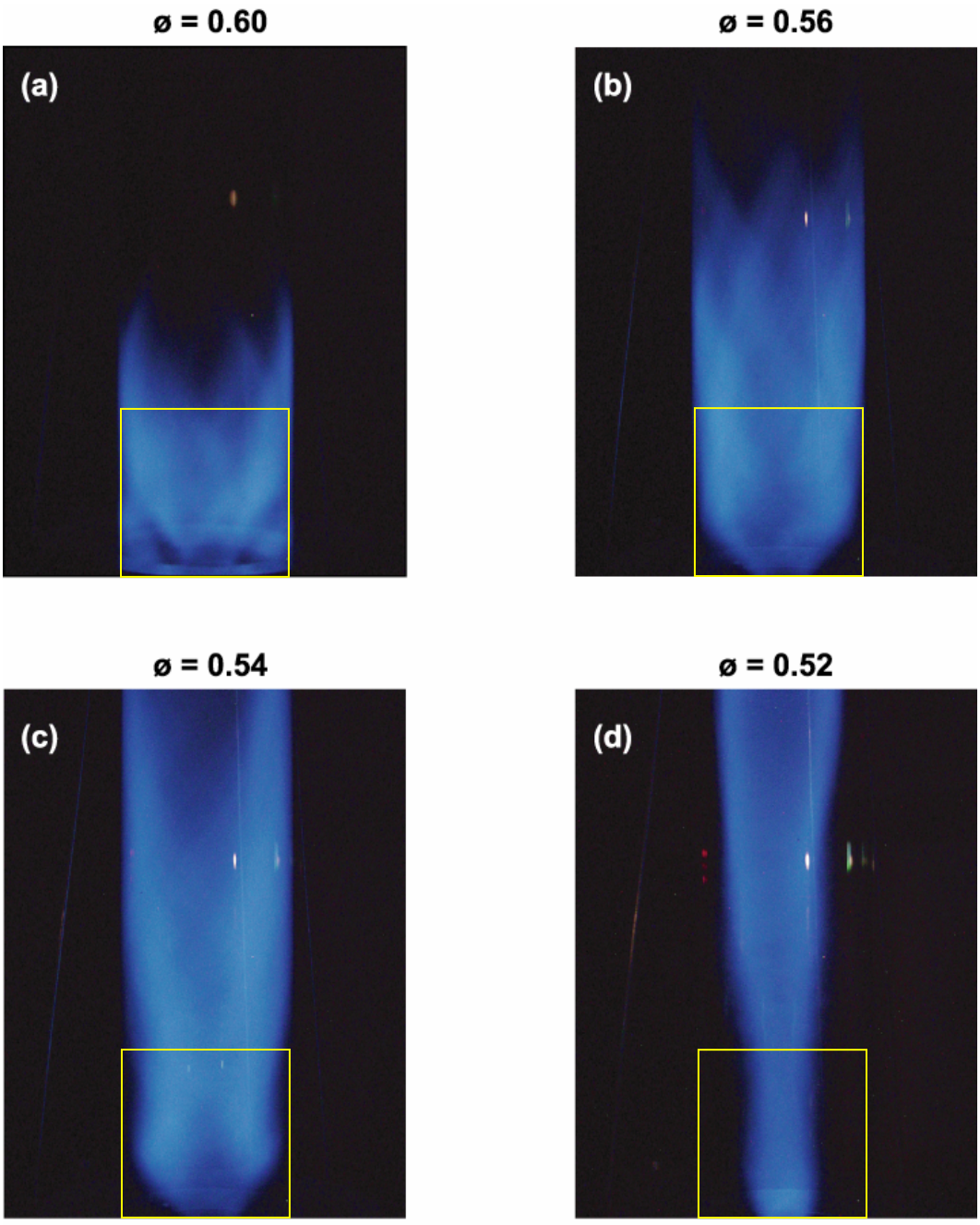

Figure 5.10. Direct flame luminosity photographs in swirl-stabilized burner. v = 14 m/s, X_{H2} = 0.0. a) ϕ = 0.0.60, Tad = 1385C; b) ϕ = 0.56, Tad = 1311C; c) ϕ = 0.54, Tad = 1274C; d) ϕ = 0.52, Tad = 1237C, the box indicates the PLIF measurement window.

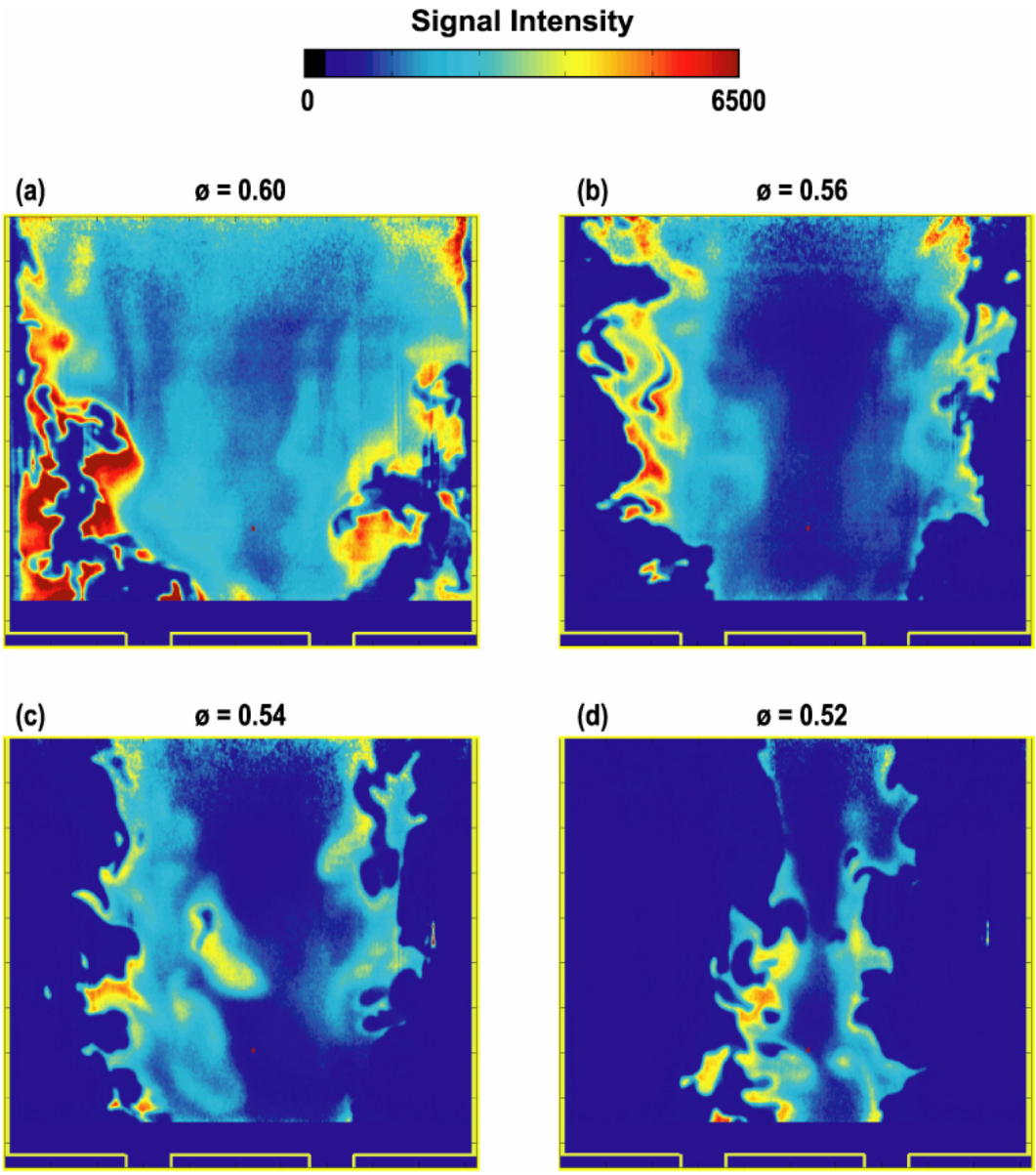

Figure 5.11. Single-shot, OH PLIF images in swirl-stabilized NG flame for the same flame sequence as the photographs in Figure 5.10. The false color map indicates OH mole fraction. Burner inlet nozzle location is indicated at the bottom of the image.

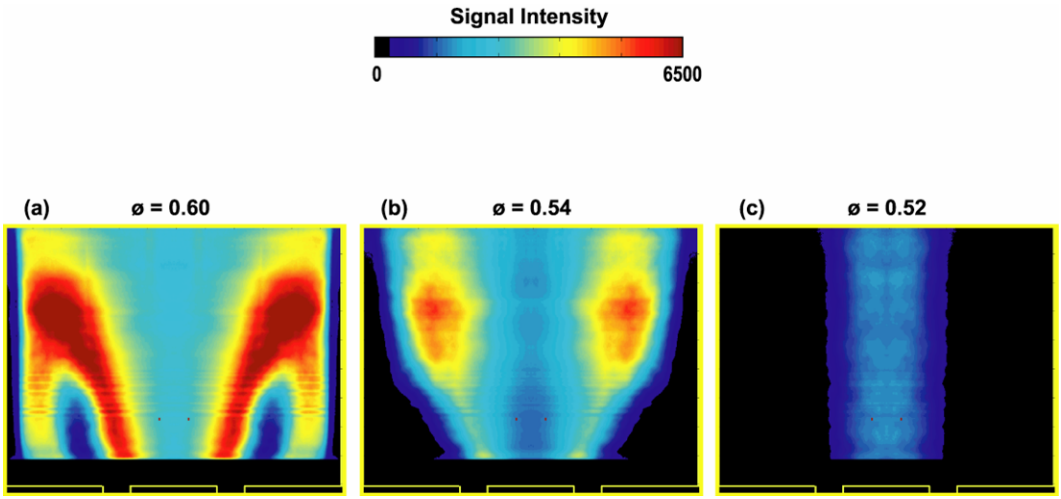

Figure 5.12. Time-averaged OH PLIF images in swirl-stabilized flame. X_{H2} = 0.0, v = 14 m/s. a) ϕ = 0.60 Tad = 1385 C; b) ϕ = 0.54 Tad = 1274 C; c) ϕ = 0.52 Tad = 1237 C.

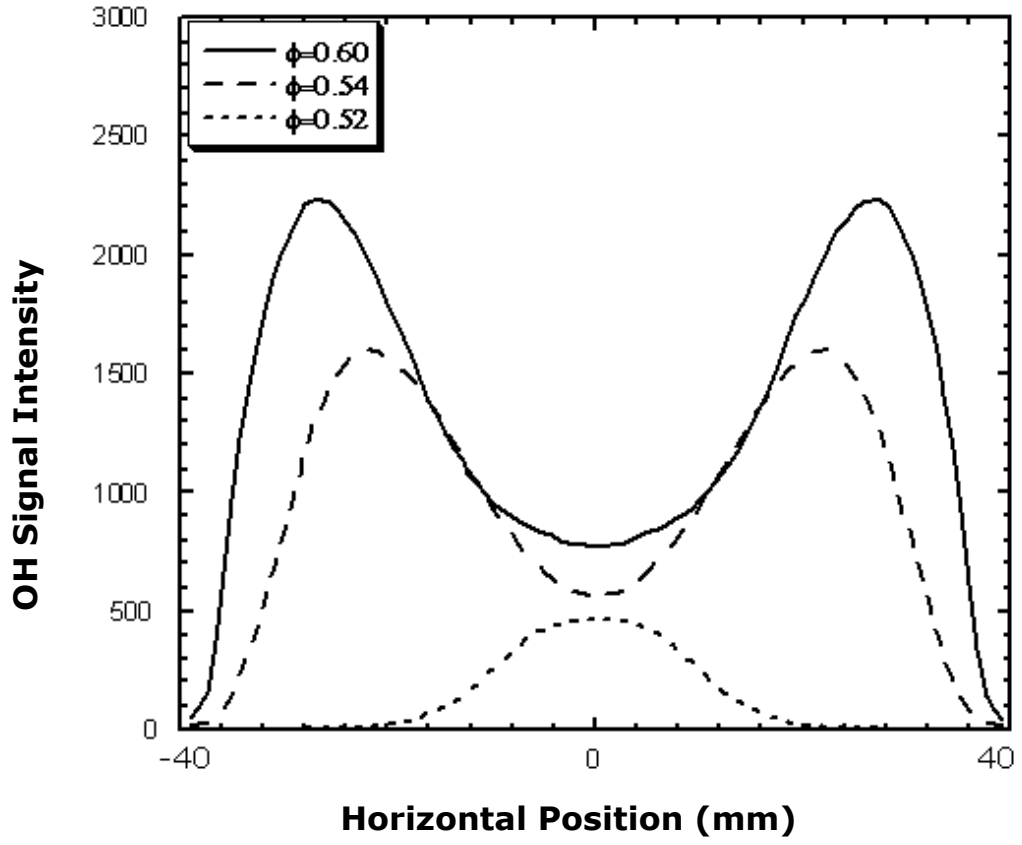

Figure 5.13. Horizontal profiles of OH intensity for different equivalence ratios at y = 30 mm. $X_{H2} = 0.0$, v = 14 m/s.

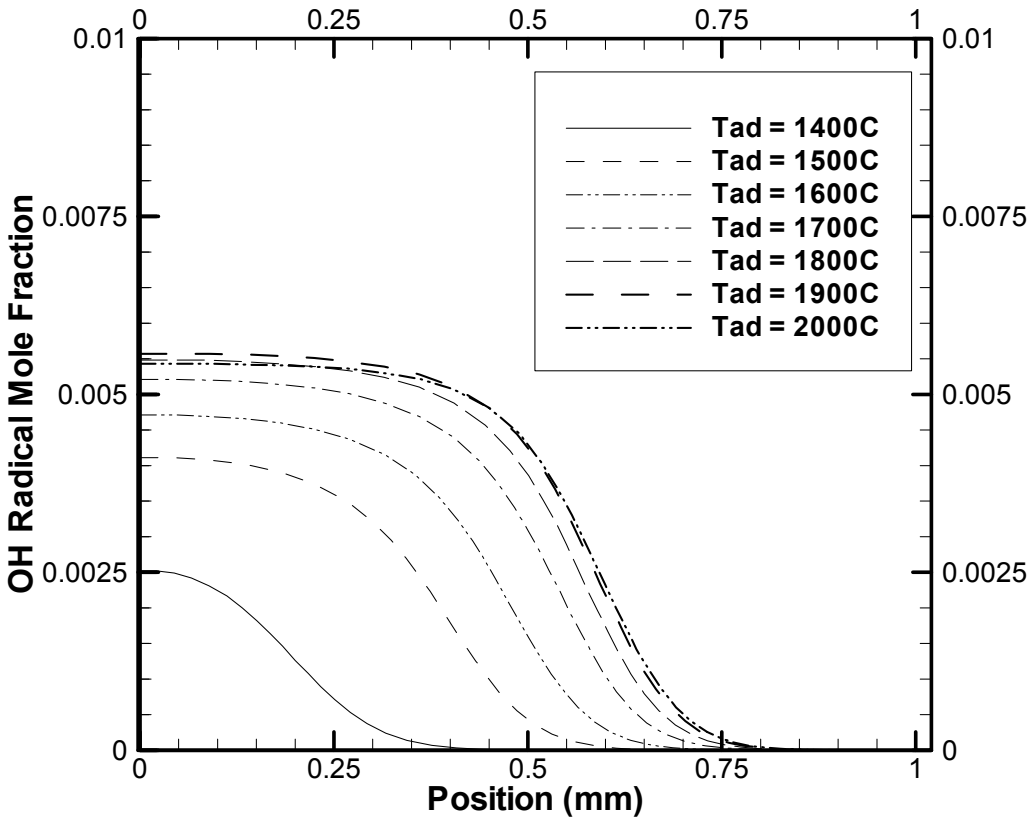

Figure 5.14. The effect of equilibrium adiabatic flame temperature on OH radical mole fractions for CH_4-air flames at a strain rate of 645 s^{-1}.

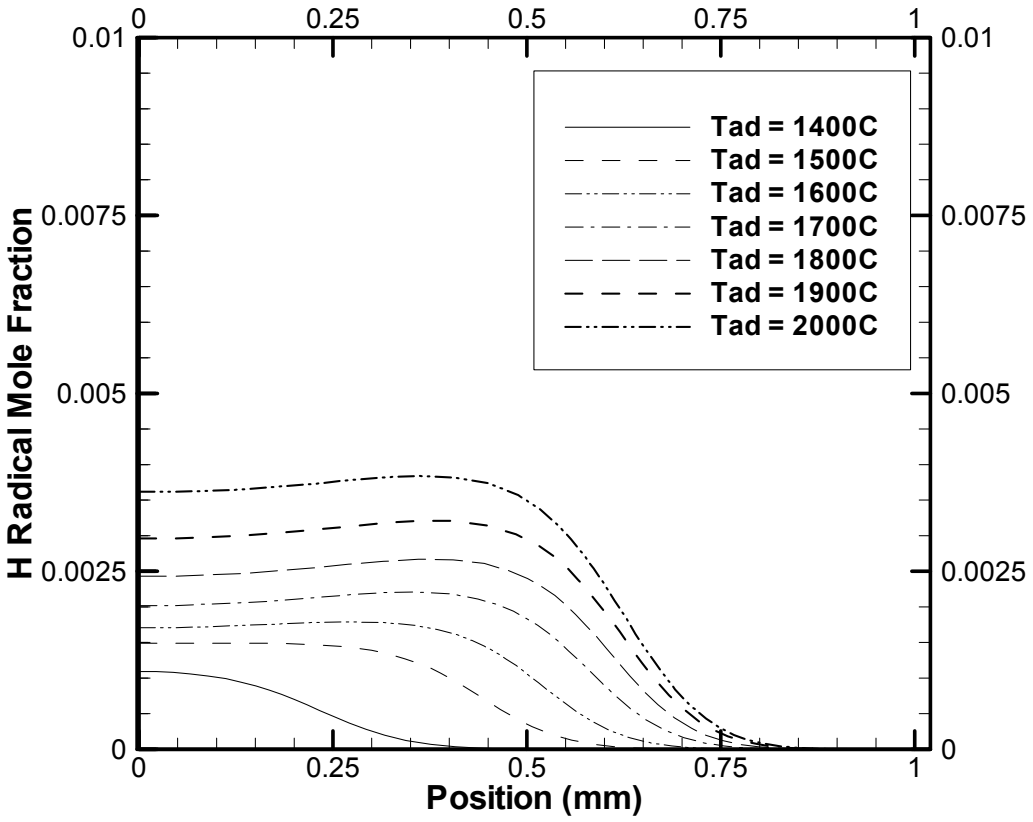

Figure 5.15. The effect of equilibrium adiabatic flame temperature on H radical mole fractions for CH_4-air flames at a strain rate of 645 s^{-1}.

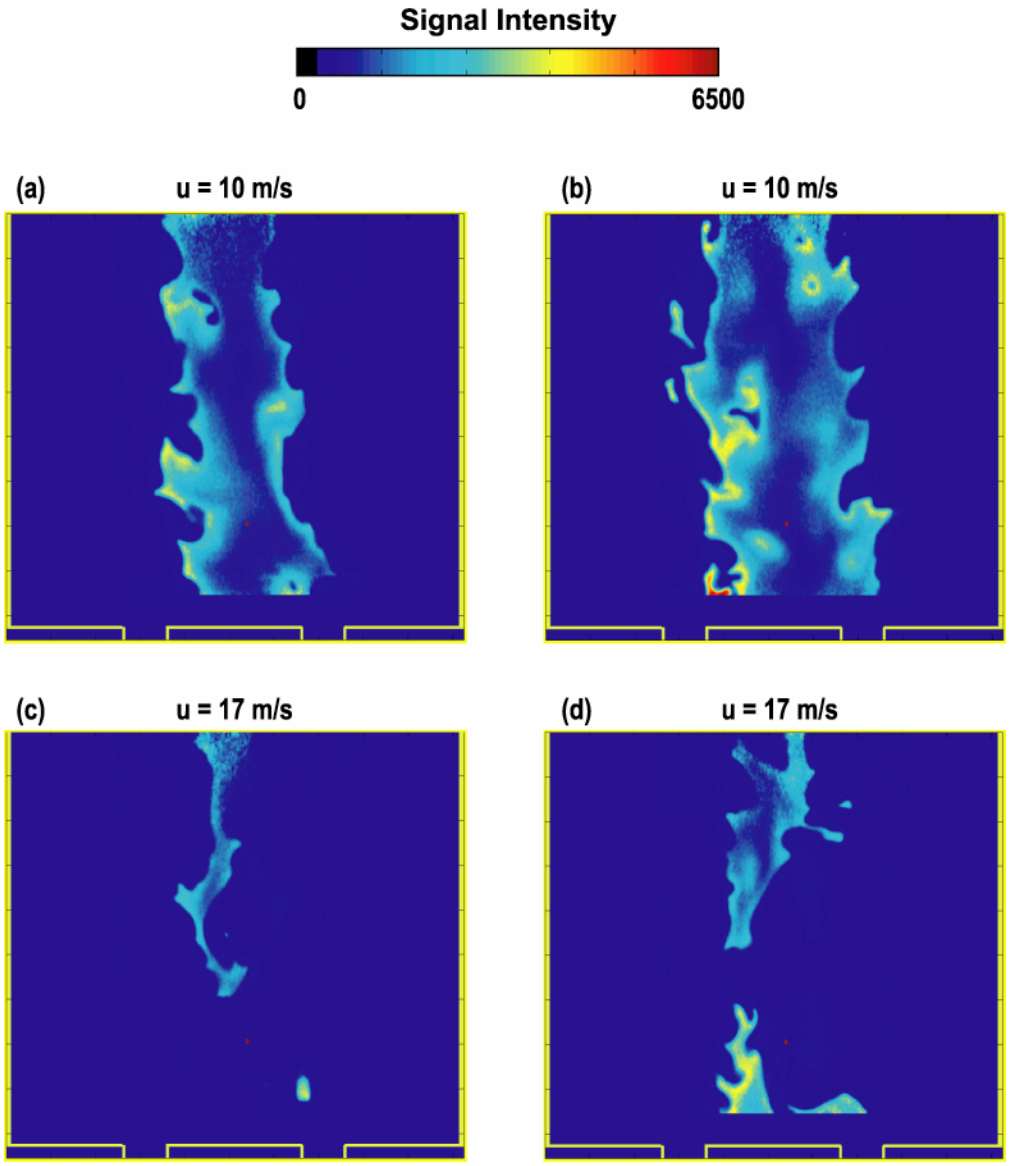

Figure 5.16. Single-shot, OH PLIF images in swirl-stabilized NG flame. X_{H2} = 0.0, ϕ = 0.52 Tad = 1237 C. a), b) v = 10 m/s; c), d) v = 17 m/s.

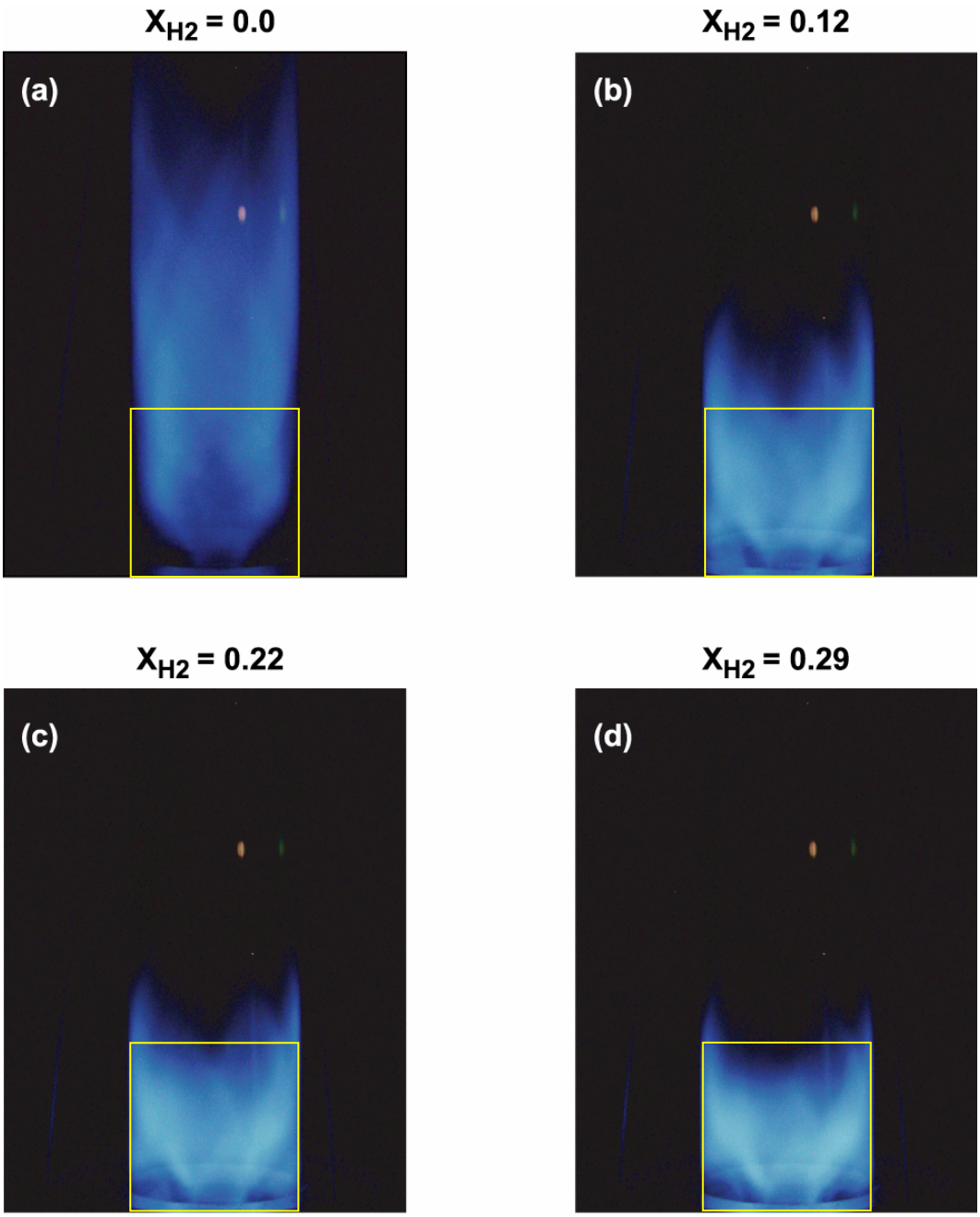

Figure 5.17. Direct flame luminosity photographs for Q = 700slm and Tad = 1290 +/- 20 C, (a) X_{H2} = 0.0, (b) X_{H2} = 0.12, (c) X_{H2} = 0.22, and (d) X_{H2} = 0.29, the box indicates the PLIF measurement window.

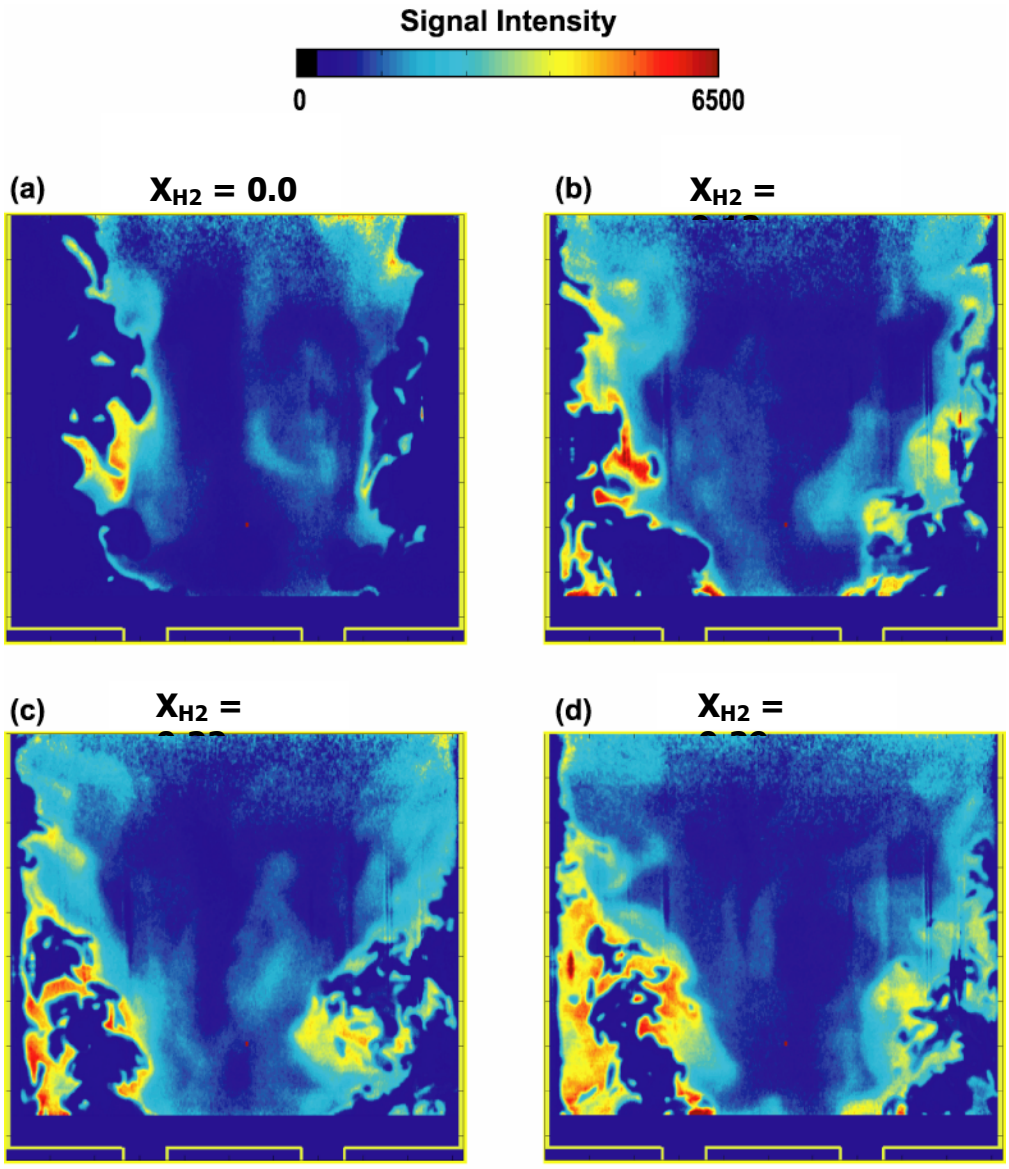

Figure 5.18. Single-shot, OH PLIF images in swirl-stabilized H_2-enriched flames for the same flame sequence as the photographs shown in Figure 5.17. The false color map indicates OH mole fraction. Burner inlet nozzle location is indicated at the bottom of the image.

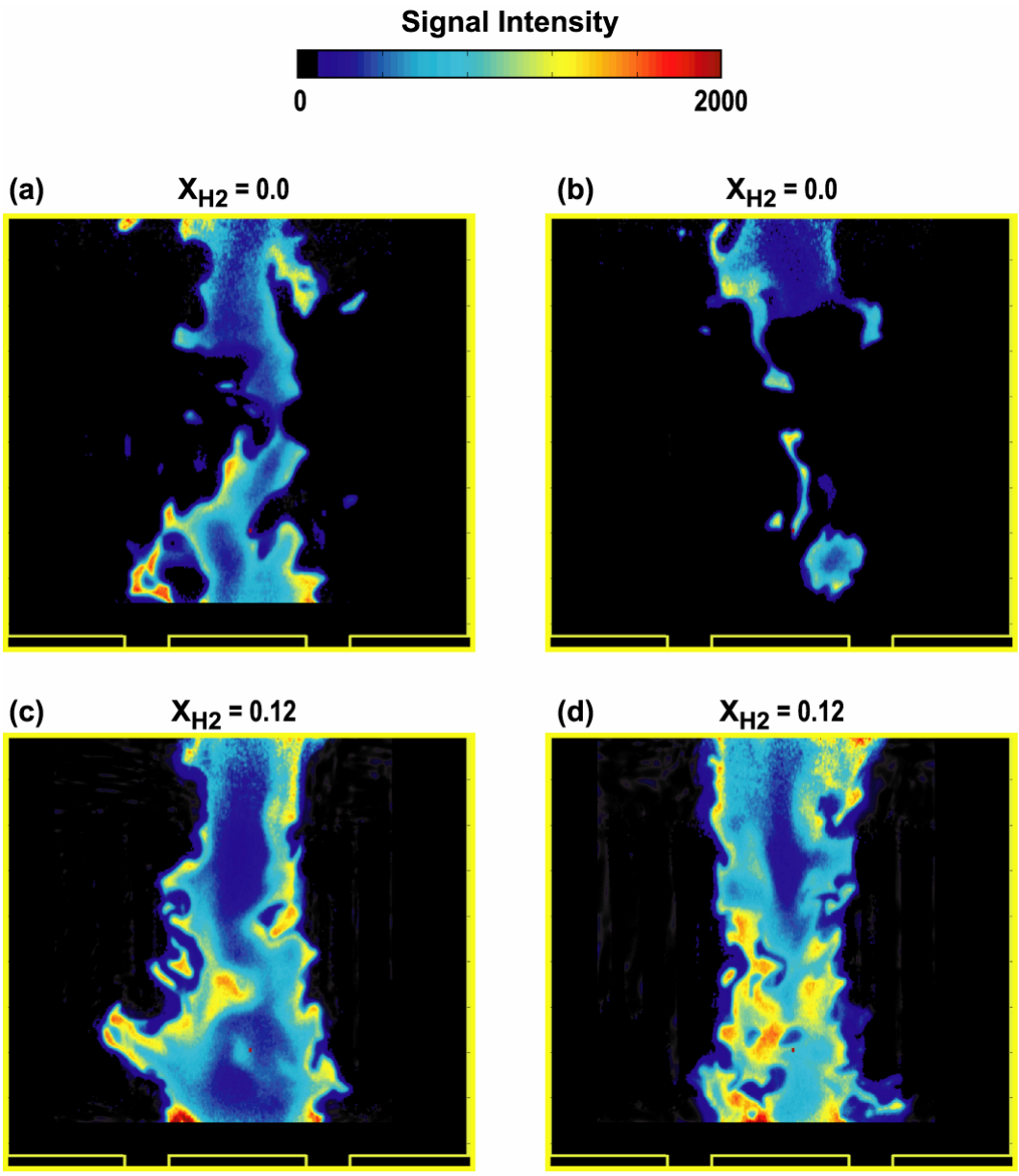

Figure 5.19. Single-shot, OH-PLIF images in unstable, tornado shaped flames for Q = 850 slm and Tad = 1240 C (a) and (b) $X_{H2} = 0$, (c) and (d) $X_{H2} = 0.12$.

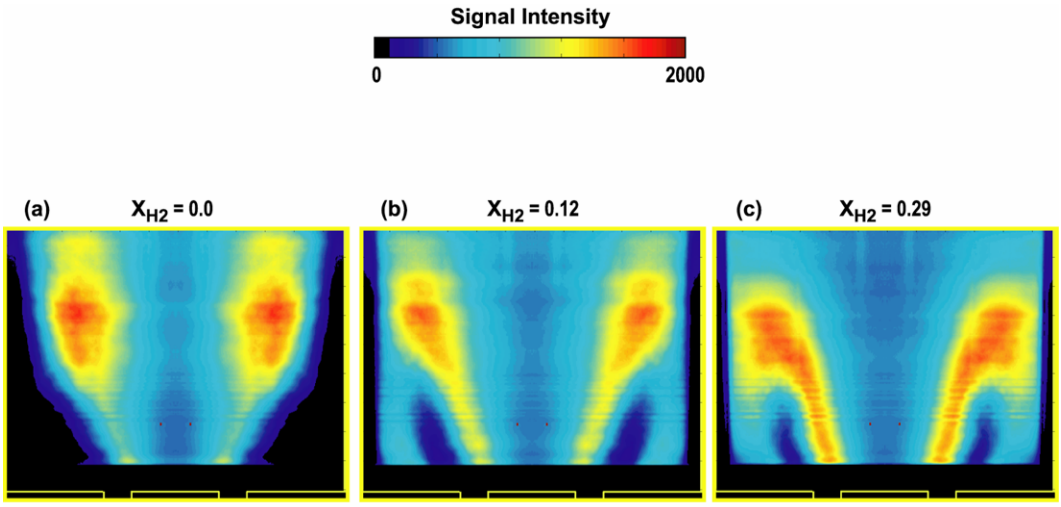

Figure 5.20. Time-averaged OH-PLIF images for Q = 700 slm and Tad = 1290 +/- 20 C. (a) X_{H2} = 0.0, (b) X_{H2} = 0.12, (c) X_{H2} = 0.29.

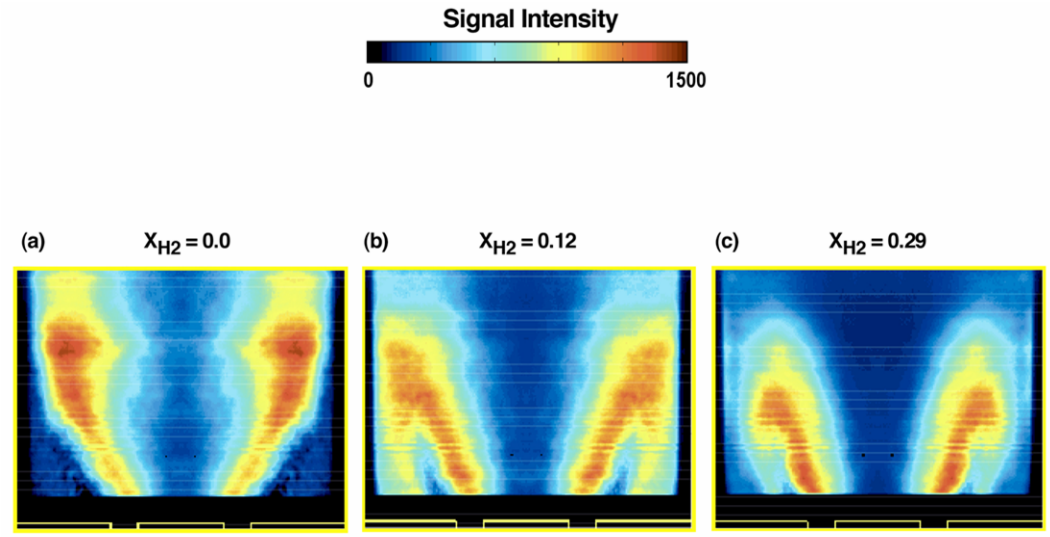

Figure 5.21. RMS OH-PLIF images for Q = 700 slm and Tad = 1290 +/- 20 C. (a) $X_{H2} = 0.0$, (b) $X_{H2} = 0.12$, (c) $X_{H2} = 0.29$.

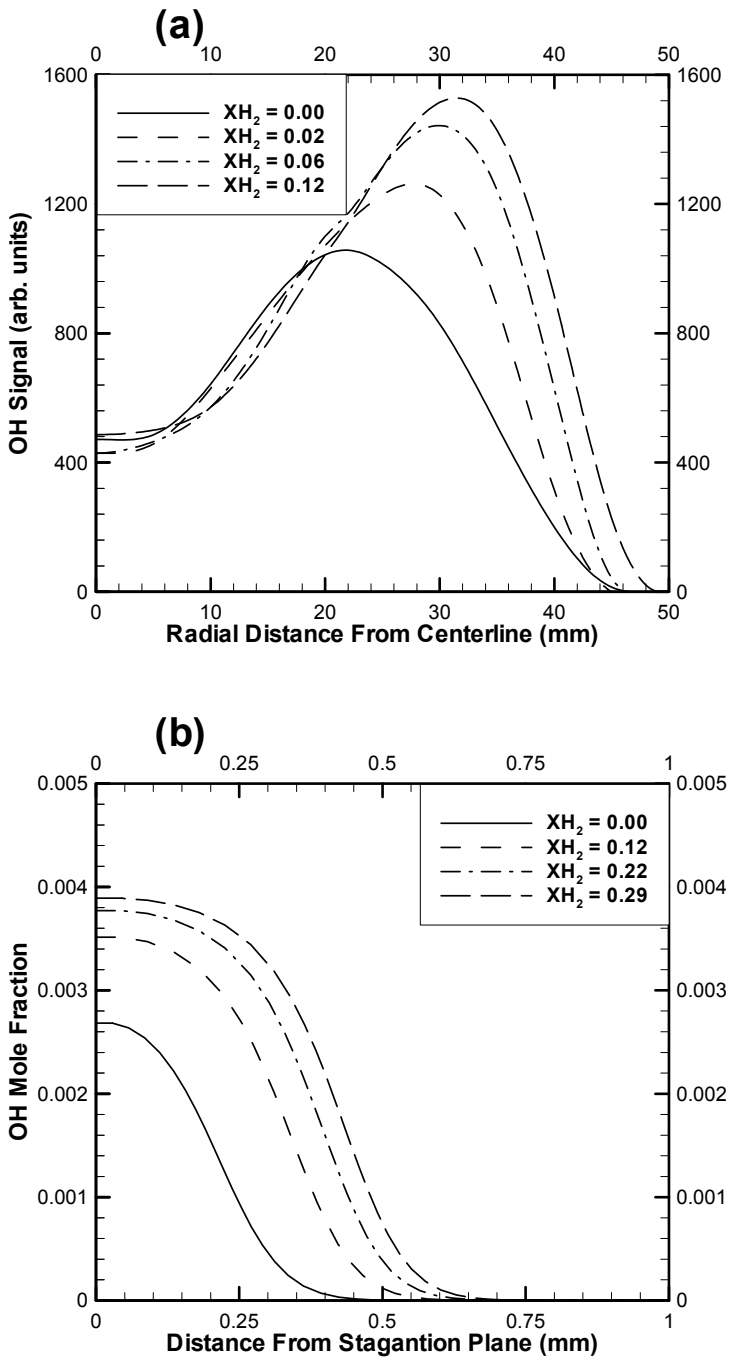

Figure 5.22. Effect of H_2 addition on OH concentration (a) Experimental for Q = 850 slm and T_{ad} = 1275 C, (b) Calculations for a strain rate of 645^{-1} and T_{ad} = 1400 C.

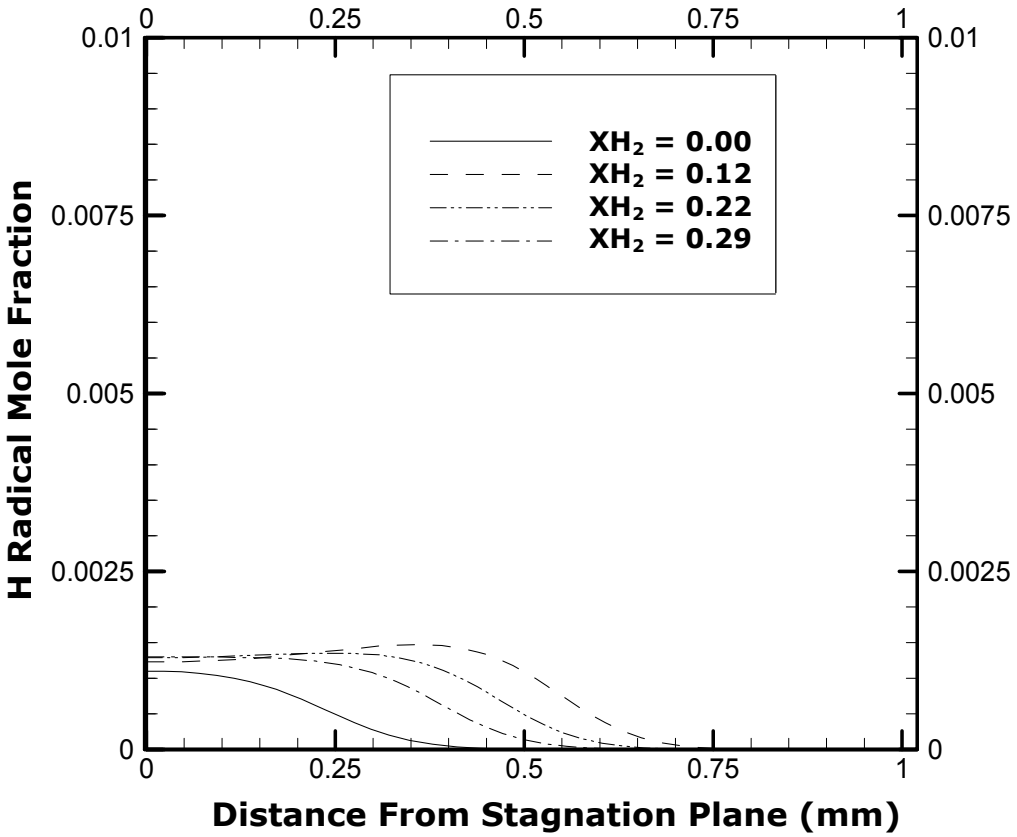

Figure 5.23. The effect of H_2-enrichment on H radical mole fractions for calculations at an equilibrium adiabatic flame temperature of 1400 C, and a strain rate of 645 s^{-1}.

CHAPTER 6: FLOW FIELD MEASUREMENTS

Several aspects of the flow fields of the flames and the non-reacting flow are presented next to show the effects of heat release and H_2 addition. The estimated Kolmogorov length scale varied between 0.01mm and 0.2mm, while the estimated Taylor microscale ranged from 0.1mm to 2.0mm. The spatial resolution of 0.9mm in the present study was inadequate to capture the smallest length scales. However, the measurements resolved the larger structures in the Taylor microscale. The Stokes numbers calculated based on these length scales show that the particles were able to capture all but the smallest Kolmogorov scales of motion

Data will be presented for three test cases in this chapter, non-reacting room temperature air, a pure CH_4 flame, and a 60% CH_4 and 40% H_2 flame. The swirl number, inlet velocity, and the calculated adiabatic flame temperature for both flames were 1.5, 10m/s, and 1350^0C, respectively. The Reynolds numbers were 13576, 13487, and 13117 for the non-reacting case, CH_4 flame, and the H_2-enriched CH_4 flame respectively. The difference in Reynolds numbers is due to the difference in viscosity and density of the mixtures.

6.1 Time-averaged velocity fields

Time-averaged velocity information is useful for determining the large scale structures in the flow, such as the size and shape of the recirculation zones. Figure 6.1 shows time-averaged velocity vectors for the 30 mm by 30 mm window indicated in Figure 2.6. The left side of the image corresponds to the combustor centerline, and the bottom edge is the inlet plane. The inlet annulus is

located between horizontal coordinates of 10 mm and 20 mm, and is denoted by the high jet velocity. The combustor wall is outside the field of view. Five distinct regions of the flow, similar to those in previous studies, are observed in Figure 6.1. The first region is the inlet jet flow directed downstream and horizontally outward in the combustor. The sudden expansion causes a circulation to develop at the intersection of the combustion inlet plane and the combustor wall, which is referred to as the corner recirculation zone. The central region of the combustor in backflow is the central recirculation zone. The fourth region is the inner shear layer formed between the inlet jet and the central recirculation zone. Finally, an outer shear layer is present between the inlet jet and corner recirculation zone.

An examination of Figure 6.1 reveals differences in the time-averaged flow field of non-reacting flow, CH_4 flame and H_2-enriched CH_4 flame. The flow velocities in the central recirculation region are on the order of 1-2 m/s for the non-reacting case. However, in case with flames, the flow velocities in this region are on the order of 3-4 m/s. The heat release associated with combustion results in volumetric expansion to accelerate the flow, thereby leading to higher velocities in the central recirculation zone. Figure 6.1 shows that the size of the central recirculation zone is about the same for the non-reacting flow and CH_4 flame. A slightly narrower recirculation region is observed for the H_2-enriched flame. These results differ from those in the unconfined configuration of Ji and Gore (2002). In an unconfined system, the heat released in the flame expands the flow in the horizontal direction to produce a wider central recirculation zone. In

the present configuration, the horizontal expansion is constrained by the combustor wall.

Figure 6.1 shows that the jet region is similar for the non-reacting flow and CH_4 flame. In both cases, the jet is oriented at approximately a 45^0 angle with respect to the combustor inlet plane. This result suggests that the CH_4 flame is unable to sustain combustion in the highly strained jet region, where conditions similar to the non-reacting flow are maintained. Reactions are primarily confined to the inner shear layer, where thermal expansion has produced higher flow velocities compared to the non-reacting flow. The jet flow structure for the H_2-enriched flame is significantly different from the previous two cases. The jet region is broader and it is oriented at a 60^0 angle with respect to the combustor inlet plane. Increase in momentum caused by the heat release in the jet region would explain this observation, suggesting that the H_2-enriched flame is able to sustain combustion in the highly strained jet region. Figure 6.1 shows that a corner recirculation region is present for all cases, although full visualization was constrained by the limited field of view. The corner recirculation zones for the non-reacting flow and CH_4 flame are similar, indicating lack of reactions in this region in agreement with flame luminosity and OH PLIF measurements by Schefer et al. (2002). Flow velocities in the corner recirculation zone are higher for the H_2-enriched flame, indicating thermal expansion in the presence of reactions. Overall, results presented in Figure 6.1 provide direct evidence that the average flow structure is affected not only by combustion but also by the fuel composition, which determines the location and rates of heat release.

6.2 Instantaneous velocity fields

In addition to the large scale features found in time-averaged data, smaller short lived structures exist. These structures can affect the flame characteristics causing it to become distorted or extinguished in some cases, and therefore must be understood. Figure 6.2 shows instantaneous velocity vectors at two random instants of time for the three cases. In each case, significant temporal variations are observed because of the turbulent nature of the flow. The instantaneous flow field for the non-reacting case in Figures 6.2 (a) and (b) shows that the velocity magnitudes are similar to those observed in the time-averaged flow field. One major difference is the smaller vortical structures not observed in the averaged flow field. The recirculation zones observed in the averaged flow field are still present. According to Figures 6.2 (c) and (d), the magnitude of the velocities in the CH_4 flame is higher than the non-reacting flow, most notably in the central recirculation region. Smaller vortical structures observed in the inner shear layer are expected to affect the flame stabilization. For the H_2-enriched flame, the inlet jet in Figures 6.2 (e) and (f) is observed to have shifted noticeably downstream, as in the time-averaged flow field. Overall, results in Figure 6.2 show that the average flow field does not represent the instantaneous flow field, which contains random smaller vortical structures. Thus, instantaneous flow measurements are necessary to characterize flame properties in a turbulent flow.

6.3 Turbulence fields

Turbulence fields are a means of measuring the action of the small vortices and flow structures observed in the instantaneous velocity fields. The

RMS and the TKE are measures of the random fluctuations in the flow field, and the Ked measures the conversion of kinetic energy of these turbulent fluctuations into internal energy. Figure 6.3 shows plots of the RMS velocity fields for the three cases. For all cases, the horizontal RMS velocity peaks in the outer shear layer at the inlet plane, where turbulent fluctuations cause the flow to shift between the inlet jet and corner recirculation zone. The vertical RMS velocity fields show a peak in the inner shear layer for similar reasons. Peak RMS values in the non-reacting flow are 6 to 7 m/s, and the RMS values in the central recirculation region are around 1 m/s (Figures 6.3 (a) and (b)). In general, higher mean velocities have led to higher magnitudes of RMS velocity in the inlet jet region. Figures 6.3 (c) and (d) show a broad region of high vertical RMS velocity in the inlet jet of the CH_4 flame, indicating the unsteady nature of the heat release. The unsteady heat release causes intermittent flow acceleration to produce large flow fluctuations. The RMS velocities in the central recirculation zone are higher, between 2-3 m/s, compared to the non-reacting flow. For the H_2-enriched flame, the downward shift of the inlet jet is reflected in the RMS velocity fields. The RMS velocity is highest in the shear layers on either side of the inlet jet because of the vortical structures in these regions. The RMS velocities in the central recirculation region are similar to the CH_4 flame. The broad region of high RMS vertical velocity in the inlet jet region observed for the CH_4 flame is not present. This suggests steady heat release, producing a more robust flame for the H_2-enriched fuel.

Next, the turbulent kinetic energy (TKE) was calculated using Eqn. 4.12 where the out of plane RMS velocity is not considered. Figure 6.4 shows that the TKE is maximum near the inlet jet and minimum in the central recirculation region. These trends are related to the mean and RMS velocity magnitudes in the inlet jet and central recirculation regions. Much of the TKE is confined to the inlet jet region, where the velocity is the highest. In the CH_4 flame, higher levels of TKE in the inlet jet region signify unsteady nature of combustion, an observation also made from RMS velocity plots in Figure 6.3. Higher TKE levels observed in the inlet jet region of the CH_4 flame are not present in the H_2-enriched flame. In the H_2-enriched flame, more stable combustion reduces velocity fluctuations and hence, the TKE. The maximum TKE is about the same for all three cases.

Kinetic energy dissipation rate is a measure of the conversion of the kinetic energy of the flow to internal energy of the fluid by viscous losses at small scales. The 2-D kinetic energy dissipation rate was defined in Eqn. 4.17, and is shown in Figure 6.5. Intense energy dissipation occurs in the inlet jet and corner recirculation zones, where the velocity is high. The kinetic energy dissipation rate field for the CH_4 flame is similar to that of the non-reacting case, because of the similarity in the flow structure. In case of the H_2-enriched flame, the region with high values of kinetic energy dissipation rate has shifted downstream because of the change in the orientation of the inlet jet region.

6.4 2-D Vorticity and normal strain fields

Vorticity and divergence are of importance because they can either help or hinder the combustion at high values. Figure 6.6 shows the vorticity and normal strain calculated from the average velocity fields for the three cases. Positive vorticity is observed in the inner shear layer where the reverse flow turns counterclockwise to join the inlet jet. The region of negative vorticity is associated with the clockwise rotating flow in the corner recirculation zone. For the non-reacting case (Figure 6.6 (a)), peak vorticity magnitudes of about 5000 s^{-1} are observed in the shear layers, while the vorticity magnitudes in the central recirculation region are relatively low. Peak vorticity values in the shear layers of the CH_4 flame (see Figure 6.6 (c)) have increased to 6000 s^{-1} because of higher velocities in the flame. In the case of the H_2-enriched flame, the regions of high vorticity are broader and shifted upwards in conjunction with the shear layers. The peak vorticity values are similar to those for the CH_4 flame.

The averaged normal strain data for the three cases are also shown in Figure 6.6. Normal strain is important because compression promotes combustion whereas expansion may cause flame extinction. Figure 6.6 (b) for the non-reacting case shows that the regions of negative strain or compression are located in the inner shear layer and corner recirculation zone. Positive strain or expansion is observed in the outer shear layer. Normal strain is generally small in the central recirculation region. The peak values for the normal strain are 2000 s^{-1} in compression and 1000 s^{-1} in expansion. Figure 6.6 (d) shows the average normal strain for the CH_4 flame. Although the general features are similar to the

non-reacting case, the magnitudes of normal strain have increased. The peak values are 3000 s^{-1} in compression and 2000 s^{-1} in expansion. The higher extensional strain rate is caused by the volumetric expansion associated with the heat release. Figure 6.6 (f) shows the average normal strain of the H_2-enriched flame. The regions of compression and expansion have shifted upwards in conjunction with the shear layer. The peak values are 4000 s^{-1} in compression and 3000 s^{-1} in expansion. The higher extensional strain indicates more intense volumetric heat release rate for the H_2-enriched flame.

As shown above, the average velocity field does not fully represent the instantaneous flow field with smaller vortical structures. It is therefore important to consider the influence of instantaneous vorticity and normal strain on flame properties in localized regions. Figure 6.7 shows the instantaneous vorticity and normal strain fields corresponding to the velocity fields in the left column of Figure 6.2. The instantaneous vorticity field of the non-reacting flow in Figure 6.7 (a) shows random structures with peak values that are several times higher than the average values in Figure 6.6. The peak vorticity magnitudes occur in the smaller structures absent in the time-averaged field. Instantaneous peak values are about 25,000 s^{-1} compared to peak values of 5000 s^{-1} in the averaged field. Most of the structures with negative vorticity are located in the corner recirculation zone, while the majority of positive vorticity structures occur in the inner shear layer. Figure 6.7 (c) shows that the instantaneous vorticity field of the CH_4 flame is similar to that of the non-reacting flow, with matching peak values. Similar trends are observed for the instantaneous vorticity field of the H_2-enriched

flame in Figure 6.7 (e), although the region containing positive vortical structures has shifted downstream.

The instantaneous normal strain field for the non-reacting case in Figure 6.7 (b) shows several small structures with regions of expansion in the inlet jet, and regions of compression in the shear layers. Similar observations are made from the instantaneous normal strain field for the CH_4 flame in Figure 6.7 (d) and the H_2-enriched flame shown in Figure 6.7 (f). Peak values of the instantaneous normal strain fields are similar for all three cases, 21,000 in expansion and 22,000 in compression. The vorticity and normal strain of the instantaneous velocity fields are significantly different from those of the time-averaged velocity fields. Specifically the peak instantaneous values are several times higher than the peak mean values, and the field contains smaller random structures. The local flame extinction will depend upon the instantaneous strain rates that were 4-7 times greater than the average strain rates, typically used for the analysis.

6.5 Summary of flow field measurements

Average velocity fields showed the expected large scale recirculation zones found in combustors of similar geometry. The average velocity fields for the CH_4 flame had a structure similar to those of the non-reacting case, but higher velocity magnitudes were observed due to the heat release. The average velocity field for the H_2-enriched flame was significantly different from the other two cases indicating that the fuel composition affects the flow field through. The instantaneous velocity fields showed similar recirculation zones, but also contained many small intense vortical structures. The RMS velocity fields

showed that the steady heat release associated with the H_2-enriched flame resulted in lower RMS velocities, presumably due to more steady flow acceleration. The TKE results also showed that the turbulent fluctuations in the CH_4 flame were more pronounced. The Ked results showed that most of the kinetic energy was lost in the high speed inlet jet region for all the cases. The average vorticity and normal strain fields showed that recirculation structures present in the combustor result in strain rates of a few thousand. The instantaneous vorticity and strain fields showed that the peak values were associated with the smaller instantaneous flow structures and were several times the magnitude of the average values. The differences in the flow fields and strain fields when the instantaneous data were used suggest that the instantaneous data should be considered in models. Fuel composition was shown to affect the flow field, as different fuels may burn at different locations in the combustor.

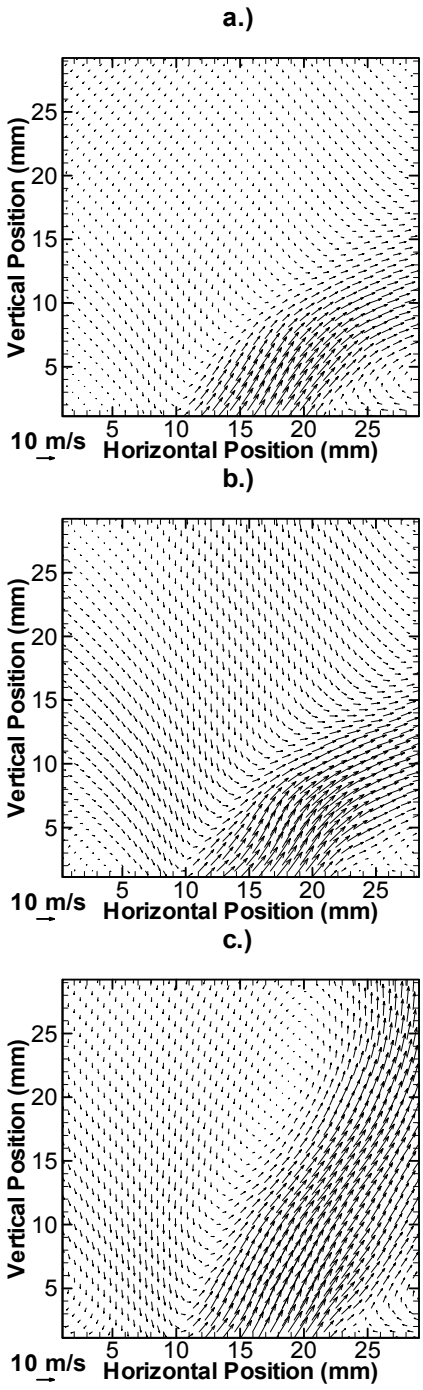

Figure 6.1. Time-averaged velocity data for: a.) Non-reacting case, b.) CH_4 flame, and c.) H_2-enriched flame. Vectors failing the 3 standard deviation outlier test were not averaged, and 25 % of the vectors are shown for clarity. (S = 1.5, V = 10 m/s, and Tad = 1350^0C)

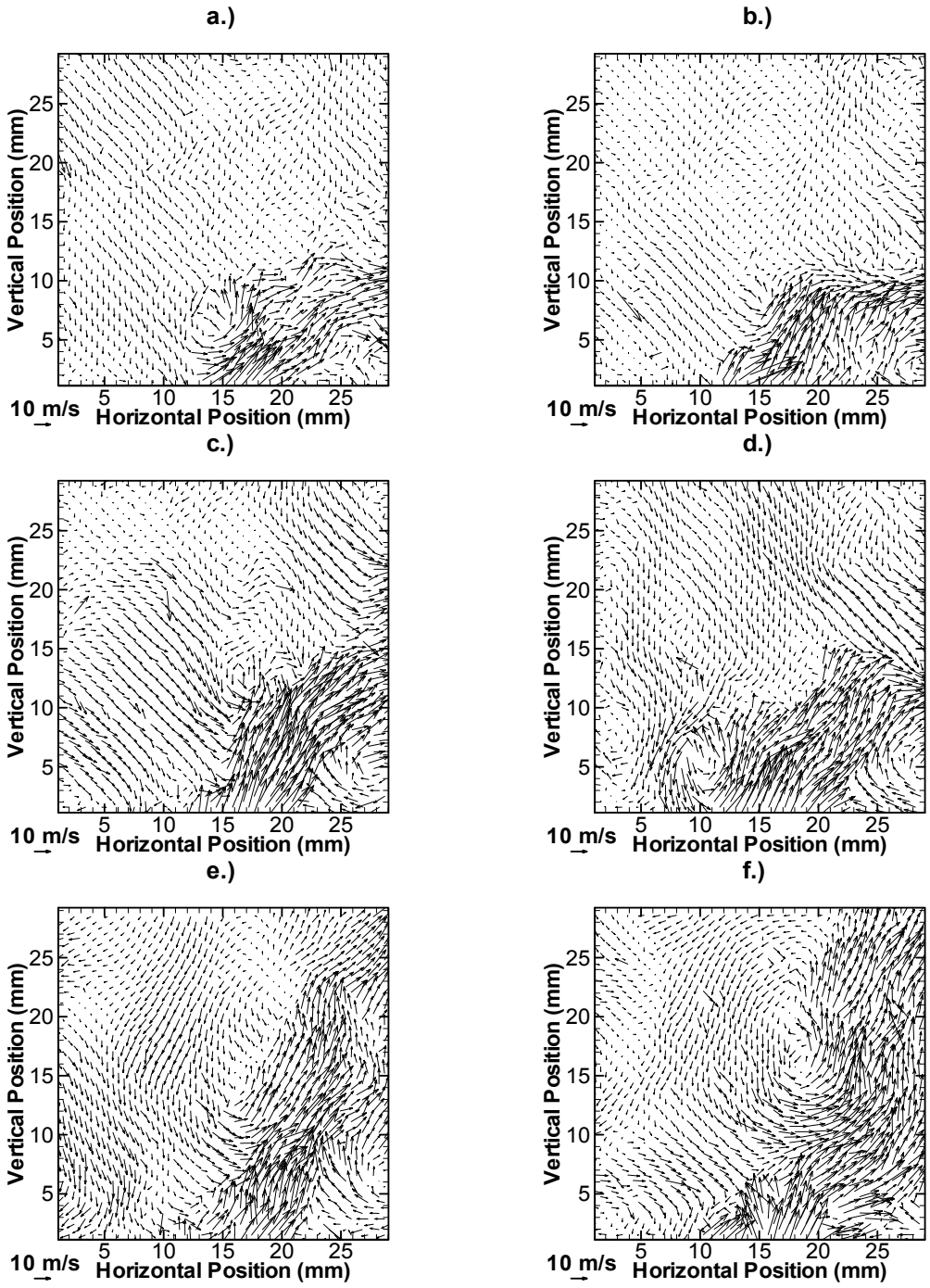

Figure 6.2. Instantaneous velocity fields at random times for: a.), b.) Non-reacting case c.), d.) CH_4 flame, and e.), f.) H_2-enriched flame. Twenty five percent of the vectors are shown for clarity. (S = 1.5, V = 10 m/s, and Tad = 1350^0C)

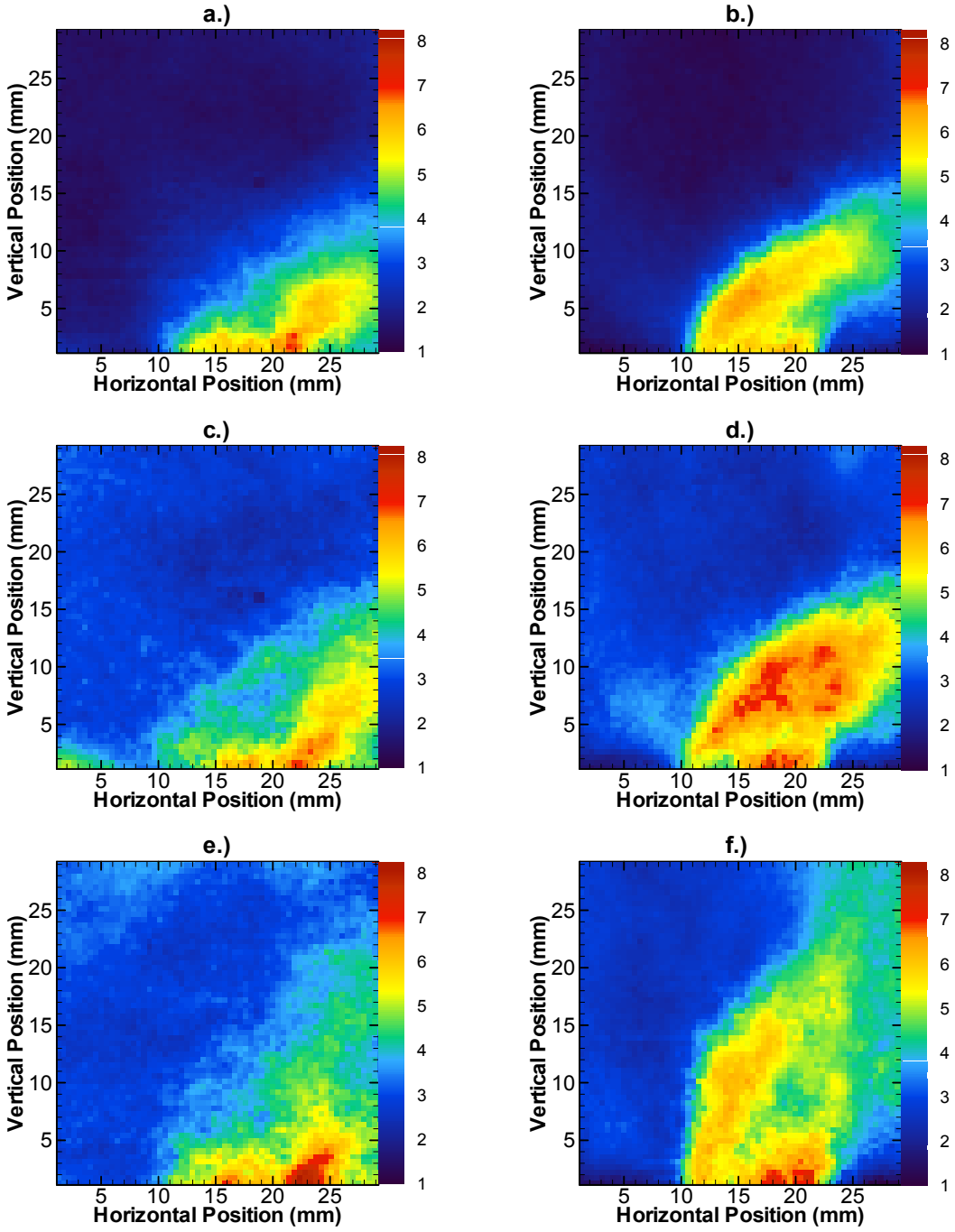

Figure 6.3. Horizontal RMS velocity (left column), and vertical RMS velocity (right column) in units of m/s for: a.), b.) Non-reacting c.), d.) CH_4 flame, and e.), f.) H_2-enriched flame. (S = 1.5, V = 10 m/s, and Tad = 1350^0C)

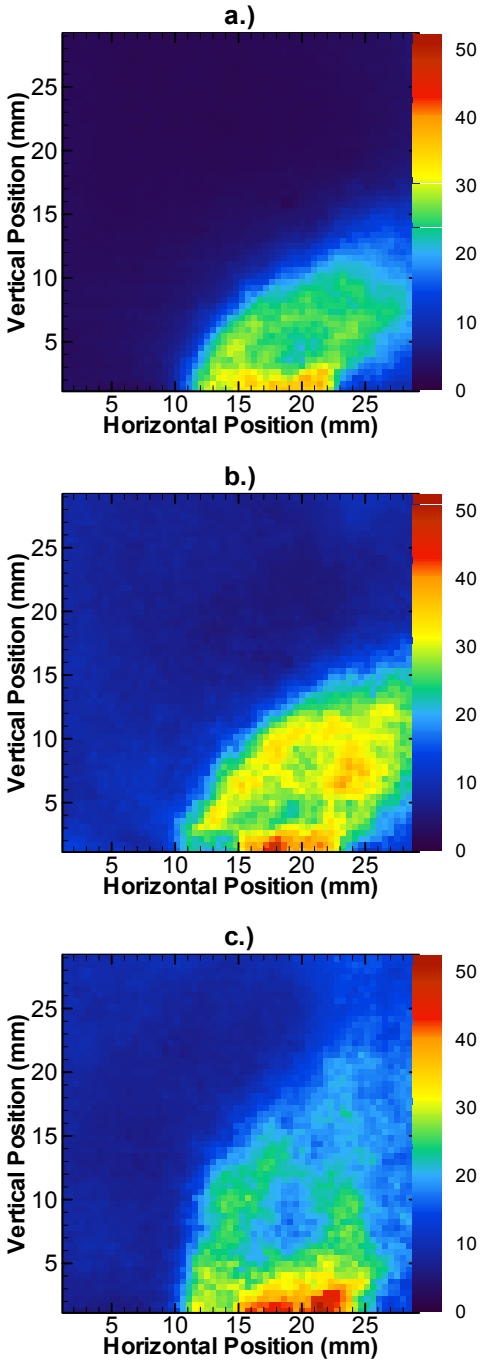

Figure 6.4. Turbulent kinetic energy in units of m^2/s^2 for: a.) Non-reacting case, b.) CH_4 flame, and c.) H_2-enriched flame. (S = 1.5, V = 10 m/s, and Tad = 1350^0C)

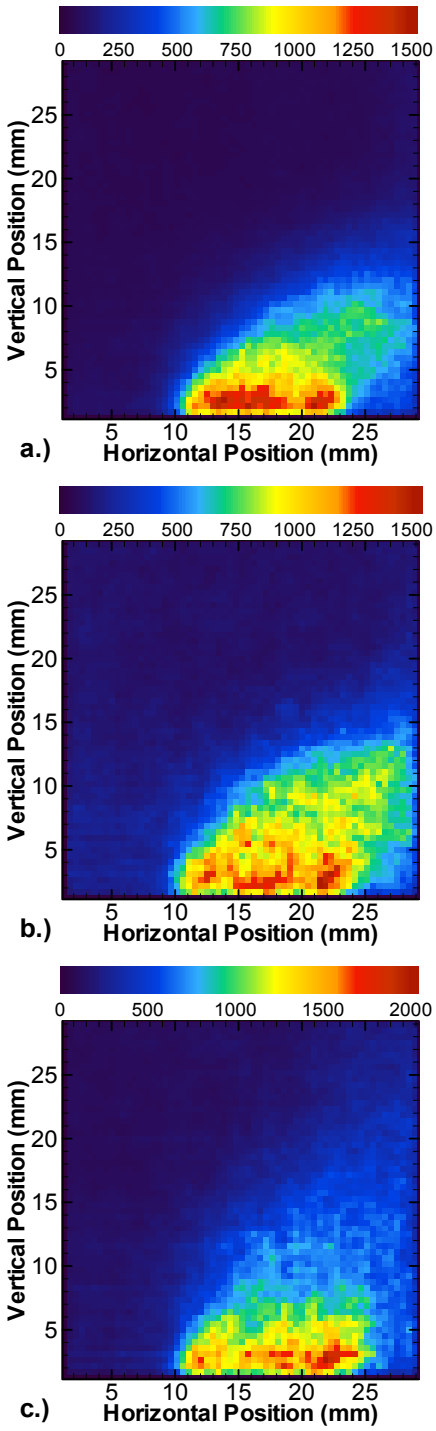

Figure 6.5. Two-dimensional kinetic energy dissipation plots in units of m^2/s^3 for: a.) Non-reacting case, b.) CH_4 flame, and c.) H_2-enriched flame. (S = 1.5, V = 10 m/s, and Tad = 1350^0C)

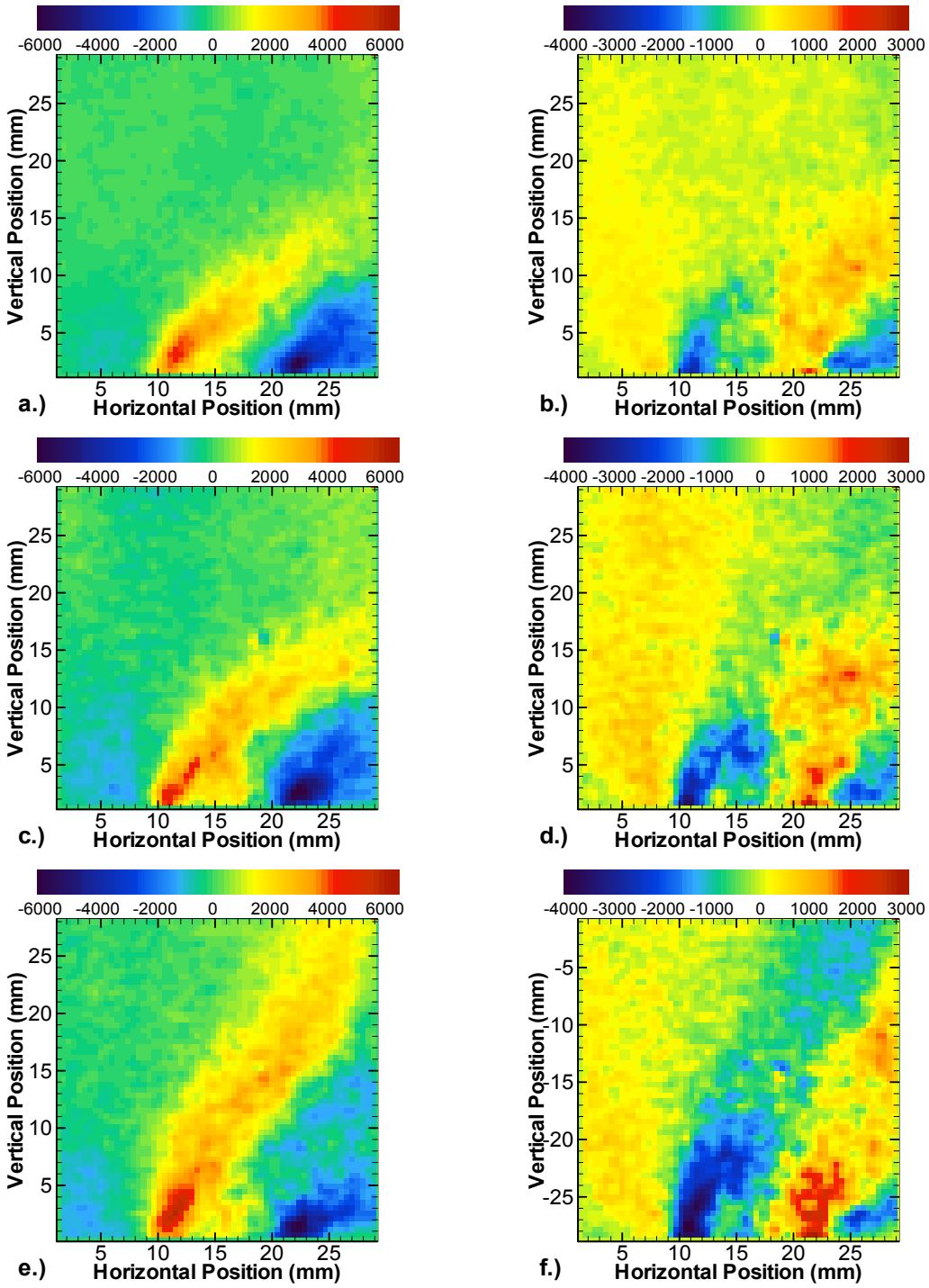

Figure 6.6. Two-dimensional Vorticity (left column) and 2-D normal strain (right column) of the average velocity field in units of 1/s: a.), b.) Non-reacting case, c.), d.) CH_4 flame, and e.), f.) H_2-enriched flame. (S = 1.5, V = 10 m/s, and Tad = 1350^0C)

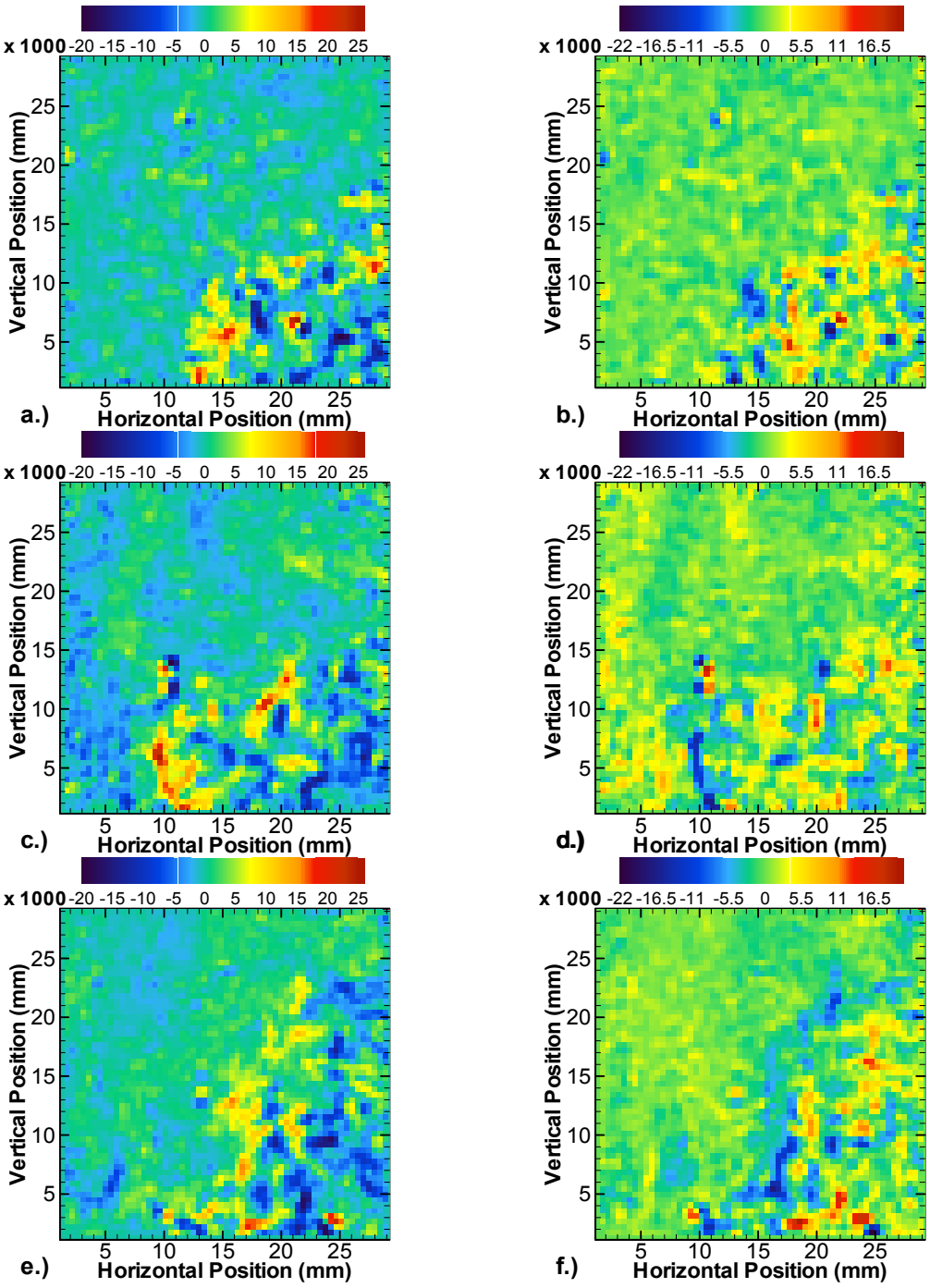

Figure 6.7. Two-dimensional Vorticity (left column) and 2-D normal strain (right column) of the instantaneous velocity fields shown in the left column of Figure 6.2 in units of 1/s: a.), b.) Non-reacting case, c.), d.) CH_4 flame, and e.), f.) H_2-enriched flame. (S = 1.5, V = 10 m/s, and Tad = 1350^0C)

CHAPTER 7: INTERACTION OF THE FLAME AND FLOW FIELD

In this chapter, time-averaged data are presented followed by the simultaneous measurements of velocity and OH in the modified combustor. The fuels utilized are CH_4 and a blend of 60% CH_4 and 40% H_2. The flame temperature was 1350 ^{0}C and the bulk vertical inlet velocity was 10 m/s. The swirl number of the burner was 1.5 and the Reynolds numbers were 13,487 and 13,117 for the CH_4 and H_2 enriched CH_4 flames respectively. The measurements were taken in many separate trials as only 10 data sets could be obtained at a time because of fouling of the quartz combustor by the seed particles. The time-averaged velocity data were computed from a sequence of 200 instantaneous measurements, which were indistinguishable from averages performed with 100 data points. The averaged OH data presented are from a set of 1000 images.

7.1 Time-averaged measurements

An overall understanding of the flame structure in the modified combustor is gained from Figure 7.1 showing time-averaged OH images for CH_4 and H_2-enriched CH_4 flames. The horizontal lines seen in the OH image are due to distortion by the quartz confinement tube. The standard corrections for flat field, background and laser sheet nonuniformity have been made to all the OH images presented in this work. In Figure 7.1, a different color scale is used for each flame. The OH image for the CH_4 flame (Figure 7.1 (a)) shows long and wide reaction zones on either side of the jet axis. Reactions occur mainly up to vertical location, y = 60 mm, although minor quantities of OH persist farther downstream. No OH is found at the intersection of the combustor inlet plane and wall, indicating a lack

of reactions in the corner recirculation zone. In contrast, the time-averaged OH image for the H_2-enriched flame is shorter and more intense, with higher OH levels. The combustion is virtually complete at z = 25 mm. High OH levels in the corner recirculation zone demonstrate intense combustion in that region. The minor asymmetry in Figure 7.1 is attributed, in part, to the differences in velocity profiles at the leading and trailing edges of the inlet swirler vanes.

Although OH data in Figure 7.1 were obtained across the full length of the combustor, simultaneous data were acquired on only one side of the jet axis over the 30mm x 30mm field-of-view of the PIV setup. Figure 7.2 shows the time-averaged OH PLIF data overlaid with velocity vectors for both flames. The flow field can be divided into several major regions. The inlet jet denoted by the high velocity reactant inflow is located at horizontal positions between 10 and 20 mm. The large backflow in the center of the combustor is the centerbody recirculation region. The corner recirculation zone (in the lower right side of the image) is formed at the intersection of the combustion inlet plane and wall. The inner shear layer is located between the centerbody recirculation zone and the inlet jet, and an outer shear layer resides between the inlet jet and the corner recirculation region.

The time-averaged CH_4 flame data in Figure 7.2 (a) show high OH levels in the inner shear layer near the combustor inlet and farther downstream. Combustion is not sustained in the high velocity region of the inlet jet. Hot combustion products in the inner shear layer and centerbody recirculation region are shielded by the inlet jet from reaching into the outer shear layer and the corner recirculation region and hence, no reactions are occurring in these zones. In

contrast, Figure 7.2 (b) shows combustion occurring in the inlet jet region for the H_2-enriched flame. Consequently, the outer shear layer and corner recirculation region also participate in combustion to help produce a shorter flame. Consumption of fuel in the corner recirculation zone and the resulting products mixing with the incoming reactants would also enhance the reaction rates. The reduction in flame length however, may not be entirely due to the added combustion in the recirculation zone. Fuel-composition dependent location of heat release has also affected the global features of the flow field. The inlet jet in the H_2-enriched flame has a higher momentum because of the heat release occurring within it. The increased velocity causes the inlet jet region to align more vertically to a 60^0 angle with respect to the combustor inlet plane. In the CH_4 flame, the non-reacting inlet jet region lacks momentum and hence, the jet tilts towards the wall upon entering the combustor. The OH image in Figure 7.2 (b) does not show correlation with the velocity field at $y > 20$ mm, because there is no reaction zone at downstream locations as shown in the image. The low OH levels at these locations correspond to OH molecules persisting because of the slow third body reactions.

Figure 7.3 shows profiles of the time-averaged vertical velocity, OH, 2-D vorticity, and 2-D normal strain near the combustor inlet plane ($y = 2.5$ mm) for both flames. The vorticity and normal strain were calculated using the path integral method to avoid differentiation errors associated with correlated data in an over-sampled PIV field (Raffel et al., 1984). The uncertainty in the velocity measurements has resulted in an uncertainty in the vorticity and strain fields of 400

s^{-1} (Raffel et al., 1984). Figure 7.3 (a) shows the mean vertical velocity and OH signal for the CH_4 flame. The velocity profile reveals the centerbody recirculation zone in back flow, the inner shear layer where the vertical velocity changes sign, the inlet jet with its high velocities, and the outer shear layer. The peak OH is observed in the inner shear layer, where the flame stabilizes. Figure 7.3 (b) shows vorticity and normal strain profiles at the same vertical location as in Figure 7.3 (a). A positive vorticity peak is observed in the inner shear layer. The peak vorticity location coincides with the location of the negative peak normal strain. The negative normal strain indicates compression of fluid elements in the inner shear layer. Results show that combustion in the CH_4 flame is stabilized in regions of high compressive strain, which agrees with similar observations made by others in non-premixed flames (Rehm and Clemens, 1998), (Han and Mungal, 2003). Figure 7.3 (c) shows the vertical velocity and OH profiles for the H_2-enriched flame. Interestingly, the OH peak has shifted into the high velocity inlet jet region. The ability of the flame to stabilize in the high velocity jet region is attributed to H_2's ability to withstand higher strain before extinction, as compared to CH_4. Furthermore, heat and combustion products from the inlet jet help sustain combustion in the corner recirculation zone for the H_2-enriched flame. Figure 7.3 (d) shows vorticity and normal strain profiles for the H_2-enriched flame. Again, we see a vorticity peak associated with the inner shear layer coinciding with the region of strong compression but not the reaction zone. These results indicate that chemical aspects take precedence over flow aspects in determining the location of heat release in the H_2-enriched flame.

7.2 Time-resolved measurements

Figure 7.4 shows the simultaneous OH and velocity data at four random instants in time for the CH_4 flame. The OH fields show significantly different flame structures, and the velocity fields show many small vortical structures that were not observed in the time-averaged field. In Figure 7.4 (a), the inlet jet region is highly erratic and without combustion. A vortical structure is observed downstream of the inlet jet at horizontal position, $x > 20$ mm and 8 mm $< y < 15$ mm. A thin OH layer curves around the left (inner) side of the vortical structure such that the OH gradient is nearly perpendicular to the flow direction. Figure 7.4 (b) shows a similar vortical structure centered at $x = 20$ mm and $y = 17$ mm. Again, the OH layer is observed to wrap around the left (inner) side of the vortex. These vortical structures may be 2-D projections of 3-D rotating filaments with combustion occurring around them. Evidently, the vortical structures are important to flame stabilization because they provide a source of heat and radicals to the incoming reactant stream. Combustion is observed in the outer edges of these structures where there is mixing between the vortex and its surroundings, but not in the interior where there is no supply of reactants. Figure 7.4 (c) shows a significantly different flow-field and flame structure compared to that at other instants. A very strong backflow with high OH levels is located around $x = 10$ mm and $y = 10$ mm. The backflow is expected to carry combustion products to burn fresh reactants along its path. A large vortex with a surrounding OH layer is observed at the jet center near the combustor inlet. Another feature is the filaments of OH extending downwards along the periphery of the combustor. The

flow field is observed to contain vortical structures around the filaments and small flow velocities within the filament, possibly explaining the stabilization of combustion. Figure 7.4 (d) contains a large vortex at x = 25 mm and y = 20 mm with much of the OH around it. Again, vortices appear to help stabilize combustion in some instances.

Figure 7.5 shows simultaneous OH and velocity data for the H_2-enriched flame. Data are shown only for two instants because flame and flow structures at other instant were similar to one another. The OH field in Figure 7.5 (a) shows many small scale structures with intense combustion, compared to the larger structures observed in the CH_4 flames. The CH_4 flame was closer to extinction and therefore, it could not sustain combustion at small scales without adequate flame stabilization. A small vortex with an OH layer around it is seen near the combustor inlet at x = 10 mm, and at other locations in the combustor. One interesting observation is that the flame also stabilizes in regions without flow recirculation. For example, strong upward flow coinciding with high OH is observed at x = 10 mm and y = 15 mm and x = 25 mm and y = 15 mm. Figure 7.5 (b) contains a large vortical structure at x = 20 mm and y = 20 mm. The right (outer) side of this vortex overlaps a significant portion of the OH region, and the left (inner) side has virtually no OH. This is explained by the combustion occurring upstream in the inlet jet, which provides hot products to sustain combustion on the right side of the vortex. Regions of OH in Figure 7.5 indicate that reactions in the corner recirculation zone and the outer shear layer are assisted by combustion occurring in the inlet jet.

Figure 7.6 shows profiles of instantaneous vertical velocity, OH, 2-D vorticity, and 2-D normal strain at y = 10mm derived from data in Figs. 7.4 (a) and 7.5 (a). Figure 7.6 (a) shows profiles of vertical velocity and OH for the CH_4 flame. The velocity profile shows a large central recirculation region, the inner shear layer, and the inlet jet. A large OH peak is observed in the central recirculation region. Figure 7.6 (b) shows the vorticity and normal strain for the above case. There appears some correlation between vorticity and normal strain, as spikes in vorticity often occur near spikes in normal strain, although the correlation in not perfect. Figures 7.6 (a) and (b) indicate that the peak OH occurs near the location of peak compressive strain, as observed previously from the time-averaged data. Figure 7.6 (c) shows profiles of vertical velocity and OH for the H_2-enriched flame. The location of the peak OH has shifted towards the inlet jet region. An OH peak is also observed in the corner recirculation region. The differences in the location of the reaction zone are explained by enhanced stability of the H_2-enriched fuel. Figure 7.6 (d) shows that the correlation between vorticity and OH level is not observed for the H_2-enriched flame. Likewise, there is lack of correlation between the OH level and normal strain.

7.3 Summary of simultaneous flame and flow field measurements

Time-averaged flow data show that the flow fields and the locations of peak OH are different for the two flames. The H_2-enriched flame is observed to be shorter and more intense, with combustion occurring in the corner recirculation zone. The OH was also found to form in the incoming reactant stream indicating that the flame was stable enough to stabilize there, but the CH_4 flame stabilized in

the shear layer between the centerbody recirculation zone and the inlet jet. The shifting of the location of OH production is important because it suggests that the H_2-enriched flame is less dependent on the flow field properties for stability, then the CH_4 flame which forms near the highest compressive strain. Simultaneous OH and velocity data show that instantaneous OH structures often correspond to the outer edges of small vortical structures. It is believed that these small structures help stabilize combustion by promoting mixing of fresh reactants with burnt products. Burnt products help to stabilize the combustion in two ways, by transferring heat, and by transferring radicals which initiate important reactions.

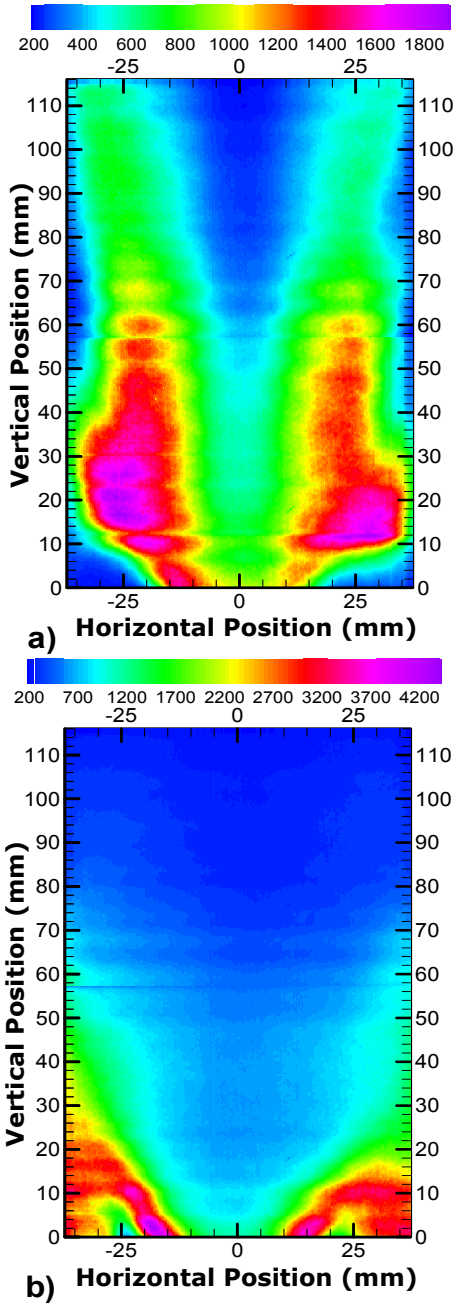

Figure 7.1. Time-averaged OH PLIF image shown at vertical locations with significant OH levels for: a) the CH_4 flame, and b) the H_2-enriched flame. (S = 1.5, V = 10 m/s, and Tad = 1350^0C)

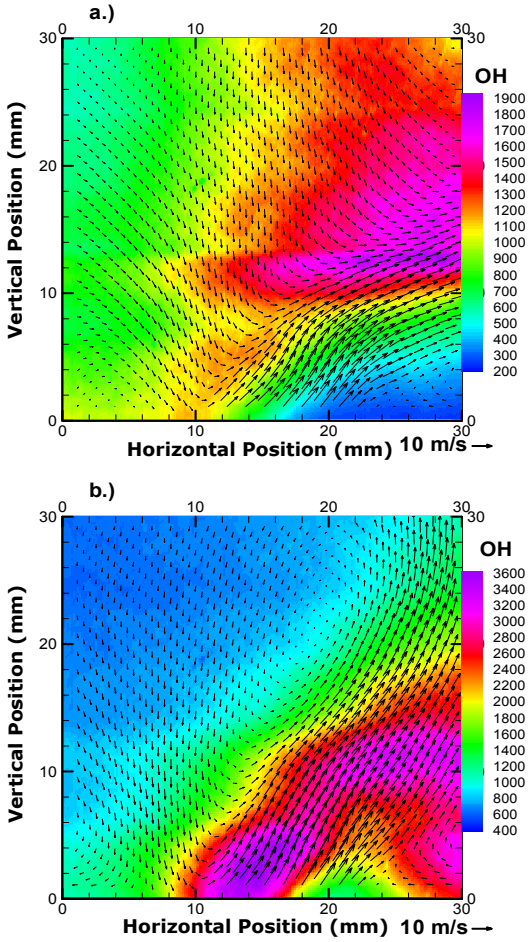

Figure 7.2. Time-averaged OH PLIF (arbitrary units) and velocity data (11% of vectors shown): a.) CH_4 flame, b.) H_2-enriched flame. (S = 1.5, V = 10 m/s, and Tad = 1350^0C)

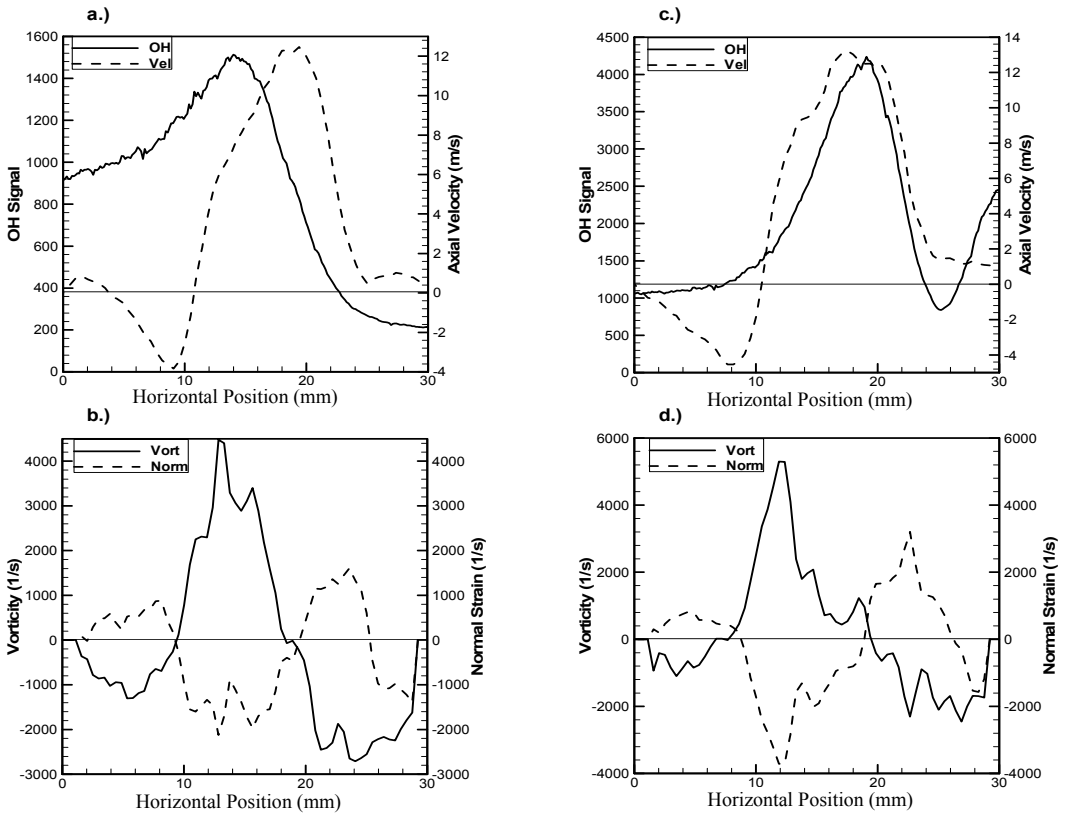

Figure 7.3. Normalized horizontal profiles of time-averaged OH signal, vertical velocity, 2-D vorticity, and 2-D normal strain at a vertical distance of 2.5 mm a) CH_4 flame OH and velocity, b) CH_4 flame 2-D vorticity and 2-D normal strain, c) H_2-enriched flame OH and velocity, and d) H_2-enriched flame 2-D vorticity and 2-D normal strain. (S = 1.5, V = 10 m/s, and Tad = 1350^0C)

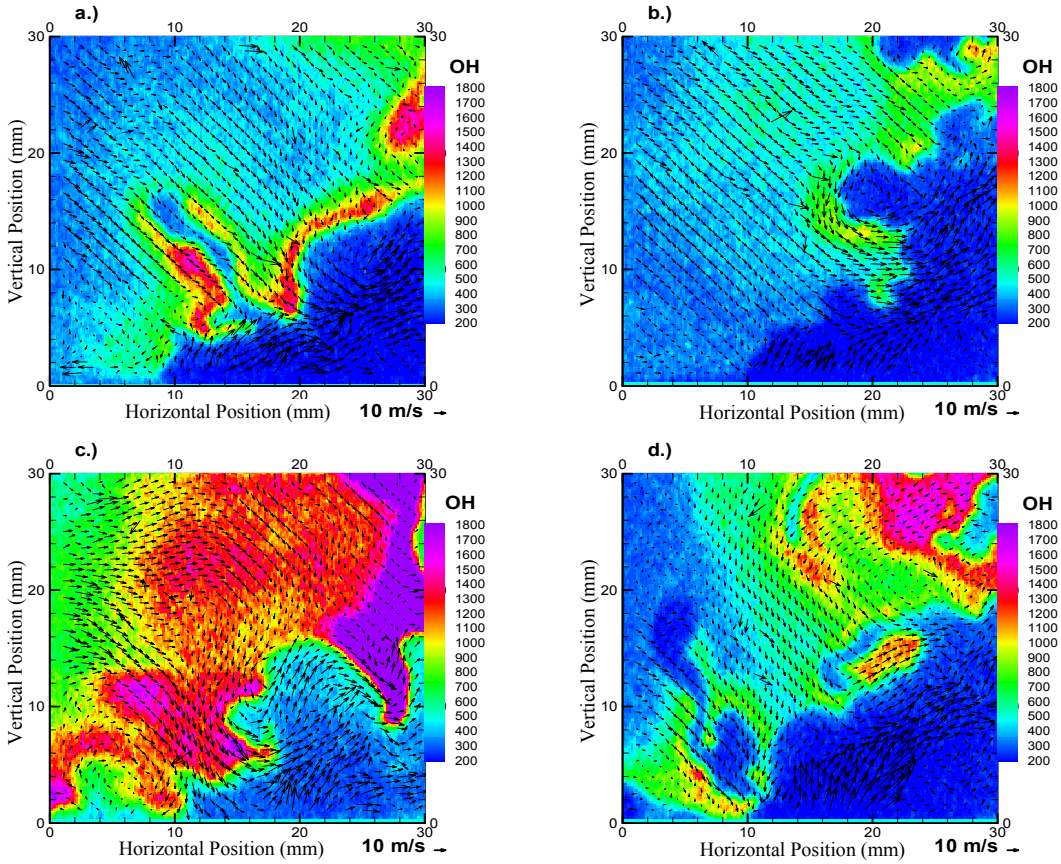

Figure 7.4. Simultaneous OH and velocity measurements at four random instants in time for the CH_4 flame a, b, c, and d. Only 11% of velocity vectors are shown to enhance clarity. (S = 1.5, V = 10 m/s, and Tad = 1350^0C)

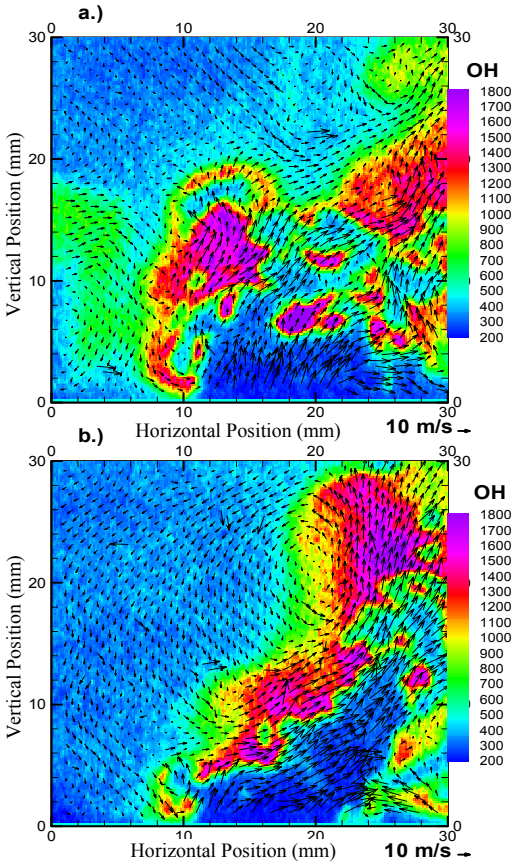

Figure 7.5. Simultaneous OH and velocity measurements at two random instants in time for the H_2-enriched flame a, and b. Only 11% of velocity vectors are shown to enhance clarity. (S = 1.5, V = 10 m/s, and Tad = 1350^0C)

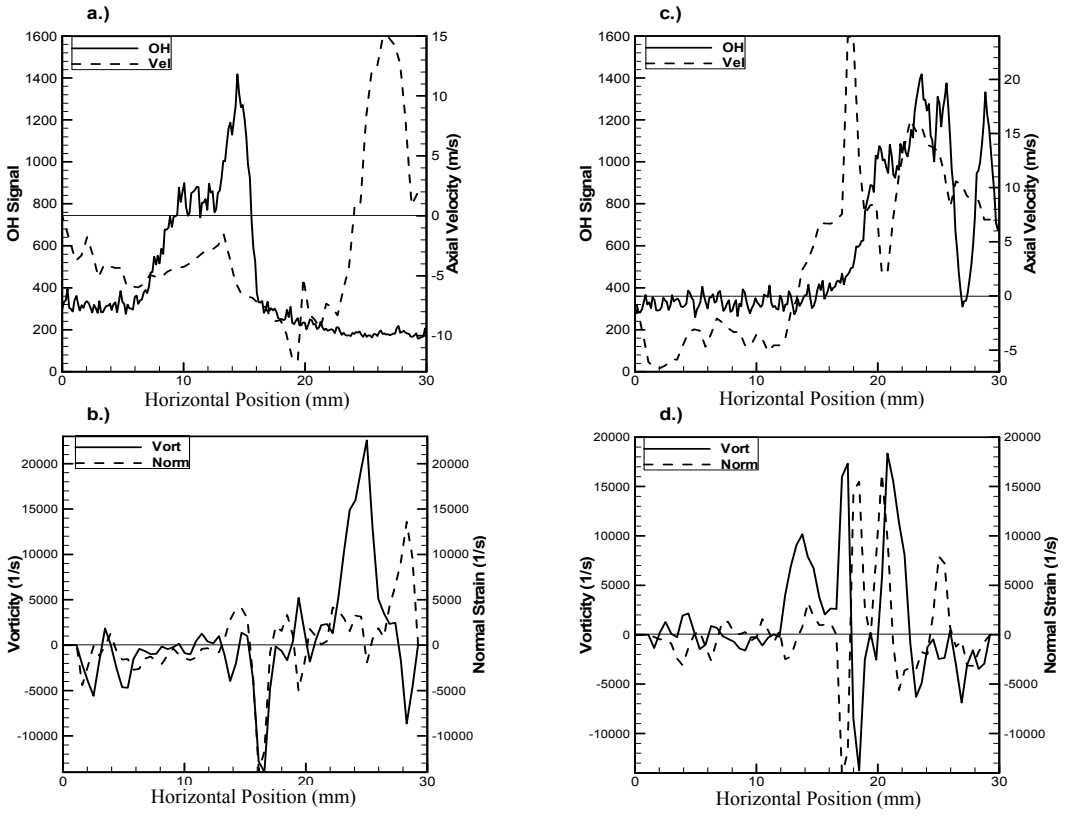

Figure 7.6. Normalized horizontal profiles of simultaneous OH signal, vertical velocity, 2-D vorticity, and 2-D normal strain at a vertical distance of 10 mm a) CH_4 flame OH and velocity, b) CH_4 flame 2-D vorticity and 2-D normal strain, c) H_2-enriched flame OH and velocity, and d) H_2-enriched flame 2-D vorticity and 2-D normal strain. (S = 1.5, V = 10 m/s, and Tad = 1350^0C)

CHAPTER 8: EMISSIONS AND COMBUSTION NOISE MEASUREMENTS

This results and discussion chapter will be divided into two categories. First, flame length and pollutant emissions data will be presented for the modified combustor setup. Second, measurements of combustion noise will be discussed. The sound data is intended to show how variations in the fuel composition will affect the combustion noise. High noise levels are an obstacle to the implementation of many lean premixed systems. These experiments were performed for adiabatic flame temperatures from 1750^{o}C down to LBO in decrements of 50^{o}C. The reactant flow rate was maintained at a constant value for all these experiments, and the swirl number was 1.5. The fuel mixtures utilized in these measurements are CH_4 blended with 10, 20, 30, and 40 % H_2, and C_3H_8 blended with 10, 20, 30, and 40 % H_2.

8.1 Flame Length and Emissions Data:

Figure 8.1 shows the variation of visible flame length with adiabatic flame temperature for various fuels. The flame length was measured by holding a ruler next to the combustor. The measurements were made to the nearest half inch (1.27 cm) to account for the uncertainty in the ruler location and the end of the flame. Figure 8.1 (a) shows the flame length of CH_4 and H_2-enriched CH_4. The flame length at higher temperatures is similar for all three fuels; although it is slightly shorter for the 40% H_2 case. The H_2-enrichment is shown to significantly reduce the flame length at lower flame temperatures near LBO. As the adiabatic flame temperature is decreased, the flame length increases because the cooler

temperatures result in slower reaction rates, and hence, longer reaction zones. The maximum values recorded refer to flames that extended beyond the combustor exit. The decrease in length prior to extinction pertains to a small unstable flame in the center of the combustor which is not completely burning the fuel, but remains lit. Figure 8.1 (b) shows the flame length of C_3H_8 and H_2-enriched C_3H_8 flames. The trends are similar to those observed for the previous case. The LBO temperatures are higher than those observed in the H_2-enriched CH_4 flames. This is caused by the higher LBO temperatures of C_3H_8 as compared to CH_4.

Figure 8.2 shows NOx emissions for all the cases. Figure 8.2 (a) shows the NOx data for the H_2-enriched CH_4 flames. As the flame temperature increases, the NOx level rises exponentially via the thermal NOx mechanism. Measured NOx values range from less than 5 ppm at flame temperatures below 1600 ^{0}C to 20 ppm at higher temperatures. The 100% CH_4 case is observed to have the highest NOx level of the fuels. The data points shown for the lowest temperature correspond to LBO. Addition of H_2 is seen to extend the temperature at LBO significantly. Figure 8.2 (b) shows the NOx emissions for the H_2-enriched C_3H_8 cases. The shapes of the curves are similar; however the maximum NOX levels have increased to nearly 70 ppm as compared to 20 ppm for the CH_4 flame data shown in Figure 8.2 (a). Hydrogen addition has no appreciable effect on NOx emissions in this case. The NOx values at low temperatures are again on the order of 5 ppm. These figures show that adding H_2 to the fuel does not significantly change the NOx emissions at a given temperature, because the NOx

level is largely dependent on the thermal mechanism. The NOx levels do not continue to drop at low flame temperature, possibly because the prompt NOx mechanism is also contributing to the NOx emissions or because of the uncertainty of the analyzer is masking the trend.

Figure 8.3 shows the CO emissions for all of the flames. Figure 8.3 (a) shows the CO emissions of the H_2-enriched CH_4 flames. The CO levels increase with flame temperature because the O_2 concentration in the post-combustion CO burn-off zone is reduced. Although the equilibrium values of CO also rise with temperature, the increase is dominant near the equivalence ratio of unity. Computations revealed that the flames containing C_3H_8 have higher equilibrium values of 400 ppm CO at an equivalence ratio of unity, whereas the CH_4 flames produce 275 ppm of CO at stoichiometric conditions. Therefore, the increase in CO observed in this experiment is a result of incomplete burn-off of the CO in the post combustion zone due to decreasing amounts of O_2 causing CO values well above their equilibrium values of less than 1 ppm over the relevant range of temperatures. The CO levels decrease as the flame temperature is reduced due to the increased amount of O_2, until close to the LBO. Near LBO, the flame burns less steadily and intermittently in local pockets, and the temperature in the CO burn-off zone is reduced, resulting in higher CO emissions due to quenching. The transition from a stable flame to an unstable flame occurs suddenly as evidenced by the steep rise in CO levels near the LBO. The CO concentration of 200 ppm pertains to the upper limit of the gas analyzer, although the actual CO values were much higher, especially prior to LBO. Near the LBO, the flame structure changes

from a stable wide flame to an unstable thin tornado-shaped flame in the center of the combustor. The unstable flame does not burn all of the fuel resulting in poor combustion efficiency and high CO emissions. Figure 8.3 (b) shows the CO emissions for the H_2-enriched C_3H_8 flames. Interestingly, the CO emissions are higher in the H_2-enriched case at high flame temperatures. This is possibly caused by the preferential reaction of O_2 with H_2 as compared to CO. The shapes of the trends are similar to those observed in Figure 8.3 (a), however the CO concentrations begin to rise at lower flame temperatures.

8.2 Combustion Noise Data:

Figure 8.4 shows a power spectral density (PSD) plot of the background noise near the experimental setup caused by the exhaust fan and other equipment. The PSD data are presented in arbitrary units (A.U.). Since all of the data were collected in the same manner the noise data for different cases can be compared. Figure 8.4 shows the ambient noise in the lab was relatively low, with the peak power of 0.25 at a frequency of 750 Hz. The total power of the background noise obtained by integrating the PSD curve was 6.9. The background noise was removed by subtracting the background PSD at each frequency from the measured PSD for the flames.

Figure 8.5 shows the PSD plot at an adiabatic flame temperature of 1750 C for the CH_4 and H_2-enriched CH_4 flames. These figures show two main frequency bands around 450 Hz, and 600 Hz. The frequency bands are close to the musical notes A4 (440 Hz) and D5 (587 Hz) which are separated by a fifth (five steps). There are two types of standing waves that occur in a column of air,

closed ended and open ended waves. The frequency (f) of a close ended oscillation is given below in Eqn. 8.1 (Serway, 1992):

$$f = \frac{k * c}{4 * l}$$
$$k = \{1,3,5,...\} \qquad \text{Eqn. 8.1}$$

where, k is the wave number, c is the speed of sound, and l is the length of the column. The formula for the open ended oscillation frequency is given below in Eqn. 8.2 (Serway, 1992):

$$f = \frac{k * c}{2 * l}$$
$$k = \{1,2,3,...\} \qquad \text{Eqn. 8.2}$$

where, the symbols are the same as Eqn. 8.1. In addition to the two dominant frequencies there are also harmonics of those frequencies which are half or double. Harmonics which double require consecutive wave numbers which suggests an open ended standing wave in the combustor, as opposed to a closed ended standing wave where only even wave numbers are possible. These frequencies are low enough that the length required to produce them includes the premixer section as well as the combustor. The speed of sound in the system is difficult to quantify because the composition and temperature change throughout. For example, the 600 Hz band may be the first harmonic of the system if the speed of sound is 840 m/s (at 1500 ^{0}C) and the estimated length is 0.7 m.

Figure 8.5 (a) shows the PSD data of the CH_4 flame at a flame temperature of 1750 ^{0}C. The majority of the combustion noise occurs in a band around 600 Hz, with minor peaks at 450 Hz and 275 Hz. The peaks are relatively wide,

indicating that they contain a considerable amount of sound energy. To the ear the tone appears muffled, though the noise is loud. The smaller peak at 275 Hz may be a harmonic of the 600 Hz band. Figure 8.5 (b) shows the PSD data for the 10% H_2 flame. There are significant noise levels in both of the major bands; however the peak value occurs in the band at 600 Hz. This PSD plot looks similar to that for the 100% CH_4 flame, which is reasonable because the fuel compositions are similar. Figure 8.5 (c) shows the PSD data for the 20% H_2 flame. The peak value has shifted to the 450 Hz band, although the 600 Hz band still contains significant power. This shift in frequency at peak power may be attributed to the combustion occurring in different regions of the flame for fuels with and without H_2 (Chapter 7), which may drive different frequencies in various regions of the combustor. Figure 8.5 (d) shows PSD data for the 30% H_2 flame which indicates a dominant peak at 450 Hz. Figure 8.5 (e) shows the PSD data for the 40% H_2 flame. The noise-spectra show the power confined to a narrow band at 450 Hz, which contains a large amount of energy (60 A.U). A very loud noise with an audibly clearer tone was produced. The absence of the 600 Hz frequency may have allowed high noise intensity to develop in the 450 Hz range, because destructive non-harmonic wave forms were not interfering with the oscillation. Another hypothesis is that the combustor was switching between the two modes of oscillation randomly with time. In this case the 450 Hz oscillation did not experience the interference of the 600 Hz wave and was significantly amplified. Fourier transformed data, such as in Figure 8.5, surrenders all time history to gain knowledge of the frequency domain. Whatever the cause, such

strong organized bands of noise can severely damage a combustor operating at high-pressure by cycling the material to fatigue failure, and must therefore be avoided.

Figure 8.6 shows the PSD for the C_3H_8 and H_2-enriched C_3H_8 flames at an adiabatic flame temperature of 1750 ^{0}C. Figure 8.6 (a) shows the PSD for the 100% C_3H_8 flame. The 600 Hz band is dominant over the 450 Hz band, and is a harmonic of a band around 300 Hz. Unlike the previous experiment a frequency of 370 Hz is observed with significant power. Figure 8.6 (b) shows the PSD data for the 90% C_3H_8 and 10% H_2 flame. The 600 Hz band has significantly increased in magnitude by a factor of three, while the 450 Hz band remains relatively unchanged in magnitude. Again there is a harmonic of the 600 Hz band around 300 Hz. Figure 7c shows the PSD for the 20% H_2-enriched C_3H_8 flame. Interestingly the 450 Hz band is shown to increase in power, while the 600 Hz band is decreasing in power due to the interference with the 450 Hz band. The large peak at 280 Hz seems to be a harmonic of the peak at 560Hz which gives the 600 Hz band 2 distinct peaks. Figures 8.6 (d) and 8.6 (e) show the PSD data for the 30% and 40% H_2-enriched C_3H_8 flames. The 450 Hz band is again observed to increase in magnitude. The peak noise level is noticeably increased in Figure 8.6 (e) over the previous C_3H_8 cases. This trend of the 450 Hz band increasing in magnitude with the addition of H_2 to the fuel was also observed in Figure 8.5. It appears that at 1750 ^{0}C fuels containing less H_2 produce oscillations in the 600 Hz band and fuels containing larger quantities of H_2 cause stronger

oscillations in the 450 Hz band, or spend more time oscillating in the 450 Hz mode.

Figure 8.7 shows PSD data for the H_2-enriched CH_4 flames at an adiabatic flame temperature of 1550 ^{0}C. The PSD data of the 100% CH_4 flame in Figure 8.7 (a) show power peaks in both the 450 Hz and 600 Hz bands. The highest power occurs in the 450 Hz band, but the 600 Hz band contains a significant amount of total energy because of the width of its peaks. Figure 8.7 (b) and 8.7 (c) show the PSD data for the 10% and 20% H_2 flames, respectively. In both flames, there is a strong peak in the 450 Hz band which is roughly double of that found in the 100% CH_4 flame, but the 600 Hz band remains unchanged. Figure 8.7 (d) is unique in that it has 3 major peaks due to the inclusion of a peak at 275 Hz and its harmonics at 550 and 825 Hz. As a consequence of having three peaks, the maximum power level is significantly below that of either the 20% H_2 or 40% H_2 cases due to interference. Figure 8.7 (e) shows the PSD data for the 40% H_2 flame. The highest peak is in the 450 Hz band, but there are also peaks at 600 and 275 Hz. Overall, the power level in all the flames is significantly reduced by up to a factor of 10.

Figure 8.8 shows the PSD data for the H_2-enriched C_3H_8 flames at an adiabatic flame temperature of 1550 ^{0}C. As with the H_2-enriched CH_4 flames the overall noise levels are decreased at lower flame temperatures. Figure 8.8 (a) shows the PSD data for the 100% C_3H_8 flame. The 450 Hz mode is dominant, with the 600 Hz band having one fourth the peak power. The 370 Hz band observed in Figure 8.6 (a) is still present, but at reduced power. Figure 8.8 (b)

shows the PSD data for the C_3H_8 flame enriched with 10% H_2. The 600 Hz band has increased in power, overtaking the 450 Hz band as the dominant mode by a small margin. Interestingly, the 600 Hz band also appears to be split into several peaks. There is a peak at 280 Hz with a harmonic at 560 Hz, and the peak at 440 Hz has a harmonic at 880 Hz. These doubling harmonics suggest that the wave forms are open-ended as opposed to close-ended. Figure 8.8 (c) shows the PSD data for the 20% H_2-enriched flame. The 600 Hz band's peak occurs at 580 Hz, and is of equal magnitude with the 450 Hz mode. There appears to be a peak around 220 Hz which is harmonic of the 450 Hz band. Figure 8.8 (d) shows the PSD data for the 30% H_2-enrichment case. The 450 Hz band is dominant; however both the 450 Hz and 600 Hz bands have increased in magnitude. The peak at 225 Hz is more symmetrically formed, and may be driving the oscillation at 450 Hz. The 600 Hz band has split into two peaks, and therefore may not be interfering with the 450 Hz peak as much. Figure 8.8 (e) shows the PSD for the 40% H_2-enriched flame. The 600 Hz band is the same magnitude as in the previous figure; however the 450 Hz mode's peak power has decreased by a factor of two. The decrease in the 450 Hz mode may be due to the shifting of the lower frequency harmonic to 250 Hz, which shows a harmonic at 500 Hz.

Figure 8.9 shows the PSD data for the CH_4 and H_2-enriched CH_4 flames at an adiabatic flame temperature of 1350 ^{0}C. Overall, peak levels have been reduced to the magnitude of the background noise level. The peaks at 450 Hz and 600 Hz are no longer dominant. Higher frequency peaks in the range of 700 to 825 Hz are observed, which are harmonics of other frequencies observed.

Figure 8.10 shows the PSD data for the H_2-enriched C_3H_8 flame at an adiabatic flame temperature of 1350 ^{0}C. Figure 8.10 (a) shows that the PSD data for the 100% C_3H_8 flame contains one significant peak around 1000 Hz and minimal peaks elsewhere. Figures 8.10 (b) through 8.10 (e) show some common trends. The 800 Hz band power decreases with H_2 addition. The 600 Hz band power increases moderately, and 450 Hz band increases significantly with the addition of H_2. The overall noise level also increases as more H_2 is added to the fuel.

Figure 8.11 contains noise data compiled over a range of temperatures for the various H_2-enriched CH_4 and C_3H_8 fuels. Figure 8.11 (a) shows the total power in the 0-1000 Hz range for the H_2-enriched CH_4 flames as a function of flame temperature. As noted earlier, the noise levels in this combustor are very low near the LBO limit for all fuels. For all cases, the noise level increased exponentially as the flame temperature increased. The 40% H_2 flame was observed to have noticeably higher total power levels at high temperatures. In this case, a single dominant frequency was amplified, which reduced the destructive interference. The total power was similar for the remaining fuels over the range of measured flame temperatures. Figure 8.11 (b) shows the total power for the H_2-enriched C_3H_8 flames over the range of temperatures. The noise level was again shown to increase exponentially with temperature. The total power levels recorded are lower than those found in the H_2-enriched CH_4 flames shown in Figure 8.11 (a).

Figure 8.11 (c) shows the power level at the highest peak on the PSD curves for the CH_4 flames. The difference between the 40% H_2 flame and the other flames is significant. The two highest power values for the 40% H_2 flame are off the scale, the highest being 66 A.U. The maximum power level for other fuels is similar. The key difference is that the 40% H_2 flame is driving one frequency to very high amplitude. Figure 8.11 (d) shows the maximum power as a function of temperature for the C_3H_8 flames. The addition of H_2 to C_3H_8 is shown to increase peak noise power, however, not to the extent observed in the CH_4 flames.

Figure 8.11 (e) shows the frequency at which the maximum power occurs for each CH_4 flame. Two dominant bands around 450 Hz and 600 Hz are observed at high flame temperatures. As the temperature decreases, the dominant frequencies changes to 780 Hz and 1000 Hz. These higher frequencies have very low amplitudes, and may be flow related as opposed to combustion related, or they might relate to the non-longitudinal modes of oscillation. It is also not clear at this time if the 1000 Hz mode is real, because it is also the Nyquist frequency. Figure 8.11 (f) shows the frequency at which the peak power occurs for the C_3H_8 flames. At higher temperatures the 450 and 600 Hz modes are dominant, but at lower temperatures the peak values shift to 1000 Hz and a couple points at 800 Hz similar to the H_2-enriched CH_4 flames.

Figure 8.12 (a) shows the percentage of total power contained in the low frequency oscillations from 0-100 Hz as a function of temperature for the CH_4 flames. In some combustion systems the low frequency noise has been shown to

correlate with the LBO and has been proposed as a marker for the imminent LBO. For all the blends of fuels, the low-frequency noise increased near LBO, but not to the extent shown by Nair and Lieuwen (2003). The relative increase in power from 1% to 10% as LBO is approached represents a decrease in the power at higher frequencies rather than an increase in the power at the lower frequencies. For the 40% H_2-enriched flame, the low-frequency noise reached a peak and decreased before LBO, possibly due to the difference in flame shape associated with the unstable flame. It is also possible that the level of premixedness of the air and fuel may play a role in the low frequency noise near extinction due to local extinction and re-ignition phenomena. The thorough mixing provided by the premixer used in this experiment should prevent the low frequency noise near LBO. Figure 8.12 (b) shows a similar trend of an increasing percentage of the total power contained in frequencies less than 100 Hz increasing to about 10% at flame temperatures near LBO in the C_3H_8 flames. Again this increase is attributed to the reduction in amplitude at the higher frequencies.

8.3 Summary of emissions and combustor noise measurements

Flame length increased as the flame temperature decreased due to the reduced kinetic rates. The addition of H_2 shortened the flames at lower flame temperatures, but had little effect at the higher flame temperatures. The NOx emissions increased exponentially with increasing flame temperature as expected for thermal NOx production. The CO emissions increased exponentially with increasing flame temperature, because of the reduced amounts of O_2 in the CO burn off zone. A sudden increase in the CO levels prior to LBO was attributed to

local regions of incomplete combustion in the unsteady flame. Noise levels for the combustor scaled with temperature as well. Two major frequency bands dominated the spectra, one at 450 Hz, and one at 600 Hz. The H2-enriched fuels frequently had peak noise levels in the 450 Hz band.

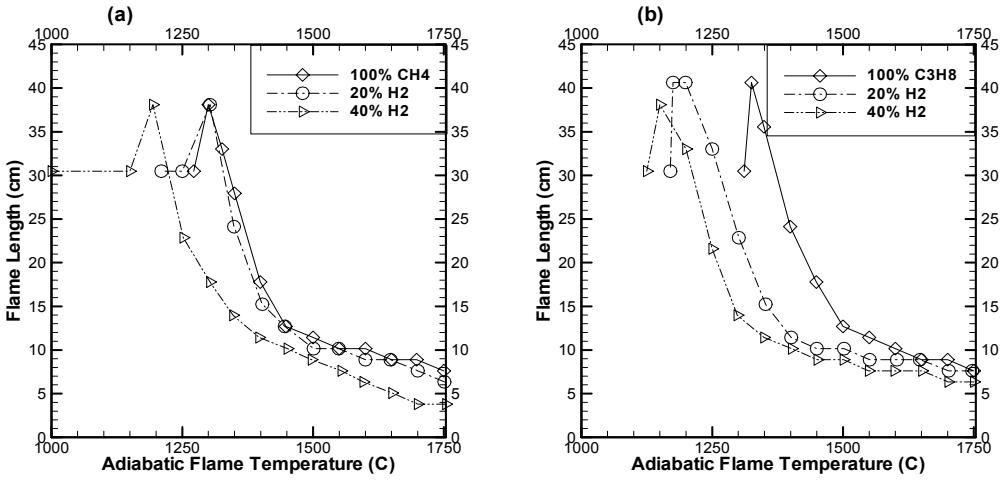

Figure 8.1. Flame length as a function of adiabatic flame temperature for: a) H_2-enriched CH_4 flames, and b) H_2-enriched C_3H_8 flames.

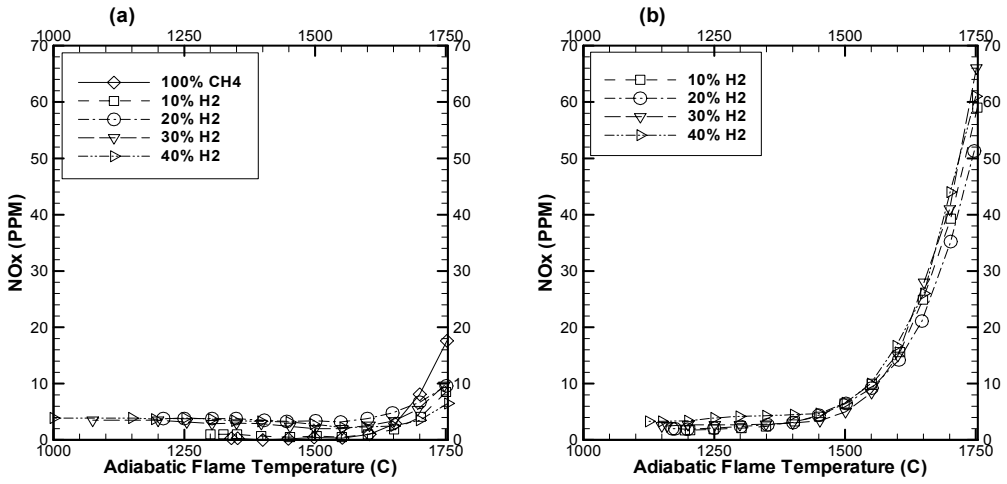

Figure 8.2. Emissions of NOx at different flame temperatures for: a) H_2-enriched CH_4 flames, and b) H_2-enriched C_3H_8 flames.

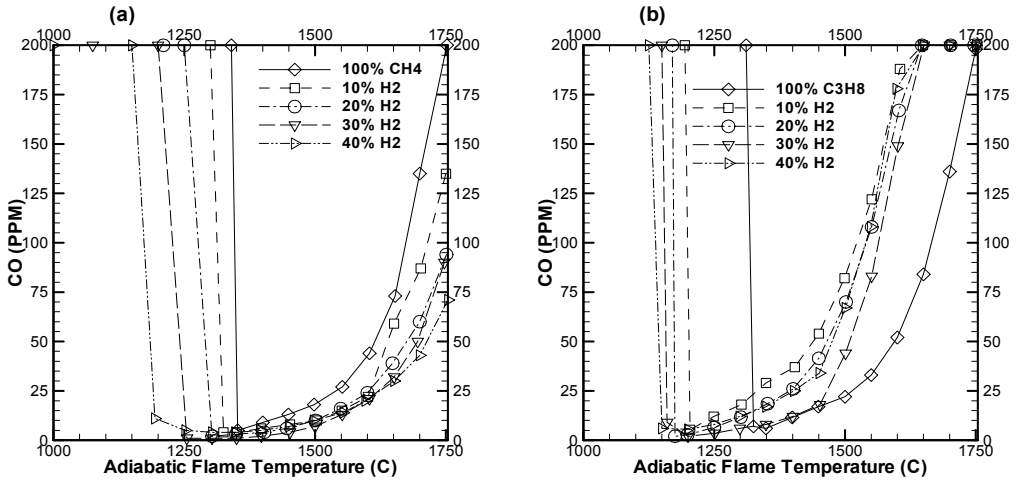

Figure 8.3. Emissions of CO at different flame temperatures for: a) H_2-enriched CH_4 flames, and b) H_2-enriched C_3H_8 flames.

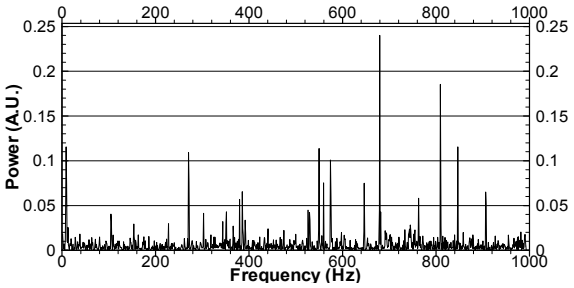

Figure 8.4. Power spectral density plot of the background noise.

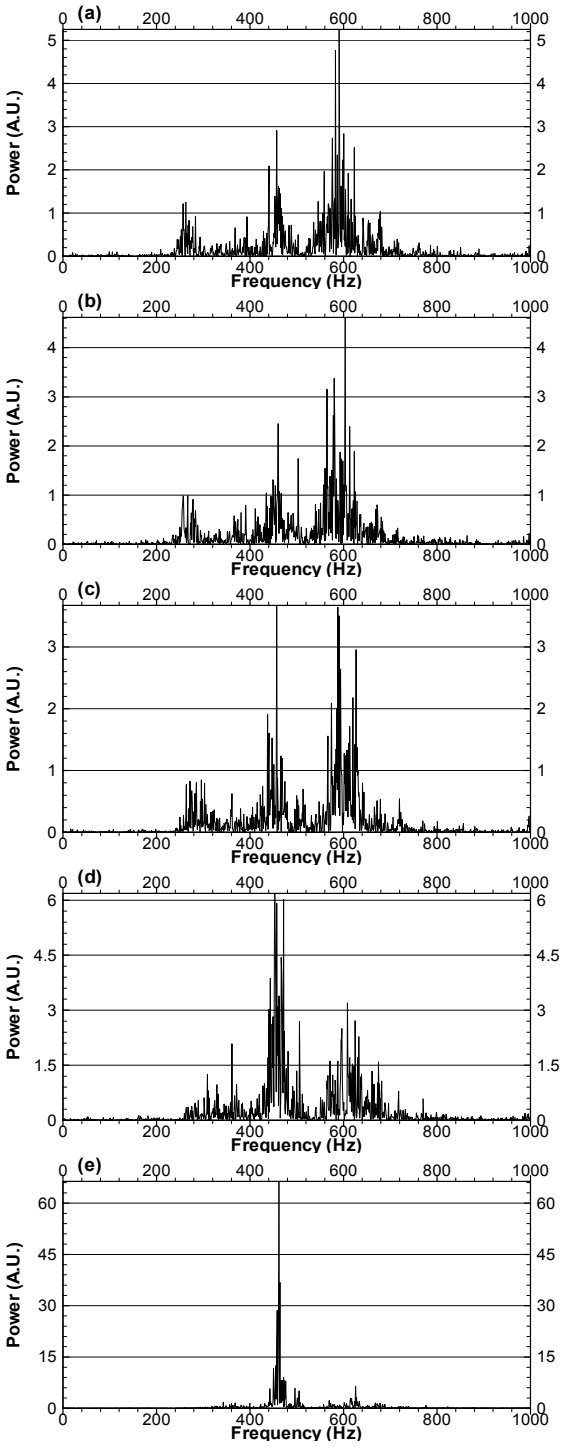

Figure 8.5. Power spectral density plots for H_2-enriched CH_4 fuels at an adiabatic flame temperature of 1750 C for: a) 100% CH_4 flame, b) 90% CH_4 + 10% H_2, c) 80% CH_4 + 20% H_2, d) 70% CH_4 + 30% H_2, and e) 60% CH_4 + 40% H_2.

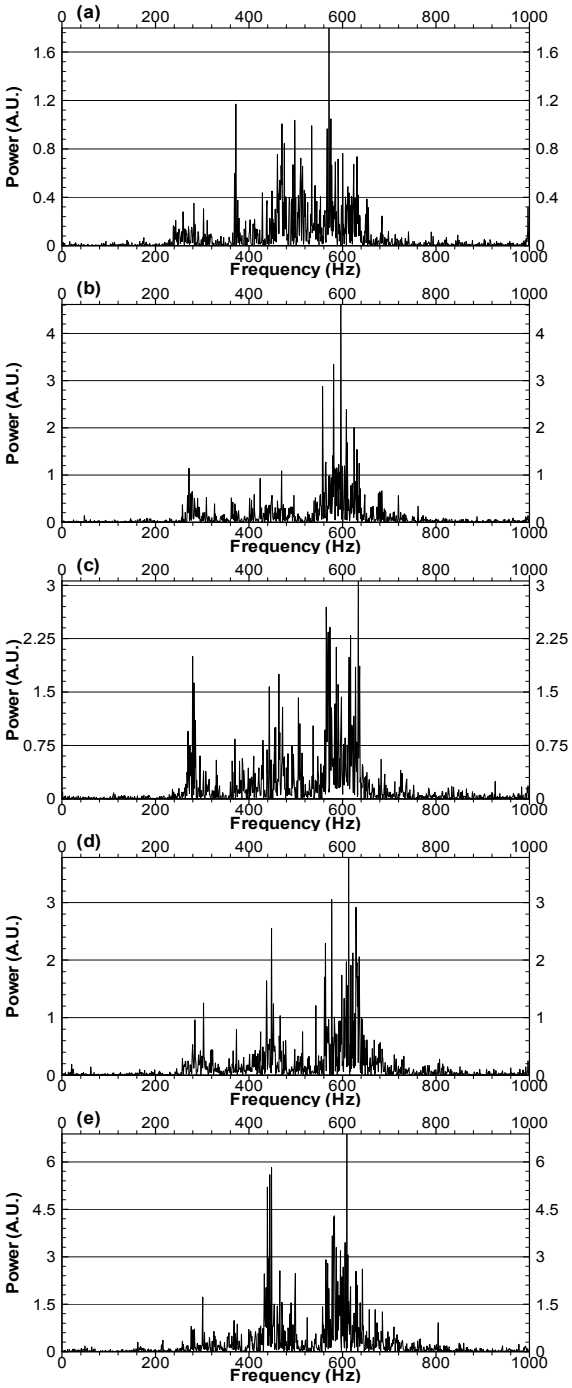

Figure 8.6. Power spectral density plots for H_2-enriched C_3H_8 fuels at an adiabatic flame temperature of 1750 C for: a) 100% C_3H_8 flame, b) 90% C_3H_8 + 10% H_2, c) 80% C_3H_8 + 20% H_2, d) 70% C_3H_8 + 30% H_2, and e) 60% C_3H_8 + 40% H_2.

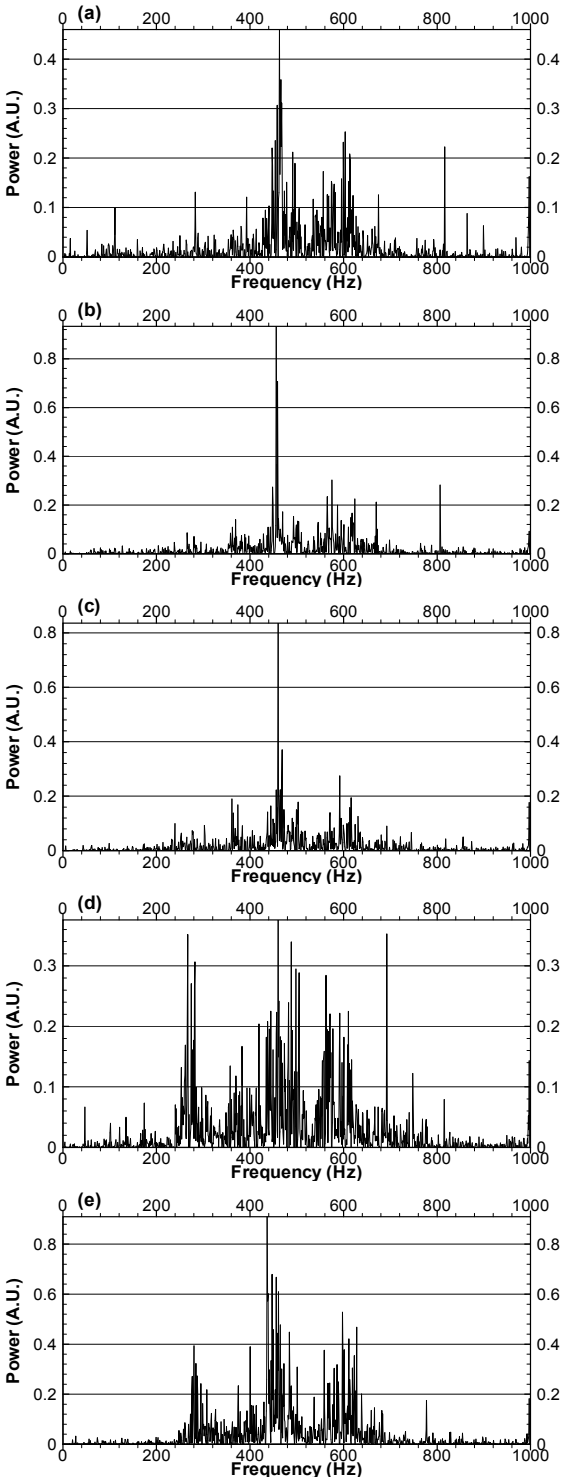

Figure 8.7. Power spectral density plots for H_2-enriched CH_4 fuels at an adiabatic flame temperature of 1550 C for: a) 100% CH_4 flame, b) 90% CH_4 + 10% H_2, c) 80% CH_4 + 20% H_2, d) 70% CH_4 + 30% H_2, and e) 60% CH_4 + 40% H_2.

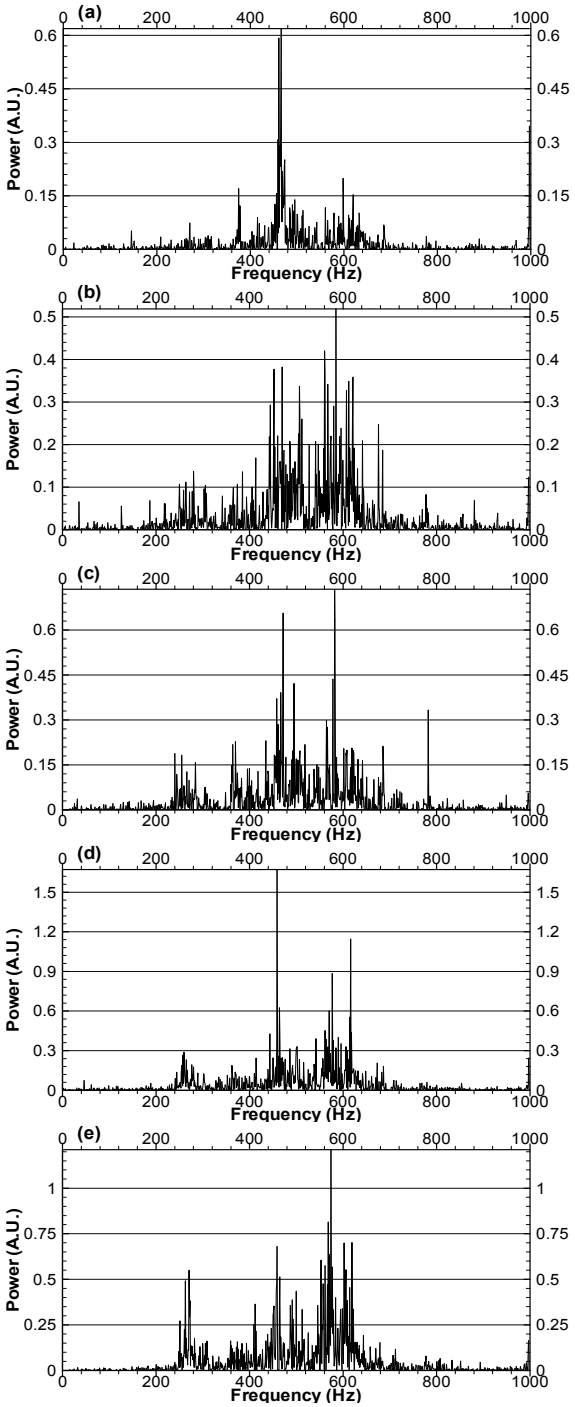

Figure 8.8. Power spectral density plots for H_2-enriched C_3H_8 fuels at an adiabatic flame temperature of 1550 C for: a) 100% C_3H_8 flame, b) 90% C_3H_8 + 10% H_2, c) 80% C_3H_8 + 20% H_2, d) 70% C_3H_8 + 30% H_2, and e) 60% C_3H_8 + 40% H_2.

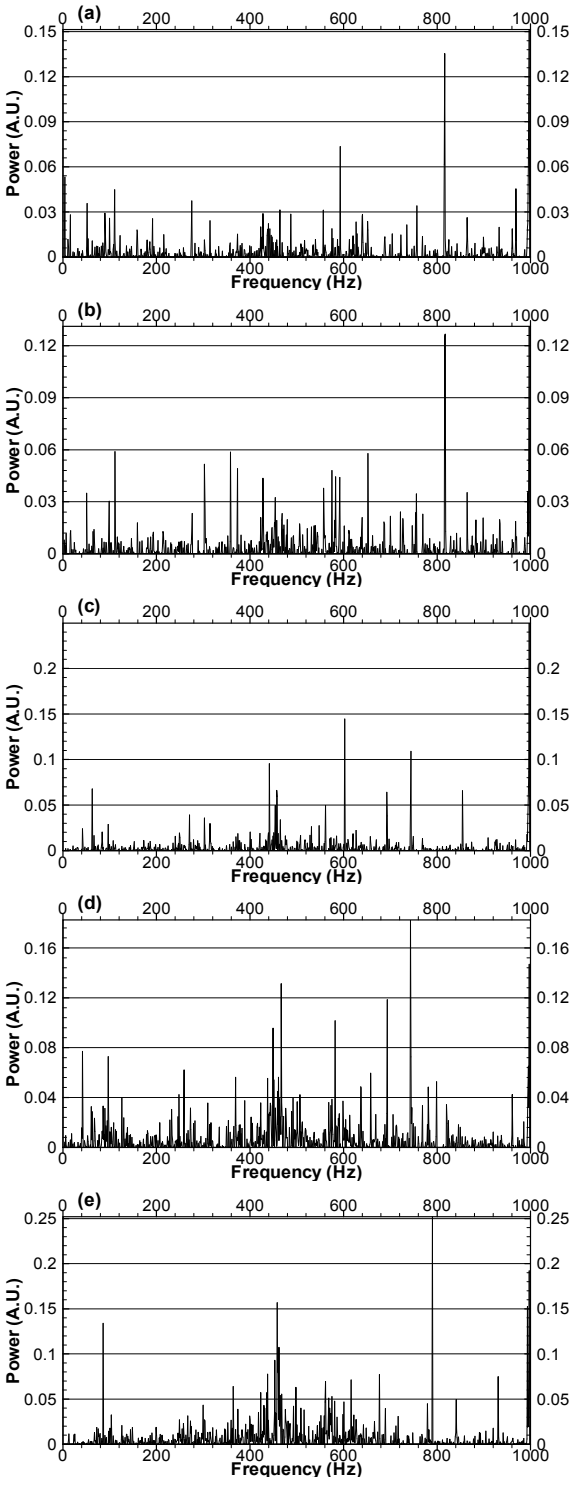

Figure 8.9. Power spectral density plots for H_2-enriched CH_4 fuels at an adiabatic flame temperature of 1350 C for: a) 100% CH_4 flame, b) 90% CH_4 + 10% H_2, c) 80% CH_4 + 20% H_2, d) 70% CH_4 + 30% H_2, and e) 60% CH_4 + 40% H_2.

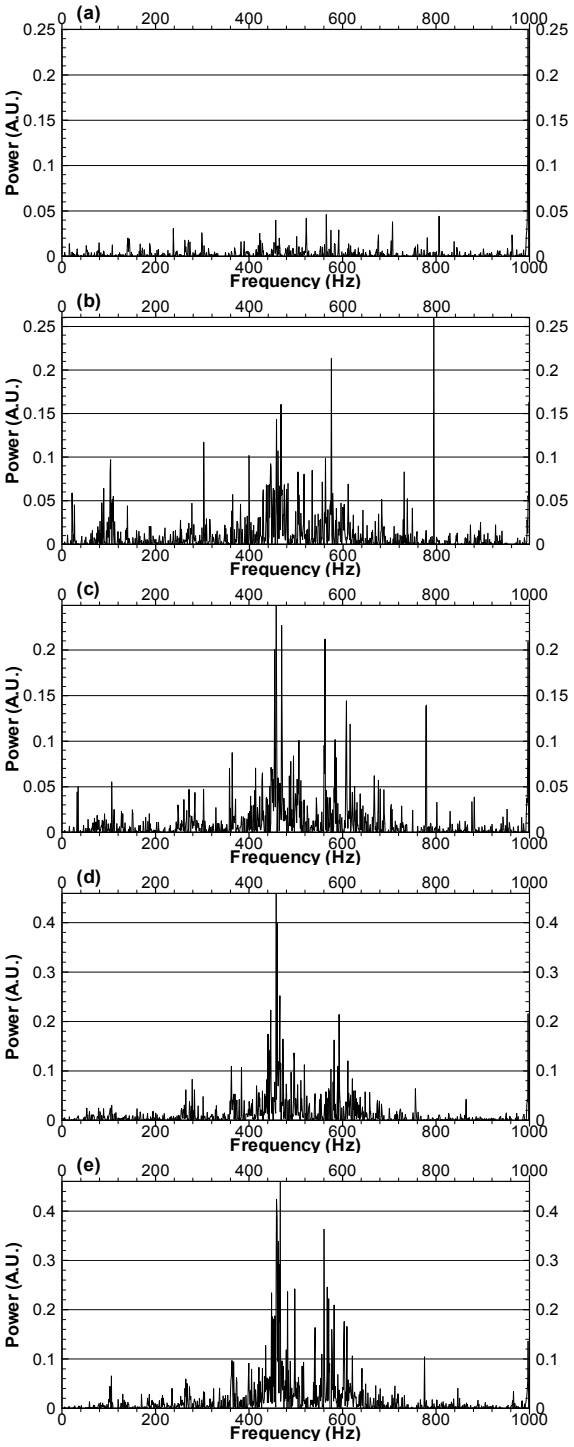

Figure 8.10. Power spectral density plots for H_2-enriched C_3H_8 fuels at an adiabatic flame temperature of 1350 C for: a) 100% C_3H_8 flame, b) 90% C_3H_8 + 10% H_2, c) 80% C_3H_8 + 20% H_2, d) 70% C_3H_8 + 30% H_2, and e) 60% C_3H_8 + 40% H_2.

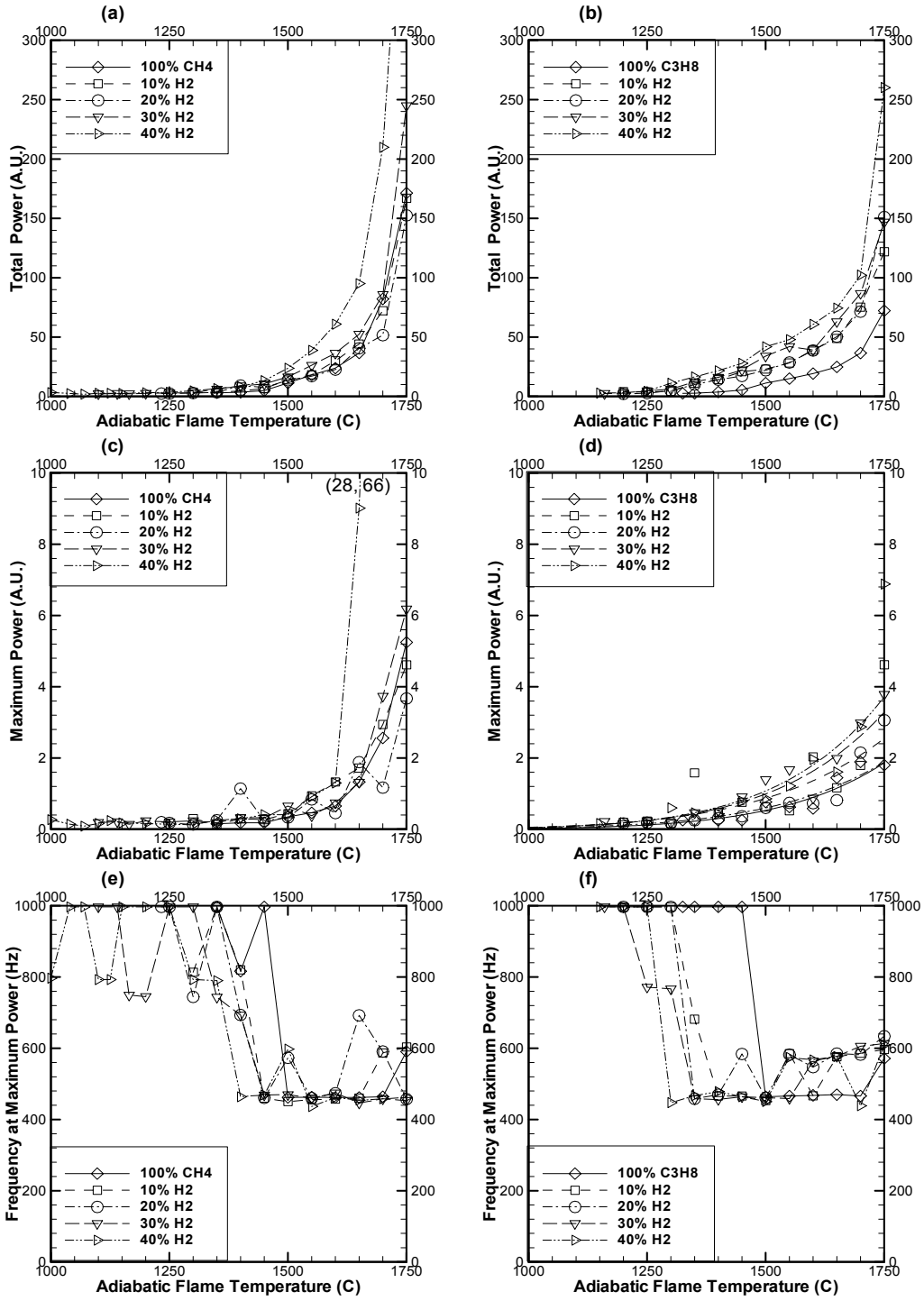

Figure 8.11. Various noise properties for the flames (CH_4, left column, C_3H_8, right column): a), b) total power, c), d) peak power level at a frequency, and e), f) Frequency at which the peak power occurred.

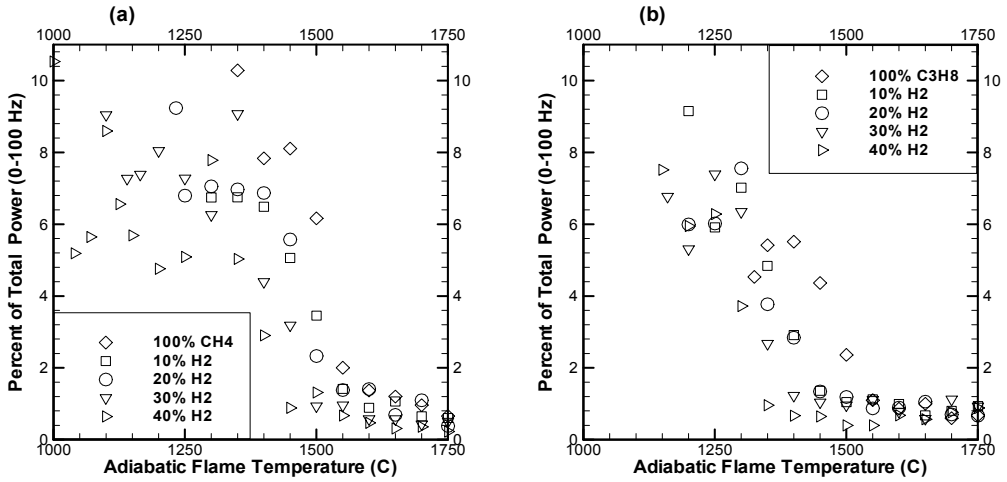

Figure 8.12. Percent of the noise power which occurred at frequencies less than 100 Hz: a) CH_4 flames, and b) C_3H_8 flames.

CHAPTER 9: CONCLUSIONS

Experiments were conducted in a lean premixed combustor to obtain data on flame stability/ blow out and on emissions of CO and NOx using H_2-enriched CH_4 or natural gas to achieve the first goal. The flame structure was identified qualitatively by luminous photographs and quantitatively by OH PLIF measurements. The results showed that the lean stability limit was lowered by the addition of H_2 to the fuel. A significant reduction in CO emissions was realized by H_2 addition as the lean stability limit of natural gas was approached. The NOx emissions for a given equilibrium adiabatic flame temperature were not affected by the H_2 addition. The flame size and shape of H_2-enriched fuel were qualitatively similar to those obtained with CH_4 flame at a higher equilibrium adiabatic flame temperature. The improved stability with H_2 enrichment was postulated to be a direct result of higher OH, H, and O radical concentrations, which increase several key reaction rates. The OH PLIF measurements showed that moderate amounts of H_2 enrichment led to significant increases in the OH radical concentrations. Increasing amounts of H_2 enrichment to the highest levels increased the radical concentrations only marginally for the conditions tested in this study. Hydrogen addition produced a broader region of high OH concentrations. Flame characteristics were most significantly affected by reactions in the torroidal corner recirculation zone.

The 2-D instantaneous velocity field was measured using particle image velocimetry to accomplish the second goal. Measurements were taken for a non-reacting flow, a CH_4 flame and a H_2-enriched CH_4 flame. The time-averaged

flow field was affected not only by combustion but also by fuel composition. In particular, the addition of H_2 to CH_4 changes the orientation of the inlet jet, indicating changes in the location and rates of heat release with different fuels. Size of the central recirculation zone was not significantly affected by combustion or H_2 addition to CH_4. This result differs from unconfined flows allowing thermal expansion in the horizontal direction to produce a wider recirculation region in reacting flows. The instantaneous flow fields contained smaller, random vortical structures that were not observed in the time-averaged flow fields. The maximum velocity magnitude in the instantaneous fields was similar to that in the averaged fields. Regions with large RMS velocity matched with regions of high mean velocity. The CH_4 flame contained a broad region of high RMS velocity and turbulent kinetic energy near the inlet jet, suggesting unsteady heat release. The kinetic energy dissipation field showed strand shaped structures in the corner recirculation and inlet jet regions for all the three cases. The instantaneous vorticity and normal strain were 4 to 7 times higher than the average values. The highest vorticity and strain magnitudes were not affected significantly by combustion or H_2 addition.

Simultaneous measurements of OH and velocity fields were obtained for CH_4 and H_2-enriched CH_4 flames which completed the third major goal of the work. Results showed that the overall flame and flow structures for the two cases were different. The CH_4 flame was longer, and lacked combustion in the corner recirculation region, whereas the H_2-enriched flame was shorter and more robust with reactions occurring in the corner recirculation region. Reactions in the CH_4

flame stabilized in the inner shear layer whereas those in the H_2-enriched flame stabilized in the inlet jet region. The simultaneous images show several small-scale vortical structures wrapping OH layers around them, which was not visible in the time-averaged fields. The H_2-enriched flame also stabilized in regions without flow recirculation. Reactions in the CH_4 flame stabilized at the location of the highest compressive strain. However, reaction zones of the H_2-enriched CH_4 flame were less influenced by the flow field because of H_2's high resistance to strain providing improved flame stability.

The burner was operated on H_2-enriched CH_4 and C_3H_8 at several fuel composition ratios while emissions and noise data were collected to finish the fourth goal. The flame length was shown to increase with decreasing flame temperature for different fuels. The addition of H_2 shortened the flame at leaner conditions and had minimal effect at higher temperatures. The NOx concentration increased exponentially with temperature for all cases because of the thermal mechanism. The CO concentration data also showed an exponential increase with temperature due to reduced oxygen concentration. The CO emissions suddenly increased prior to the LBO because of the local instabilities in the flame and poor CO burn off. The noise data showed acoustic power increasing with flame temperature for all fuels. Furthermore, the noise spectra showed considerable variation for the different fuels. For example, the 40% H_2 in CH_4 flame produced the loudest sound with an audibly tonal nature, which was caused by a high peak power at a single frequency near 450 Hz. The other fuels had two major peaks at 450 Hz and 600 Hz, which competed with each other

either directly or temporally, acting to reduce the sound levels to varying extents. The noise level decreased at lower flame temperatures although the 40% H_2 flame still had a strong peak at 450Hz. Only a moderate increase of low frequency (0-100Hz) noise near LBO was observed, possibly because of the high level of premixedness in the present system. The maximum sound power at high temperatures was observed at frequencies around 450 Hz and 600 Hz. Overall, results show significant effects of fuel composition on flame length, emissions, lean blow out, and combustion noise.

CHAPTER 10: RECOMMENDATIONS

The following recommendations are made to improve the experiment and to continue the present work:

- The fuel flow rates should be measured using a more accurate device such as laminar flow elements. This would reduce the uncertainty in the adiabatic flame temperature significantly, and allow for finer graduation in experiments when temperature is varied.
- A gas chromatograph should be used to measure the major species and some of the pollutant species at a point, which would enhance the ability to understand the effect of these multi-component fuels on combustion.
- An optically based gas analysis system could improve the rate at which experiments can be operated due to their faster response time. Such devices may require less frequent calibration as well.
- The effect of changing the inlet swirl number on combustion and sound could be studied to determine their role on various flame properties.
- The length of the premix section could be varied to determine the effect of premixing length on combustion dynamics.
- In order to study secondary effects, tertiary fuel blends could be studied. These blends more closely approximate the conditions of a burner utilizing alternative fuels, as the additives may have complimentary or competing effects.
- Samples of alternative fuels could also be utilized in the combustor to observe the lean premixed combustion performance of these fuels.

CHAPTER 11: REFERENCES

Adouane, B., Van der Wel, M. C., De Jong, W., and Van Buijtenen, J. P. (2003). "Experimental Investigation on a Newly Designed Combustor for LCV Gas," *ASME Paper GT2003-38930*.

Alavandi, S. K., and Agrawal, A. K. (2004). "Lean Premixed Combustion of Methane and Hydrogen-Enriched Methane Using Porous Inert Media," *ASME Paper GT2004-53231*.

Anderson, D. N. (1975). "Effect of Hydrogen Injection on Stability and Emissions of an Experimental Premixed Prevaporized Propane Burner," *NASA TM X-3301*.

Archer, S., and Gupta, A. K. (2004). "Effect of Swirl on Flow Dynamics in Unconfined and Confined Gaseous Fuel Flames," *AIAA Paper 2004-0813*.

Barlow, R. S., and Collignon, A. (1991). "Linear LIF Measurements of OH in Nonpremixed Methane-Air Flames: When are Quenching Corrections Unnecessary," AIAA Paper 91-0179.

Bell, S. R., and Gupta, M. (1997). "Extension of the Lean Operating Limit for Natural Gas Fueling of a Spark Ignited Engine Using Hydrogen Blending," *Combustion Science and Technology* vol. 123, pp. 23-47.

Bhargava, A., Colket, M., Sowa, W., Castelton, K., and Maloney, D. (2000). "An Experimental and Modeling Study of Humid Air Premixed Flames," *Journal of Engineering for Gas Turbines and Power*, Vol. 122, pp. 405-411.

Cattolica, R. J. (1982). "OH Radical Nonequilibrium in Methane-Air Flat Flames," *Combustion and Flame*, vol. 44, pp. 43-59.

Choudhuri, A. R., and Gollahalli, S. R. (2000). "Laser Induced Fluoresence Measurements of Radical Concentrations in Hydrogen-Hydrocarbon Hybrid Gas Fuel Flames," *International Journal of Hydrogen Energy*, Vol. 25, pp. 1119-1127.

Choudhuri, A. R., and Gollahalli, S. R. (2003). "Stability of Hydrogen/Hydrocarbon Blended Fuel Flames," *Journal of Propulsion and Power*, Vol. 19, No. 2, March-April.

Cong, Y., and Jackson, G. S. (1999) "Impact of Hydrogen Doping on Lean-Premixed Methane Flame Stability," *Fall Technical Meeting of the Eastern States Section of the Combustion Institute*.

Donbar, J. M., Driscoll, J. F., and Carter, C. D. (1998). "Simultaneous CH Planar Laser-Induced Fluorescence and Particle Imaging Velocimetry in Turbulent Flames," *AIAA Paper 1998-0151*.

Donbar, J. M., Driscoll, J. F., and Carter, C. D. (2001). "Strain Rates Measured Along the Wrinkled flame Contour Within Turbulent Non-Premixed Jet Flames," *Combustion and Flame*, vol. 125, pp. 1239-1257.

Flores, R. M., Miyasato, M. M., McDonell, V. G., and Samuelsen, G. S. (2001). "Response of a Model Gas Turbine Combustor to Variation in Gaseous Fuel Composition," *Journal of Engineering for Gas Turbines and Power*, Vol. 123, pp. 824-831.

Gauducheau, J. L., Denet, B. and Searby, G. (1998). "A Numerical Study of Lean CH4/H2/Air Premixed Flames at High Pressure," *Combustion Science and Technology,* vol. 137, pp. 81-99.

Griebel, P., Schären, R., Siewert, P., Bombach, R., Inauen, A., and Kreutner, W. (2003). "Flow Field and Structure of Turbulent High Pressure Premixed Methane/Air Flames," *ASME Paper GT-2003-38398*, June 2003.

Gupta, A. K., Lilley, D. G., and Syred, N. (1984). *Swirl Flows*, Abacus Press, Tunbridge Wells, England.

Gupta, A. K., Lourenco, L., Linck, M., and Archer, S. (2004). "New Particle-Image-Velocimetry Method to Measure Flowfields in Luminous Spray Flames," *Journal of Propulsion and Power*, vol. 20, no. 2, pp. 369-372.

Han, D., and Mungal, M. G.. (2000). "*PIV Lab 2000*" ver. 1.50, Stanford University, Stanford CA.

Han, D., and Mungal, M. G.. (2003). "Simultaneous Measurements of Velocity and CH Distributions. Part 1: Jet Flames in Co-Flow," *Combustion and Flame*, Vol. 132, pp. 565-590.

Hasegawa, T., Hisamatsu, T., Katsuki, Y., Sato, M., Koizumi, H., Hayashi, A., and Kobayasi, N. (2000). "Development of Low NOx Combustion Technology in Medium-Btu Fueled 1300^{o}C-Class Gas Turbine Combustor in IGCC," *ASME Paper 2000-GT-0028*.

Hasegawa, T., Sato, M., and Nakata, T. (2001). "A Study of Combustion Characteristics of Gasified Coal Fuel," *Journal of Engineering for Gas Turbines and Power*, Vol. 123, pp. 22-32.

Haste, M. J. (2000). *An Investigation of In-Cylinder Flow and Combustion in a Spark Ignition Engine Using Particle Image Velocimetry*, Doctoral Dissertation, Loughbourough University, Leicestershire, UK.

Jackson, G. S., Sai, R., Plaia, J. M., Boggs, C. M., and Kiger, K. T. (2003). "Influence of H_2 on the Response of Lean Premixed CH_4 Flames to High Strained Flows," *Combustion and Flame*, Vol. 132, pp. 503-511.

Janus, M. C., Richards, G. A., Yip, M. J., Robey, E. H. (1997). "Effects of Ambient Conditions and Fuel Composition on Combustion Stability," *ASME Paper GT97-266*.

Ji, J., and Gore, J. (2002). "Flow Structure in Lean Premixed Swirling Combustion," *Proceedings of the Combustion Institute*, Vol. 29, pp. 861-867.

Jones, H. R. N., and Leng, J. (1994). "The Effect of Hydrogen and Propane Addition on the Operation of a Natural Gas-Fired Pulsed Combustor," *Combustion and Flame*, Vol. 99, pp. 404-412.

Kalt, P. A. M., Frank, J. H., and Bilger, R. W. (1998). "Laser Imaging of Conditional Velocities in Premixed Propane-Air Flames by Simultaneous OH PLIF and PIV," *Proceedings of the Combustion Institute*, vol. 27, pp. 751-758.

Kalt, P. A. M., Al-Abdeli, Y. M., Masri, A. R., and Barlow, R. S. (2002) "Swirling Turbulent Non-Premixed Flames of Methane: Flow Field and Compositional Structure," *Proceedings of the Combustion Institute*, Vol. 29, pp. 1913-1919.

Kee, R. J., Rupley, F. M., and Miller, J. A. (1989). "Chemkin-II: A Fortran Chemical Kinetics Package for the Analysis of Gas Phase Chemical Kinetics," Sandia Report *SAND89-809B-UC-706*.

Kothnur, P. S., Tsurikov, M. S., Clemens, N. T., Donbar, J. M., and Carter, C. D. (2002). "Planar Imaging of CH, OH, and Velocity in Turbulent Non-Premixed Jet Flames," *Proceedings of the Combustion Institute*, vol. 29, pp. 1921-1927.

Kushari, A., Rosen, L. J., Jagoda, J. L., and Zinn, B. T. (1996). "The Effect of Heat Content and Composition of Fuel on Pulse Combustion Performance," *Proceedings of the Combustion Institute*, Vol. 26, pp. 3363-3368.

Larsen, J. F., and Wallace, J. S. (1997). "Comparison of Emissions and Efficiency of a Turbocharged Lean-Burn Natural Gas and Hythane-Fueled Engine," *Journal of Engineering for Gas Turbines and Power*, vol. 119 pp. 218-226.

Lieuwen, T., Neumeier, Y., and Zinn, B. T. (1998). "The Role of Unmixedness and Chemical Kinetics in Driving Combustion Instabilities in Lean Premixed Combustors," *Combustion Science and Technology*, Vol. 135, pp. 193-211.

Maden, K. H. (1998). "Fuel Flexibility in Industrial Gas Turbines," Turbomachinery Technology Seminar, Solar Turbines, San Diego, CA.

Meier, J. G., Hung, W. S. Y., and Sood, V. M. (1986). "Development and Application of Industrial Gas Turbines for Medium-BTU Gaseous Fuels," *Journal of Engineering for Gas Turbines and Power*, vol. 108, pp. 182-190.

Meyers, J. F., and Kubesh, J. S. (1997). "The Hybrid Rich-Burn/Lean-Burn Engine," *Journal of Engineering for Gas Turbines and Power*, vol. 119, pp. 218-226.

Morris, J. D., Symonds, R. A., Ballard, F. L., and Banti, A. (1998). "Combustion Aspects of Application of Hydrogen and Natural Gas Fuel Mixtures to MS9001E DLN-1 Gas Turbines at Elsta Plant, Terneuzen, The Netherlands," *ASME Paper 98-GT-359*.

Mueller, C. (1997). "*lscorrspef.m*," Livermore, CA.

Munson, B. R., Young, D. F., and Okiishi, T. H. (1994) *Fundamentals of Fluid Mechanics*, 2nd ed, John Wiley and Sons, New York, New York.

Nair, S., and Lieuwen, T. (2003). "Acoustic Detection of Imminent Blowout in Pilot and Swirl-Stabilized Combustors," *ASME Paper GT2003-38074*.

Nguyen, O. and Samuelson, S. (1999). "Effect of Discrete Pilot Hydrogen Dopant Injection of the Lean Blow Out Performance of a Model Gas Turbine Combustor," *ASME Paper 99-GT-359*.

Nord, L. O., and Andersen, H. G. (2003). "Influence of Variations in the Natural Gas Properties on the Combustion Process in Terms of Emissions and Pulsations for a Heavy-Duty Gas Turbine," *ASME Paper IJPGC2003-40188*.

Paul, P. H. (1994). "A Model for Temperature-Dependent Collisional Quenching of OH $A^2\sum^+$**,"** *Journal of Quantitative Spectroscopy and Radiative Transfer*, vol. 51, pp. 511-524.

Peters, N. (1999). "The Turbulent Burning Velocity for Large-Scale and Small-Scale Turbulence," *Journal of Fluid Mechanics*, Vol. 384, pp. 107-132.

Phillips, J. N., and Roby, R. J. (1999). "Enhanced Gas Turbine Combustor Performance Using H_2-Enriched Natural Gas," *ASME Paper 99-GT-115*.

Qin, W., Egolfopoulos, F. N., and Tsotsis, T. T. (2001) "Fundamental and Environmental Aspects of Landfill Gas Utilization for Power Generation," *Chemical Engineering Journal*, vol. 82, pp. 157-172.

Raffel, M., Willert, C., and Kompenhans, J. (1984). *Particle Image Velocimetry: A Practical Guide*, Springer, New York, NY, pp. 157-166.

Rehm, J. E., and Clemens, N. T. (1999). "The Association of Scalar Dissipation Rate Layers and OH Zones with Strain, Vorticity, and 2-D Dilatation Fields in Turbulent Nonpremixed Jets and Jet Flames," *AIAA Paper 99-0676*.

Rehm, J. E., and Clemens, N. T. (1998). "The Relationship Between Vorticity/Strain and Reaction Zone Structure in Turbulent Non-Premixed Jet Flames," *Proceedings of The Combustion Institute*, vol. 27, pp. 1113-1120.

Ren, J. Y, Qin, W., Egolfopoulos, F. N., Mak, H., and Tsotsis, T. T. (2001). "Methane Reforming and its Potential Effect on the Efficiency and Pollutant Emissions of Lean Methane–Air Combustion," *Chemical Engineering Science*, vol. 56, pp. 1541.

Ren, J. Y., Qin, W., Egolfopoulos, F. N., and Tsotsis, T. T. (2001). "Strain Rate Effects on Hydrogen-Enhanced Lean Premixed Combustion," *Combustion and Flame*, Vol. 124, pp. 717-720

Richards, G. A., and Janus, M. C. (1998). "Characterization of Oscillations During Premix Gas Turbine Combustion," *Journal of Engineering for Gas Turbines and Power*, Vol. 120, pp. 294-302.

Richards, G. A., McMillian, M. M., Gemmen, R. S., Rogers, W. A., and Cully, S. R. (2001). "Issues for Low-Emission, Fuel-Flexible Power Systems," *Progress in Energy and Combustion Science*, Vol. 27, pp. 141-169.

Rogg, B. and Wang, W. (1995). *RUN-1DL The Laminar Flame and Flamelet Code User Manual*, Rurh University, Bochum, Germany.

Serway, R.A. (1992). *Physics for Scientists and Engineers*, 3rd ed., Saunders College Publishing, Fort Worth, Texas.

Schefer, R. W., Smith, T. D., and Marek, C. J. (2002). "Evaluations of NASA Lean Premixed Hydrogen Burner," Sandia Report *SAND2002-8609*.

Schefer, R. W., Wicksall, D. M., and Agrawal, A. K. (2002). "Combustion of Hydrogen-Enriched Methane in a Lean Premixed Swirl-Stabilized Burner," *Proceedings of The Combustion Institute*, Vol. 29, 2002, pp 843-851.

Schlichting, H., and Kestin, J. (1979). *Boundary Layer Theory*, 7th ed, McGraw-Hill, New York, New York.

Tsurikov, M. S., and Clemens, N. T. (2002). "The Structure of Dissipative Scales in Axisymmetric Turbulent Gas-Phase Jets," *AIAA Paper 2002-0164*.

Watson, K. A., Lyons, K. M., Carter, C. D., and Donbar, J. M. (2002). "Simultaneous Two-Shot CH Planar Laser-Induced Fluorescence and Particle Image Velocimetry Measurements in Lifted CH_4/Air Diffusion Flames," *Proceedings of the Combustion Institute*, vol. 29, pp. 1905-1912.

Wheeler, A.J., and Ganji, A.R. (1996). *Introduction to engineering Experimentation*, Prentice Hall, Upper Saddle River, New Jersey.

Wicksall, D. M., and Agrawal, A. K. (2001). "Effects of Fuel Composition on Flammability Limit of a Lean Premixed Combustor," *ASME Paper GT2001-007*.

Wicksall, D. M., Agrawal, A. K., Schefer, R. W., and Keller, J. O. (2003). "Fuel Composition Effects on the Velocity Field in a Lean Premixed Swirl-Stabilized Combustor," *ASME Paper GT2003-38712*.

Wu, S., Zhang, H., Ren, J. Y., Qin, W., and Al-Wahabi, S. (1999). "Effect of Oxygen Enrichment of the Dynamics and Structure of Lean Methane-Air Premixed Flames," *Proceedings of the Western States Section of the Combustion Institute, Paper 99F-56*.

APPENDIX 1: SAMPLE CALCULATIONS

The following sample calculations are performed for a flame utilizing 40% H_2 and 60% CH_4 fuel at a flame temperature of 1350 ^{0}C. Built in MATLAB routines were used to obtain average and RMS values.

The hydraulic diameter (D_h) must be used to calculate the inlet Reynolds number to account for the effects of flow through an annulus. The D_h is equal to 4 times the ratio of the cross sectional area to the wetted perimeter (Munson et al., 1994). In the equation below r_0 is the premixer radius and r_i is the centerbody radius.

$$D_h = \frac{4\pi\left(r_0^2 - r_i^2\right)}{2\pi\left(r_0 + r_i\right)} = 2\left(2.025 - 1\right)cm = 2.05cm$$

The bulk vertical inlet velocity was also necessary to calculate the Reynolds number.

$$V = \frac{Q}{A} = \frac{Q}{\pi(r_0^2 - r_i^2)} = \frac{0.0097\, m^3/s}{\pi\left(2.025^2 - 1^2\right)m^2 * 10^{-4}} = 10\, m/s$$

The Reynolds number was calculated using the equation below where ν is the kinematic viscosity of air at 1 ATM and 20 ^{0}C ($1.51*10^{-5}$ m^2/s) (Munson et al., 1994).

$$\mathrm{Re} = \frac{V * D_h}{\nu} = \frac{10\, m/s * .0205m}{1.51*10^{-5}\, m^2/s} = 13{,}576$$

The Reynolds numbers for a CH_4 flame enriched with 40% H_2 at a flame temperature of 1350 C is 13,117 due to the changes in viscosity ($1.7881*10^{-5}$ $N*s/m^2$) and density (1.1442 kg/m^3). The Reynolds number for a 100% CH_4 flame is 13,487, the density is 1.1732 kg/m3, and the dynamic viscosity is $1.7832*10^{-5}$.

To determine the ability of the seed particles to accurately track the small scales of motion of the flow, the Stokes number is caluculated, which is the ratio of the time scale of the particles raction to the velocity field, and time scales of the flow. The scalar dissipation, ε, is necessary to calculate the Kolmogorov time scale and is estimated below. Alternatively, if the maximum value of the RMS velocity is used, then ε = 341333.

$$\varepsilon \approx \frac{u'^3}{L} = \frac{\left(2\,m/s\right)^3}{0.0015m} = 5333\,m^2/s^3$$

The Kolmogorov time scale is calculated below assuming the viscosity of air and using the lower value for scalar dissipation, if the higher value is used, the Kolmogorov time scale is $6.65*10^{-6}$s.

$$\tau_K = \left(\frac{\nu}{\varepsilon}\right)^{\frac{1}{2}} = \left(\frac{1.51*10^{-5}\,m^2/s}{5333\,m^2/s^3}\right)^{\frac{1}{2}} = 5.32*10^{-5}\,s$$

The time scale of the large eddies can be estimated as well. If the higher value for RMS velocity is used, the large eddy time scale is $1.9*10^{-4}$s.

$$\tau_{LE} = \frac{L}{u'} = \frac{0.0015m}{2\,{}^{m}\!/\!_{s}} = 7.5*10^{-4}\,s$$

The time scale of the particles response is calculated below.

$$\tau_P = \frac{\rho_P * D_P^2}{18\mu} = \frac{2100\,{}^{kg}\!/\!_{m^3} * \left(10^{-6}\,m\right)^2}{18*\left(1.51*10^{-5}\,N*s\,{}^{}\!/\!_{m^2}\right)} = 6.51*10^{-6}\,s$$

And finaly the Stokes number can be calculated as below for the shortest Kolmogorov time scale. The Stokes number for the large eddies is estimated to be between 0.009 and 0.03, indicating that particles capture large eddies well, and the Stokes number for the Kolmogorov time scales is between 0.1 and 1.0 indicating that the smallest scales of the flow may not be fully captured.

$$St = \frac{\tau_P}{\tau_K} = \frac{6.51*10^{-6}\,s}{6.65*10^{-6}\,s} = 0.98$$

The Swirl number of the inlet swirler was calculated using Eqn. 1.7 from Gupta et al. (1984) which is derived for flow through an axial swirler with a centerbody assuming plug flow and rigid body rotation. The angle phi is the acute angle between the fin and the direction of the flow prior to entering the swirler. The swirl number of the intial burner is shown below, the swirl number of the modified burner was calculated to be 1.5.

$$S = \frac{2}{3}\left[\frac{1-\left(\frac{D_h}{D}\right)^3}{1-\left(\frac{D_h}{D}\right)^2}\right] * Tan\phi = \frac{2}{3}\left[\frac{1-\left(\frac{2}{4}\right)^3}{1-\left(\frac{2}{4}\right)^2}\right] * Tan\phi = \frac{7}{9} * Tan(45) = 0.78$$

The stoichiometric air to fuel ratio was calculated using Eqn. 4.4 and the coefficients listed in Table 4.1.

$$\left.A/F\right)_{Stoich.} = (C1 + C2 * X) * 4.76 = (2 + (-1.5) * 0.4) * 4.76 = 6.664$$

The actual air to fuel ratio was calculated using the measured flow rates in SLPM.

$$\left.A/F\right)_{Acutal} = \frac{Q_{Air}}{Q_{CH4} + Q_{H2}} = \frac{536.71}{27.18 + 18.11} = 11.85$$

The equivalence ratio was calculated using Eqn. 4.1.

$$\Phi = \frac{\left.A/F\right)_{Stoich.}}{\left.A/F\right)_{Actual}} = \frac{6.664}{11.8} = 0.562$$

Using the measured air to fuel ratio, the adiabatic flame temperature was calculated using Eqn. 4.5 and the values from Table 4.2.

$$T_{AD} = D1 \bullet [AFR]^{D2} = 10181 * [11.85]^{-.8171} C = 1350.4C$$

The turbulent kinetic energy was calculated using Eqn. 4.12.

$$TKE = \frac{1}{2}\left(U_{RMS}^2 + V_{RMS}^2\right)$$

The two dimensional vorticity was calculated using a path integral method programmed into MATLAB. The code used follows below, the naming conventions for the points are the same as those in Figure 4.4 (a). The four "Gam" terms correspond to each side of the boundary, and vort(i,j) is the vorticity at the point. A nested loop structure performs this calculation at each point throughout the measurement field, excepting those at the edge of the field. The

distance between the velocity vectors in meters is delx and dely in the x and y directions, respectively.

```
delx = abs(x(1,2) - x(1,1))/1000; dely = abs(y(1,1) - y(2,1))/1000;
 for j = 2:N(2)-1
        for i = 2:N(1)-1
            Gam1(i,j) = delx*(u(i+1,j-1)+2*u(i+1,j)+u(i+1,j+1));
            Gam2(i,j) = dely*(v(i+1,j+1)+2*v(i,j+1)+v(i-1,j+1));
            Gam3(i,j) = -delx*(u(i-1,j+1)+2*u(i-1,j)+u(i-1,j-1));
            Gam4(i,j) = -dely*(v(i-1,j-1)+2*v(i,j-1)+v(i+1,j-1));
            vort(i,j) = ((Gam1(i,j)+Gam2(i,j)+Gam3(i,j)+Gam4(i,j)))/(8*delx*dely);
        end;
end;
```

A similar code was used to calculate the normal strain rate. Again, the four "norm" terms refer to a side of the boundary each, and the normal(i,j) term is the normal strain at the point.

```
delx = abs(x(1,2) - x(1,1))/1000; dely = abs(y(1,1) - y(2,1))/1000;     %dmw
 for j = 2:N(2)-1
         for i = 2:N(1)-1
                 norm1(i,j) = (u(i-1,j-1)+2*u(i-1,j)+u(i-1,j+1))/(8*dely);
                 norm2(i,j) = (u(i+1,j+1)+2*u(i+1,j)+u(i+1,j-1))/(8*dely);
                 norm3(i,j) = (v(i-1,j+1)+2*v(i,j+1)+v(i+1,j+1))/(8*delx);
                 norm4(i,j) = (v(i+1,j-1)+2*v(i,j-1)+v(i-1,j-1))/(8*delx);
```

```
            normal(i,j) = (norm1(i,j)-norm2(i,j)+norm3(i,j)-norm4(i,j));
        end;
end;
```

The kinetic energy dissipation rate was also calculated using a modified version of the path integral method. The kinetic energy consists of two terms which are like the normal strain, and also has a term like the shearing strain.

```
for (i = 2:1:60);
    for (j = 2:1:60);
        %calc du/dx
            norm3(i,j) = (v(i-1,j+1)+2*v(i,j+1)+v(i+1,j+1))/(8*delx);
            norm4(i,j) = (v(i+1,j-1)+2*v(i,j-1)+v(i-1,j-1))/(8*delx);
            dudx(i,j) = norm3(i,j)-norm4(i,j);
        %calc dv/dy
            norm1(i,j) = (u(i-1,j-1)+2*u(i-1,j)+u(i-1,j+1))/(8*dely);
            norm2(i,j) = (u(i+1,j+1)+2*u(i+1,j)+u(i+1,j-1))/(8*dely);
            dvdy(i,j) = norm1(i,j)-norm2(i,j);
        %calc shear xy
            shear1(i,j) = (v(i+1,j-1)+2*v(i+1,j)+v(i+1,j+1))/(8*dely);
            shear2(i,j) = (v(i-1,j+1)+2*v(i-1,j)+v(i-1,j-1))/(8*dely);
            shear3(i,j) = (u(i-1,j-1)+2*u(i,j-1)+u(i+1,j-1))/(8*delx);
            shear4(i,j) = (u(i+1,j+1)+2*u(i,j+1)+u(i-1,j+1))/(8*delx);
            shearing(i,j) = (-shear1(i,j)+shear2(i,j)-shear3(i,j)+shear4(i,j));
```

```
        %calc dissipation
            diss(i,j) = 2*Visc*((dudx(i,j))^2+(dvdy(i,j))^2+.5*(shearing(i,j))^2);
    end;
end;
```

The integral length scale was also calculated by finding the correlation coefficients for the vertical velocity at 15 grid locations in the downstream direction from the point. These correlation coefficients were then integrated using a trapezoid rule to find the integral length scale. Due to the many averaging functions in the correlation and the number of correlations the calculations were automated in a MATLAB program.

First the difference of the instantaneous and mean velocities is acquired at the point and locations downstream.

```
delu0(i)=((v(row,col))-(vavg(row,col)));
delu1(i)=((v(row-1,col))-(vavg(row-1,col)));
```

Second, these differences are multiplied together.

```
prod1=delu0(i)*delu1(i);
```

Using the definition of the RMS velocity, a substitution is made for the bottom half of the correlational coefficient, and the coefficient can now be calculated.

```
R1(j)=((mean(prod1))/(((rms1(row,col)^2+rms2(row,col)^2)^.5)*((rms1(r
ow-1,col)^2+rms2(row-1,col)^2)^.5)));
```

These correlational coefficients are calculated for R0 up to R15 and integrated.

APPENDIX 2: UNCERTAINTY ANALYSIS

The uncertainty analysis will be split into two sections, one for the modified setup used in the University of Oklahoma Gas Turbine Research Laboratory, and the other for the setup used at Sandia National Laboratories.

Uncertainty in the measurements at the University of Oklahoma:

The LFE used to measure the air flow rate has a manufacturer's uncertainty of 0.5 % of full scale, or 5 SLPM. The fuel flow meters utilized have uncertainties of 1% of full scale according to the manufacturer, which are 0.6 and 0.3 SLPM. The uncertainty of the fuel additive flow meter was less for some cases where a 0-15 SLPM meter was used. The emissions measurements have an uncertainty of 2 ppm according to the manufacturer.

Uncertainty propagation into the calculated quantities:

The first calculation made from the flow rates is the air to fuel ratio. The uncertainties shown below are for the operating conditions used in the sample calculations in Appendix 1.

$$\left.A/F\right)_{Acutal} = \frac{Q_{Air}}{Q_{CH4} + Q_{H2}}$$

$$\omega_{AFR} = \sqrt{\left(\frac{\partial(AFR)}{\partial(Q_{CH4})} * \omega_{CH4}\right)^2 + \left(\frac{\partial(AFR)}{\partial(Q_{AIR})} * \omega_{air}\right)^2 + \left(\frac{\partial(AFR)}{\partial(Q_{H2})} * \omega_{H2}\right)^2}$$

$$\omega_{AFR} = \sqrt{\left(-\frac{Q_{air}}{(Q_{CH4}+Q_{H2})^2} * \omega_{CH4}\right)^2 + \left(\frac{1}{Q_{CH4}+Q_{H2}} * \omega_{air}\right)^2 + \left(-\frac{Q_{air}}{(Q_{CH4}+Q_{H2})^2} * \omega_{H2}\right)^2}$$

$$\omega_{AFR} = \sqrt{\left(\frac{-536.71}{(27.18+18.12)^2} * .6\right)^2 + \left(\frac{1}{27.18+18.12} * 5\right)^2 + \left(\frac{-536.71}{(27.18+18.12)^2} * .3\right)^2}$$

$$\omega_{AFR} = 0.21$$

The adiabatic flame temperature is then calculated from the air to fuel ratio using the correlations derived from adiabatic flame temperature calculations.

$$T_{AD} = D1 \bullet [AFR]^{D2\ 0}C$$

$$\omega_{Tad} = \sqrt{\left(\frac{\partial(T_{AD})}{\partial(AFR)} * \omega_{AFR}\right)^2}\ ^0C$$

$$\omega_{Tad} = \sqrt{\left(\frac{D2 * D1}{(AFR)^{(-D2+1)}} * \omega_{AFR}\right)^2}\ ^0C$$

$$\omega_{Tad} = \sqrt{\left(\frac{-.8171 * 10181}{(11.85)^{1.8171}} * 0.21\right)^2}\ ^0C$$

$$\omega_{Tad} = 19^0C$$

The uncertainty in the H_2 mole fraction in the fuel can also be calculated from the flow rates, and is less than 1%.

$$X_{H2} = \frac{Q_{H2}}{Q_{H2} + Q_{CH4}}$$

$$\omega_{XH2} = \sqrt{\left(\frac{\partial(X_{H2})}{\partial(Q_{H2})} * \omega_{H2}\right)^2 + \left(\frac{\partial(X_{H2})}{\partial(Q_{CH4})} * \omega_{CH4}\right)^2}$$

$$\omega_{XH2} = \sqrt{\left(\frac{Q_{CH4}}{(Q_{H2} + Q_{CH4})^2} * \omega_{H2}\right)^2 + \left(\frac{-Q_{H2}}{(Q_{H2} + Q_{CH4})^2} * \omega_{CH4}\right)^2}$$

$$\omega_{XH2} = \sqrt{\left(\frac{27.18}{(27.18 + 18.12)^2} * .3\right)^2 + \left(\frac{-18.12}{(27.18 + 18.12)^2} * .6\right)^2}$$

$$\omega_{XH2} = 0.0066$$

The uncertainties in the air to fuel ratio and the mole fraction of H_2 in the fuel propagate into the uncertainty in the equivalence ratio.

$$\Phi = \frac{(C1 + C2 * X_{H2}) * 4.76}{AFR}$$

$$\omega_{\Phi} = \sqrt{\left(\frac{\partial(\Phi)}{\partial(X_{H2})} * \omega_{XH2}\right)^2 + \left(\frac{\partial(\Phi)}{\partial(AFR)} * \omega_{AFR}\right)^2}$$

$$\omega_{\Phi} = \sqrt{\left(\frac{4.76 * C2}{AFR} * \omega_{XH2}\right)^2 + \left(\frac{-4.76 * (C1 + C2 * X_{H2})}{(AFR)^2} * \omega_{AFR}\right)^2}$$

$$\omega_{\Phi} = \sqrt{\left(\frac{4.76*(-1.5)}{11.85}*.0066\right)^2 + \left(\frac{-4.76*(2-1.5*X_{H2})}{11.85^2}*.21\right)^2}$$

$$\omega_{\Phi} = 0.011$$

Uncertainty in the measurements at Sandia National Laboratory:

The flow measurement equipment utilized at SNL had similar uncertainties as that used at the University of Oklahoma. Therefore, attention will be focused on the uncertainties in the OH PLIF and the PIV measurements. The OH PLIF signal was equal to the mole fraction to with in 10% of the peak value according to the work of Barlow and Collignon (1991). There findings were for a non-premixed flame however, so using the same methods, the error in a simple opposed flow configuration was calculated. This was possible because all the relevant species and temperature data was provided by RUN1-DL. The result of this analysis showed that the errors caused by not accounting for quenching and the state of the population may be closer to 5% of the peak value. However, 10% of the peak value has been reported to be conservative.

The uncertainty in the PIV field was calculated using the equations from Haste's Dissertation (2000), and modifying them slightly for this case as described in Chapter 4. A copy of part of the MATLAB program utilized to calculate the uncertainty follows. This portion of the program uses a double looping structure to systematically calculate the uncertainty at all the interior interrogation regions. Another outer loop also scans through multiple images in

the run, to increase the number of points sufficiently. Finally all the uncertainty data is placed in a linear array in increasing order, and the value of the 95th percentile is calculated.

```
%calculate the uncertainties using the path integral method
   for (i = 2:1:60);
      for (j = 2:1:60);
      %calc du/dx
         norm3(i,j) = (v(i-1,j+1)+2*v(i,j+1)+v(i+1,j+1))/(8*delx);
         norm4(i,j) = (v(i+1,j-1)+2*v(i,j-1)+v(i-1,j-1))/(8*delx);
         dudx(i,j) = norm3(i,j)-norm4(i,j);
      %calc dv/dy
         norm1(i,j) = (u(i-1,j-1)+2*u(i-1,j)+u(i-1,j+1))/(8*dely);
         norm2(i,j) = (u(i+1,j+1)+2*u(i+1,j)+u(i+1,j-1))/(8*dely);
         dvdy(i,j) = norm1(i,j)-norm2(i,j);
      %calc du/dy
         shear1(i,j) = (v(i+1,j-1)+2*v(i+1,j)+v(i+1,j+1))/(8*dely);
         shear2(i,j) = (v(i-1,j+1)+2*v(i-1,j)+v(i-1,j-1))/(8*dely);
         dudy(i,j) = shear2(i,j)-shear1(i,j);
      %calc dv/dx
         shear3(i,j) = (u(i-1,j-1)+2*u(i,j-1)+u(i+1,j-1))/(8*delx);
         shear4(i,j) = (u(i+1,j+1)+2*u(i,j+1)+u(i-1,j+1))/(8*delx);
         dvdx(i,j) = shear4(i,j)-shear3(i,j);
```

```
    %Calculate the random or precision error
    Vo(i,j) = (sqrt(u(i,j)^2+v(i,j)^2));
    Rnd(i,j) = (1/(Vo(i,j)*(sqrt(12*N))))*(sqrt(L^2*(dudx(i,j)^2+dudy(i,j)^2+
       dvdx(i,j)^2+dvdy(i,j)^2)+W^2*(dudz^2+dvdz^2)));
    Rndper(i,j) = (Rnd(i,j)/Vo(i,j))*100;

    %calculate the systematic or bias error
    bias(i,j) = -(Delt/(Vo(i,j)))*sqrt((u(i,j)*dudx(i,j)+v(i,j)*dudy(i,j))^2+
       (u(i,j)*dvdx(i,j)+v(i,j)*dvdy(i,j))^2);
    biasper(i,j) = (bias(i,j)/Vo(i,j))*100;
    %calculate the total error assuming most probable(square root of the sum of
the squares)
    total(i,j) = sqrt(Rnd(i,j)^2+bias(i,j)^2);
    totalper(i,j) = (total(i,j)/Vo(i,j))*100; %percent error
    end;
  end;
```

APPENDIX 3: OPPOSED FLOW FLAME REACTION MECHANISM

The reaction mechanism utilized in the opposed flame calculations is presented below as formatted for the RUN1-DL software. This mechanism was utilized because there was an existing solution for a similar flame which was used as an initial guess. The mechanism was included with the program's examples, specifically example 7, and has been used without any changes. The species used in the mechanism are presented below in the symbol input file in RUN1-DL (EX7SYM) Rogg and Wang (1995).

```
LIST OF SYM / CHNO.....................................
Y    CH4      1400
Y    O2       0002
Y    H2O      0201
Y    CO2      1002
Y    CO       1001
Y    H2       0200
Y    H        0100
Y    OH       0101
Y    O        0001
Y    HO2      0102
Y    CH3      1300
Y    CHO      1101
Y    CH2O     1201
Y    H2O2     0202
Y    CH       1100
Y    CH2      1200
Y    N2       0020
-END OF SYM   1234
BOUNDS ON TEMPERATURE.............
0298.00    2500.00
-END OF BOUNDS
CHEMTP: TYPE OF CHEMISTRY.........
DETAILED CHEMISTRY
-END OF CHEMTP
```

The mechanism is from a file called EX7MEC, which was the mechanism input file for example 7 (Rogg and Wang, 1995). The two first letters of each line

determine how the program interprets the line. The comment lines are preceded by NN or CC, the reactions utilized are preceded by YY. Spaces and placeholders have been deleted to format the file to fit the page.

```
NN  ----------ELEMENTARY REACTION----!!-----A----!!ALPHA-!!---E--
NN  A AND ALPHA IN CM-MOL-SEC UNITS, E IN KJ/MOLE
                                     !!-----A----!!ALPHA-!!---E--
NN                                   !!   E10.3  !! F6.1 !!  F8.1
CPMECHANISM OF CH4-AIR, P=1BAR,  C1-CHEMISTRY
.............................
NN***********************************!!**********!!******!!******
*
CC===  H2/O2 - MECHANISM (GOOD FOR PREMIXED AND DIFFUSION FLAMES)
CC R1
CC  BAULCH-VALUE MINUS 10 PERCENT

YY    O2  + H = OH  + O              !! 2.20 E 14!! 0.00 !!70.30
NN    OH  + O = O2  + H              !! 1.57 E 13!! 0.00 !! 3.52
CC R2
YY    H2  + O = OH  + H              !! 5.06 E  4!! 2.67 !!26.3
NN    OH  + H = H2  + O              !! 2.22 E  4!! 2.67 !!18.29
CC R3
YY    H2  +OH = H2O + H              !! 1.00 E  8!! 1.60 !!13.8
NN    H2O + H = H2  + OH             !! 4.31 E  8!! 1.60 !!76.46
CC R4
YY    OH  +OH = H2O + O              !! 1.50 E  9!! 1.14 !! 0.42
NN    H2O + O = OH  + OH             !! 1.47 E 10!! 1.14 !!71.09
CC R5
YY    H   + H + M'= H2 + M'          !! 1.80 E 18!!-1.00 !! 0.00
NN    H2  + M'= H + H + M'           !! 7.26 E 18!!-1.00 !!436.81
CC R6
YY    H + OH + M'= H2O +  M'         !! 2.20 E 22!!-2.00 !! 0.00
NN    H2O + M'= H + OH +  M'         !! 3.83 E 23!!-2.00 !!499.48
CC R7
YY    O + O + M'= O2 +  M'           !! 2.90 E 17!!-1.00 !! 0.00
NN    O2 + M' = O + O + M'           !! 6.55 E 18!!-1.00 !!495.58
CC R8
YY    H + O2  + M'= HO2 + M'         !! 2.30 E 18!!-0.80 !! 0.00
NN    HO2 + M'= H + O2 + M'          !! 3.19 E 18!!-0.80 !!195.39
CC R9
YY    HO2 + H = OH + OH              !! 1.50 E 14!! 0.00 !! 4.2
NN    OH  +OH = HO2 + H              !! 1.50 E 13!! 0.00 !!170.84
CC  R10
YY   HO2 + H =  H2  +  O2            !!  2.50E 13!! 0.00 !!2.90
NN   H2  + O2=  HO2 +  H             !!  7.27E 13!! 0.00 !!244.33
CC  R11
YY   HO2 + H = H2O + O               !!  3.00E 13!! 0.00 !!7.2
NN   H2O + O = HO2 + H               !!  2.95E 13!! 0.00 !!244.51
CC  R12
YY   HO2 +O  =  OH + O2              !!  1.80E 13!! 0.00 !!-1.7
NN   OH  +O2 =  HO2+ O               !!  2.30E 13!! 0.00 !!231.71
CC  R13
YY   HO2+ OH =H2O+ O2                !!  6.00E 13!! 0.00 !!0.000
```

```
NN   H2O+ O2 =HO2+ OH                !!  7.52E 14!! 0.00 !!304.09
CC  R14
Y*   HO2 + HO2 = H2O2 + O2           !!  2.50E 11!! 0.00 !!-5.2
NN   H2O2+  O2 =  HO2 +HO2           !!  1.02E 12!! 0.00 !!169.82
CC  R15
YY   OH + OH + M'= H2O2 + M'         !!  3.25E 22!!-2.00 !! 0.0
NN   H2O2    + M'= OH+OH+ M'         !!  1.69E 24!!-2.00 !!202.29
CC  R16
YY   H2O2 + H= H2+ HO2               !!  1.70E 12!! 0.00 !!15.7
NN             H2+ HO2=H2O2 + H      !!  1.32E 12!! 0.00 !!83.59
CC  R17
YY   H2O2 + H = H2O + OH             !!  1.00E 13!! 0.00 !!15.0
NN   H2O  +OH = H2O2+  H             !!  3.34E 12!! 0.00 !!312.19
CC  R18
YY   H2O2 + O= OH + HO2              !!  2.80E 13!! 0.00 !!26.8
NN  OH    + HO2 = H2O2 + O           !!  9.51E 12!! 0.00 !!86.67
CC  R19
YY   H2O2 + OH = H2O + HO2           !!  5.40E 12!! 0.00 !! 4.20
NN   H2O  + HO2= H2O2+  OH           !!  1.80E 13!! 0.00 !!134.75
CC= H2/O2/NO - MECHANISM (GOOD FOR PREMIXED AND DIFFUSION FLAMES)
CC====     (ZEL'DOVICH NO)
CC====     (ADD ALL REACTIONS OF THE H2/O2 MECHANISMS)
CC  R20
NN     N2 + O  = NO + N              !!  1.80E 14!! 0.00 !!319.0
NN     NO + N  = N2 + O              !!  3.98E 13!! 0.00 !!4.19
CC  R21
NN     O2 + N = NO + O               !!  6.40E 09!! 1.00 !!26.10
NN     NO + O = O2 + N               !!  1.36E 09!! 1.00 !!159.23
CC  R22
NN     N  + OH = NO + H              !!  3.00E 13!! 0.00 !!0.0
NN     NO +  H = N  +OH              !!  8.12E 13!! 0.00 !!200.58
CC==== CO/O2 - MECHANISM (GOOD FOR PREMIXED AND DIFFUSION FLAMES)
CC====  (ADD ALL REACTIONS OF THE H2/O2 AND H2/O2/N2 MECHANISMS)
CC  R23
YY    CO + OH = CO2 + H              !!  4.40E  6!! 1.50 !!-3.1
NN    CO2+  H = CO  +OH              !!  4.97E  8!! 1.50 !!89.74
CC  R24
YY   CO  + HO2= CO2 + OH             !!  1.50E 14!! 0.00 !!98.70
NN   CO2 +  OH= CO  +  HO2           !!  1.70E 15!! 0.00 !!358.18
CC  R25
YY    CO + O + M'= CO2 + M'          !!  7.10E 13!! 0.00 !!-19.0
NN    CO2    + M'= CO  + O + M'      !!  1.42E 16!! 0.00 !!502.65
CC  R26
YY    CO+ O2      = CO2 + O          !!  2.50E 12!! 0.00 !!200.00
NN    CO2 + O     = CO  + O2         !!  2.21E 13!! 0.00 !!226.07
CC  R27
YY      CHO + H   =  CO + H2         !!  2.00E 14!! 0.00 !!0.00
NN      CO  + H2  =  CHO+ H          !!  1.30E 15!! 0.00 !!376.49
CC  R28
YY    CHO + O     =  CO + OH         !!  3.00E 13!! 0.00 !!0.00
NN    CO  + OH    =  CHO+ O          !!  8.55E 13!! 0.00 !!368.48
CC  R29
YY   CHO + O = CO2 + H               !!  3.00E 13!! 0.00 !!0.0
NN   CO2 + H = CHO + O               !!  9.66E 15!! 0.00 !!461.32
CC  R30
YY   CHO + OH     = CO + H2O         !!  1.00E 14!! 0.00 !! 0.00
NN    CO + H2O    = CHO+ OH          !!  2.80E 15!! 0.00 !!439.16
```

```
CC  R31
YY    CHO + O2     = CO + HO2          !!  3.00E 12!! 0.00 !!0.00
NN    CO  +HO2     = CHO+  O2          !!  6.70E 12!! 0.00 !!135.07
CC  R32
YY    CHO + M'     = CO + H + M'       !!  7.10E 14!! 0.00 !!70.3
NN     CO + H + M'= CHO    + M'        !!  1.14E 15!! 0.00 !! 9.98
CC  R33
YY   CH2O+  H      = CHO+ H2           !!  2.50E 13!! 0.00 !!16.7
NN   CHO + H2      = CH2O+ H           !!  1.99E 12!! 0.00 !!78.01
CC  R34
YY    CH2O+ O      = CHO+  OH          !!  3.50E 13!! 0.00 !! 14.60
NN    CHO + OH     = CH2O +O           !!  1.22E 12!! 0.00 !! 67.90
CC  R35
YY   CH2O + OH     = CHO+ H2O          !!  3.00E 13!! 0.00 !! 5.0
NN    CHO + H2O    = CH2O + OH         !!  1.03E 13!! 0.00 !!128.97
CC  R36
YY   CH2O+ HO2     = CHO+ H2O2         !!  1.00E 12!! 0.00 !!33.50
NN    CHO+ H2O2    = CH2O + HO2        !!  1.03E 11!! 0.00 !!26.92
CC  R41
YY    CH2O + CH3   = CHO + CH4         !!  1.00E 11!! 0.00 !!25.5
NN    CHO + CH4    = CH2O+ CH3         !!  2.10E 11!! 0.00 !!90.13
CC  R37
YY    CH2O+ M'     = CHO + H + M'      !!  1.40E 17!! 0.00 !!320.00
NN    CHO +H  + M'= CH2O + M'          !!  2.76E 15!! 0.00 !!-55.51
CC====  CH4/O2 - MECHANISM (GOOD FOR PREMIXED FLAMES ONLY)
CC====  (ADD ALL REACTIONS OF THE H2/O2 AND CO/O2/ MECHANISMS)
CC  R38
YY    CH + O  = CO  + H                !!  4.00E 13!! 0.00 !! 0.0
NN    CO +  H = CH  +O                 !!  1.94E 15!! 0.00 !!736.25
CC  R39
YY   CH  +  O2= CHO + O                !!  3.00E 13!! 0.00 !!0.00
NN   CHO +  O = CH  +   O2             !!  4.00E 13!! 0.00 !!300.99
CC  R39A NEW
Y*   CH  + CO2= CHO +CO                !!  3.40E 12!! 0.00 !!2.90
CC  R40
YY    CH2+ H     = CH  + H2            !!  8.40E  9!! 1.50 !!1.40
NN    CH     + H2= CH2 + H             !!  5.83E  9!! 1.50 !!13.96
CC  R40 A NEW
Y*    CH2+ O     = CO  +  H  + H       !!  8.00E 13!! 0.00 !!0.00
CC  R40 B NEW
Y*    CH2+ O2    = CO  + OH  + H       !!  6.50E 12!! 0.00 !!6.30
CC  R40 C NEW
Y*    CH2+ O2    = CO2 +  H  + H       !!  6.50E 12!! 0.00 !!6.30
CC  R42
YY      CH3 + H   =  CH2+ H2           !!  1.80E 14!! 0.00 !!63.0
NN      CH2 + H2  =  CH3+ H            !!  3.63E 13!! 0.00 !!44.53
CC  R50
YY    CH3 + H      = CH4               !!  1.96E 36!!-7.00 !! 38.00
NN   CH4           = CH3+ H            !!  3.20E 34!!-6.00 !! 457.5
CC  R43
YY    CH3 + O      =  CH2O+ H          !!  7.00E 13!! 0.00 !!0.00
NN    CH2O+  H     =  CH3+ O           !!  9.23E 14!! 0.00 !!292.53
CC  R43 A NEW
NN    CH3 + OH     =  CH2O+ H   + H    !!  9.00E 14!! 0.00 !!64.8
CC  R43 B NEW
NN    CH3 + OH     =  CH2O+ H2         !!  8.00E 12!! 0.00 !!00.0
CC  R43 C NEW
```

```
NN    CH3 + O2    =  CH2O+ H  + O    !!  1.50E 13!! 0.00 !!120.0
CC  R45
YY   CH3 + M      = CH2+ H + M       !!  1.00E 16!! 0.00 !!380.00
NN    CH2+ H + M  = CH3+ M           !!  5.01E 14!! 0.00 !!-75.29
CC  R45 A NEW
CC  R45 B NEW
CC  R46
YY    CH4 + H     = H2 + CH3         !!  2.20E  4!! 3.00 !!36.60
NN    H2  +CH3    = CH4+  H          !!  8.33E  2!! 3.00 !!33.28
CC  R47
YY    CH4 + O     = CH3+OH           !!  1.20E  7!! 2.10 !!31.90
NN    CH3 +OH     = CH4    + O       !!  1.99E  5!! 2.10 !!20.57
CC  R48
YY   CH4 + OH     = CH3+ H2O         !!  1.60E  6!! 2.10 !!10.30
NN   CH3 + H2O    = CH4 +OH          !!  2.61E  5!! 2.10 !!69.64
CC  R49
YY    CH4 + HO2   = CH3+   H2O2      !!  4.00E 12!! 0.00 !! 81.20
NN    CH3 + H2O2  = CH4  +HO2        !!  1.96E 11!! 0.00 !! 9.99
CC  R51
YY   CH4 + CH2    = CH3+ CH3         !!  1.30E 13!! 0.00 !!39.90
NN    CH3+ CH3    = CH4  + CH2       !!  2.44E 12!! 0.00 !!55.06
CC  R61
NN   CH2CO +H     = CH3+  CO         !!  7.00E 12!! 0.00 !!12.6
NN   CH3 +  CO    = CH2CO + H        !!  1.08E 12!! 0.00 !!157.01
CC  R62
NN    CH2CO + O   = CHO+   CHO       !!  1.80E 12!! 0.00 !! 5.60
NN    CHO + CHO   = CH2CO+ O         !!  4.48E 10!! 0.00 !!127.36
CC  R63
NN   CH2CO + OH   = CH2O + CHO       !!  1.00E 13!! 0.00 !! 0.0
NN    CH2O+ CHO   = CH2CO  + OH      !!  7.14E 12!! 0.00 !! 68.46
CC  R64
NN   CH2CO + M'   = CH2+ CO + M'     !!  1.00E 16!! 0.00 !! 248.0
NN    CH2+ CO + M'= CH2CO + M'       !!  7.72E 13!! 0.00 !!-62.88
CC R68
NN    CH3CO + H  = CH2CO + H2        !!  2.00E 13!! 0.00 !!  0.0
NN    CH2CO  + H2= CH3CO + H         !!  4.13E 13!! 0.00 !!247.20
CC  R69
NN    CH3CO+ O    = CH3 + CO2        !!  2.00E 13!! 0.00 !!0.0
NN    CH3 + CO2   = CH3CO + O        !!  3.16E 14!! 0.00 !!476.45
CC  R71
NN    CH3CO       =  CH3 + CO        !!  2.30E 26!!-5.00 !!75.20
NN    CH3 + CO    =  CH3CO           !!  1.82E 25!!-5.00 !!30.0
CC  R76
NN   CH3CHO +  H = CH3CO + H2        !!  4.00E 13!! 0.00 !! 17.6
NN   CH3CO + H2 = CH3CHO + H         !!  7.57E 12!! 0.00 !!98.28
CC  R77
NN   CH3CHO +  O = CH3CO + OH        !!  5.00E 12!! 0.00 !!7.50
NN   CH3CO + OH = CH3CHO + O         !!  4.15E 11!! 0.00 !!80.17
CC  R78
NN   CH3CHO + OH = CH3CO + H2O       !!  8.00E 12!! 0.00 !!0.0
NN   CH3CO + H2O= CH3CHO +OH         !!  6.53E 12!! 0.00 !!143.34
CC  R79
NN   CH3CHO +HO2 = CH3CO + H2O2      !!  1.70E 12!! 0.00 !!44.8
NN   CH3CO + H2O2=CH3CHO +HO2        !!  4.16E 11!! 0.00 !!57.59
CC  R80
NN   CH3CHO +CH2 = CH3CO +  CH3      !!  2.50E 12!! 0.00 !!15.9
NN   CH3CO + CH3 =CH3CHO +CH2        !!  2.34E 12!! 0.00 !!115.06
```

```
CC  R81
NN   CH3CHO +CH3 = CH3CO +  CH4      !!  8.50E 10!! 0.00 !!25.10
NN   CH3CO + CH4 =CH3CHO +CH3        !!  4.25E 11!! 0.00 !!109.10
CC  R82
NN   CH3CHO      = CH3   +  CHO      !!  2.00E 15!! 0.00 !!331.00
NN   CH3   + CHO =CH3CHO             !!  4.60E 12!! 0.00 !!-10.01
CC  R99
CC   C3H6 + O     = CH3CO+ CH3       !!  5.00E 12!! 0.00 !!1.90
CC  CH3CO + CH3        =   C3H6 + O  !!  1.03E 15!! 0.00 !!156.63
CC  R100
CC  NC3H7 + H     = C3H8             !!  2.00E 13!! 0.00 !! 0.0
CC    C3H8             =  NC3H7 + H  !!  4.01E 15!! 0.00 !!419.13
CC  R101
CC  IC3H7 + H     = C3H8             !!  2.00E 13!! 0.00 !! 0.0
CC    C3H8             =  IC3H7 + H  !!  1.57E 15!! 0.00 !!407.20
CC  R102
CC  NC3H7 + O2    = C3H6   + HO2     !!  1.00E 12!! 0.00 !!20.90
CC    C3H6 + HO2      =  NC3H7 + O2  !!  5.11E 12!! 0.00 !! 82.88
CC  R103
CC  IC3H7 + O2    = C3H6   + HO2     !!  1.00E 12!! 0.00 !! 12.50
CC    C3H6 + HO2      =  IC3H7 + O2  !!  2.00E 12!! 0.00 !! 62.55
CC  R104
CC  IC3H7         = C3H6   + H       !!  2.00E 14!! 0.00 !!161.90
CC    C3H6 + H         =  IC3H7      !!  2.89E 14!! 0.00 !! 16.56
CC  R105
CC  NC3H7         = C2H4   +CH3      !!  3.00E 14!! 0.00 !!139.00
CC    C2H4 + CH3       =  NC3H7      !!  5.88E 13!! 0.00 !! 57.89
CC  R106
CC  NC3H7         = C3H6   + H       !!  1.00E 14!! 0.00 !!156.10
CC    C3H6 + H         =  NC3H7      !!  3.69E 14!! 0.00 !! 22.69
CC  R107
CC   C3H8 + H     =NC2H7 + H2        !!  1.30E 14!! 0.00 !! 40.60
CC   NC2H7    +    H2  =   CH3H8+ H  !!  2.61E 12!! 0.00 !! 58.28
CC  R108
CC   C3H8 + H     =IC2H7 + H2        !!  1.00E 14!! 0.00 !! 34.90
CC   IC2H7    +    H2  =   CH3H8+ H  !!  5.13E 12!! 0.00 !! 64.51
CC  R109
CC   C3H8 + O     =NC2H7 + H2        !!  3.10E 13!! 0.00 !! 24.10
CC   NC2H7    +    H2  =   CH3H8+ O  !!  2.65E 11!! 0.00 !! 33.77
CC  R110
CC   C3H8 + O     =IC2H7 + OH        !!  2.60E 13!! 0.00 !! 18.70
CC   IC2H7    +    OH  =   CH3H8+ O  !!  5.86E 11!! 0.00 !! 40.30
CC  R111
CC   C3H8 + OH    =NC3H7 + H2O       !!  6.30E  6!! 2.00 !! 2.70
CC   NC3H7   +   H2O  =   C3H8 + OH  !!  5.46E  5!! 2.00 !! 83.04
CC  R112
CC   C3H8 + OH    =IC3H7 + H2O       !!  1.20E  8!! 1.46 !! -0.8
CC   IC3H7  + H2O  =   C3H8 + OH     !!  2.66E  7!! 1.46 !!91.48
CC  R113
CC   C3H8 +  HO2  =NC3H7 + H2O2      !!  6.00E 12!! 0.00 !!81.20
CC   NC3H7  +   H2O2 =   C3H8 + HO2  !!  2.56E 11!! 0.00 !! 30.99
CC  R114
CC   C3H8 + HO2   =IC3H7 + H2O2      !!  2.00E 12!! 0.00 !! 71.10
CC   IC3H7  +  H2O2 = C3H8 + H2O2    !!  1.33E 11!! 0.00 !! 32.83
CC  R115
CC   C3H8 + CH3   =NC3H7 + CH4       !!  7.50E 12!! 0.00 !! 62.50
CC   NC3H7  +  CH4  =   C3H8 + CH3   !!  1.33E 11!! 0.00 !! 83.50
```

```
CC  R116
CC   C3H8 + CH3   =IC3H7 + CH4       !!  4.30E 12!! 0.00 !! 55.50
CC   IC3H7  +  CH4  =   C3H8 + CH3   !!  5.83E 12!! 0.00 !! 88.43
-END
2
M'      !!CH4     !!  3.00E 00!!
M'      !!CO2     !!  1.5 E 00!!
M'      !!H2      !!  1.  E 00!!
M'      !!CO      !!  0.75E 00!!
M'      !!O2      !!  0.40E 00!!
M'      !!N2      !!  0.40E 00!!
M'      !!H2O     !!  6.5 E 00!!
M       !!CH4     !!  1.00E 00!!
M         EQUAL
-END
```